Dynamics of aqueous salt solutions investigated with two-dimensional terahertz-infrared-visible spectroscopy

Dissertation
zur Erlangung des Grades
„Doktor der Naturwissenschaften“
im Promotionsfach Chemie

am Fachbereich 09
Chemie, Pharmazie, Geographie und Geowissenschaften
der Johannes Gutenberg-Universität Mainz

Laura Antonia Vietze
geb. in Frankfurt am Main

Mainz, 2020

Statutory Declaration

I hereby declare that I wrote this dissertation submitted without any unauthorized external assistance and used only sources acknowledged in the work. All textual passages, which are appropriated verbatim or paraphrased from published and unpublished texts, as well as all information obtained from oral sources are duly indicated and listed in accordance with bibliographical rules. In carrying out this research, I complied with the rules of standard scientific practice as formulated in the statutes of the Johannes Gutenberg-University Mainz to insure standard scientific practice.

I will write in the first person plural instead of singular (we instead of I) to make the text more readable.

Laura Antonia Vietze

"It is important to realize that in physics today,
we have no knowledge what energy is.
We do not have a picture
that energy comes in little blobs of a definite amount.
It is not that way."

Richard Feynman

Abstract

Low-frequency modes (LFMs) of molecular vibrations excited at room temperature play an important role in various (bio-)chemical reactions and physical processes as they contribute to the thermodynamic functions and potentials. In water, which is ubiquitous in our everyday life, these LFMs are related to the collective dynamics of the water hydrogen-bond network. However, neat water is rare in nature, and most often, it acts as a solvent for various solutes. These solutes can perturb the water network and thus change its structure and dynamics, which are affected by the intermolecular potential energy surface that also determines reaction pathways. Therefore, a detailed understanding of the water network's dynamics is not only of fundamental interest but can help to learn more about (bio-)chemical reaction pathways in an aqueous environment.

Linear absorption spectroscopy can only give limited insights into LFMs, as those spectra are often congested and thus the analysis and interpretation are challenging. Two-dimensional terahertz-infrared-visible (2D TIRV) spectroscopy adds a second dimension. It thus allows disentangling the congested LFM spectra by measuring the coupling and correlations with high-frequency modes (HFMs). 2D TIRV spectroscopy provides new insights into the nature and
(in-)homogeneity of the LFMs, but also reveals the couplings between the LFMs and HFMs, playing an important role in energy dissipation. In this thesis, we investigate the coupling between the low-frequency modes and the OH-stretch mode as well as the inhomogeneity of the hydrogen-bond modes in aqueous salt solutions. To this end, we develop a procedure simplifying the analysis of 2D TIRV spectra significantly.

The theoretical formalism as well as the experimental implementation of this procedure that enables distinguishing different excitation pathways in 2D TIRV spectroscopy and thus simplifies the analysis of the spectra is presented in chapter 4. We verify this approach using the model samples CaF_2 and nitrogen gas. Finally, we simplify the more complex spectrum of neat liquid water by disentangling interfering excitation pathways and thus enabling further investigations on aqueous solutions.

We find in chapter 5, that the coupling between the intramolecular OH-stretch mode and the water libration in the frequency range from $300\ \mathrm{cm}^{-1}$ to $500\ \mathrm{cm}^{-1}$ is enhanced significantly in the hydration shell of Br^- and I^-. This is due to a change of the low-frequency vibrations of the protons that are most close to the anions in this frequency range.

The analysis of the coupling between the OH-stretch and the hydrogen-bond modes in chapter 6 reveals the increasing inhomogeneity of the hydrogen-bond modes with the addition of salts. More precisely, we find that the correlation between the frequencies of the hydrogen-bond modes and the OH-stretch mode increases with the addition of halide anions, in particular due to a shift of the frequencies of the LFMs. We attribute this change to the water molecules in the first hydration shell of anions. The dynamics of the water network becomes more inhomogeneous in the presence of halide anions.

Zusammenfassung

Niederfrequente Moden (engl. low-frequency modes, kurz LFMs) molekularer Schwingungen, die bei Raumtemperatur angeregt sind, spielen eine wichtge Rolle bei verschiedensten (bio-)chemischen Reaktionen und physkalischen Prozessen, da sie zu den thermodynamischen Funktionen und Potentialen beitragen. In Wasser, das allgegenwärtig im alltäglichen Leben ist, hängen diese LFMs mit der kollektiven Dynamik des Wasserstoffbrückennetzwerks zusammen. In der Natur ist reines Wasser jedoch selten und fungiert stattdessen meistens als Lösungsmittel für verschiedenste andere Substanzen. Diese können das Wassernetzwerk stören und so Struktur und Dynamik ändern, welche durch die intermolekulare Potentialfläche beeinflusst werden. Die Potentialfläche wiederum bestimmt chemische Reaktionswege. Aus diesem Grund ist ein detailliertes Verständnis der Dynamik des Wassernetzwerks nicht nur von fundamentalem Interesse, sondern kann auch helfen Reaktionswege in wässriger Umgebung besser zu verstehen.

Einblicke in die niederfrequenten Moden mit linearer Absorptionsspektroskopie sind nur bedingt möglich, da die Spektren oft verdichtet sind und so die Analyse und Interpretation zur Herausforderung wird. Zweidimensionale Terahertz-Infrarot-Sichtbare Spektroskopie (engl. two-dimensional terahertz-infrared-visible spectroscopy, kurz 2D TIRV) fügt eine weitere Dimension hinzu, sodass die verdichteten Spektren der LFMs entzerrt werden indem die Kopplung und Korrelationen mit einer hochfrequenten Mode (engl. high-frequency mode, kurz HFM) gemessen wird. 2D TIRV Spektroskopie gibt so neue Einblicke in die Art und Weise und (In-)Homogenität der LFMs, enthüllt aber auch die Kopplung zwischen den nieder- und hochfrequenten Moden, die eine wichtige Rolle in der Energiedissipation spielt. In dieser Arbeit wird die Kopplung zwischen den niederfrequenten Moden und der OH-Streckschwingung sowie die Inhomogenität der Wasserstoffbrückenschwingungen in wässrigen Salzlösungen untersucht. Dafür entwickeln wir ein Verfahren, dass die Analyse der 2D TIRV Spektren signifikant vereinfacht.

Der theoretsichen Formalismus sowie die experimentelle Ausführung dieses Verfahrens, das die Unterscheidung verschiedener Anregungswege in 2D TIRV Spektroskopie erlaubt und somit die Analyse der Spektren vereinfacht, ist in Kapitel 4 beschrieben. Wir überprüfen den Ansatz mit den Beispielproben CaF_2 und gasförmigem Stickstoff und vereinfachen das komplexe Spektrum von Wasser indem wir interferierende Anregungswege separieren. Dies ermöglicht weitere Untersuchungen an wässrigen Lösungen.

In Kapitel 5 zeigen wir, dass die Kopplung zwischen der intramolekularen OH-Streckschwingung und den Librationsbewegungen der Wassermoleküle in der Hydrathülle von Br^- und I^- im Frequenzbereich von $300\ \mathrm{cm}^{-1}$ bis $500\ \mathrm{cm}^{-1}$ deutlich verstärkt ist. Dies resultiert aus einer Änderung der niederfrequenten Schwingungen der Protonen, die den Anionen am nächsten sind.

Die Analyse der Kopplung zwischen der OH-Streck- und den Wasserstoffbrücken-schwingungen in Kapitel 6 zeigt die zunehmende Inhomogenität der Wasserstoffbrücken-schwingungen mit der Zugabe von Salz. Insbesondere beobachten wir, dass die Korrelation zwischen den Frequenzen der niederfrequenten Wasserstoffbrückenschwingungen und der

OH-Streckschwingung mit der Zugabe von Halogenanionen ansteigt, vorwiegend durch eine Verschiebung der Frequenzen der niederfrequenten Moden. Wir schreiben diese Änderungen den Wassermolekülen in der ersten Hydrathülle der Anionen zu, die somit zu einer erhöhten Inhomogenität der Dynamik des Wassernetzwerks in Anwesenheit von Halogenanionen führt.

This thesis is based on the following publications:

Chapter 4:

L. Vietze, E. H. G. Backus, M. Bonn and M. Grechko. *Distinguishing different excitation pathways in two-dimensional terahertz-infrared-visible spectroscopy.* (in preparation)

Chapter 5:

L. Vietze, J. Hunger, P. Seliya, M. Bonn and M. Grechko. *Coupling between the water OH-stretch and the libration modes in neat water and in the hydration shell of halide anions*. (in preparation)

Chapter 6:

L. Vietze, J. Hunger, M. Bonn and M. Grechko. *Inhomogeneity of the hydrogen-bond modes in liquid water and halide salts solutions*. (in preparation)

Other publications:

M. Grechko, S. A. Bretschneider, **L. Vietze**, H. Kim, and M. Bonn. *Vibrational coupling between organic and inorganic sublattices of hybrid perovskites*. Angew. Chem. Int. Ed. 2018, 57, 13657.

L. Vietze, M. Bonn and M. Grechko (2019). *Two-Dimensional Terahertz-Infrared-Visible Spectroscopy Elucidates Coupling Between Low-and High-Frequency Modes.* In: Cho M. (eds) *Coherent Multidimensional Spectroscopy*. Springer Series in Optical Sciences, vol 226. Springer, Singapore.

CONTENTS

1 INTRODUCTION

1.1 WATER AND AQUEOUS SOLUTIONS

1.1.1 Water

Water is the most important liquid on earth. It plays a crucial role in cell biology and therefore is essential for life on earth [1,2]. Even though water is ubiquitous in our daily life, many of its properties remain mysterious as they vary from the usual behavior of liquids. Prominent anomalies as the density maximum at $4\ °C$ (usually the density of liquids decreases when cooled), the extraordinary high surface tension, and the fact that the density of the solid (ice) is smaller than the liquid are decade-old scientific puzzles but only partly understood. These and even more anomalies can be related to the presence of hydrogen bonds and their cooperative effects in the liquid [3–7]. Hydrogen bonds connect two water molecules next to each other. These connections are based on the electrostatic force and are formed due to the charge displacement in the water molecule. On average, one molecule is connected to 3.6 other molecules. This leads to a tetrahedral structure and the so-called hydrogen bond network (Fig. 1.1) [1,5]. This hydrogen-bond network is highly dynamic and involves the breaking and formation of hydrogen bonds on a (sub-)picosecond timescale [8]. These inter-, but also the intramolecular motions in the water network, are highly sensitive to their environment. For example, the intramolecular OH-stretch mode depends on the hydrogen bonds, which are formed with the surrounding molecules [9]. In turn, the strength of these hydrogen bonds is influenced by the number and geometry of the neighboring molecules [10,11]. These cooperative properties of the hydrogen-bond network are closely related to the complex thermodynamic potential. This thermodynamic potential is determined by the potential energy surface, which has a significant impact on the dynamics of the water molecules [12]. For these reasons, a better understanding of the intermolecular dynamics can help to expand the knowledge about the potential energy surface and is of high interest in current water research. However, despite the enormous progress in the understanding of the molecular structure and dynamics of water in the last century, the discussion is vividly continued [4–6,13].

1.1.2 Aqueous salt solutions

Neat liquid water is rare in nature. Two-thirds of the earth's surface is covered with salt water, in living organisms, salt solutions constitute the matrix for various other components. In addition, water is important for a variety of other fields, ranging from geology to chemistry and for industrial processes, where it works as a solvent for various other molecules [1,8].One of the simplest but simultaneously most interesting solutes are monatomic ions. They regulate biological processes in cells but also influence the rates of chemical reactions in water [1,3]. Seminal work on the influence of ions on aqueous systems was performed in the 19th century by Franz Hofmeister [14]. He analyzed the influence of different ions on the solubility of proteins in water and ordered the ions according to their effect. The so-called *Hofmeister series* was later found in many more experiments, e.g. by sorting the salts according to the viscosity of their aqueous solutions [8]. Hofmeister made use of the good solubility of ions in

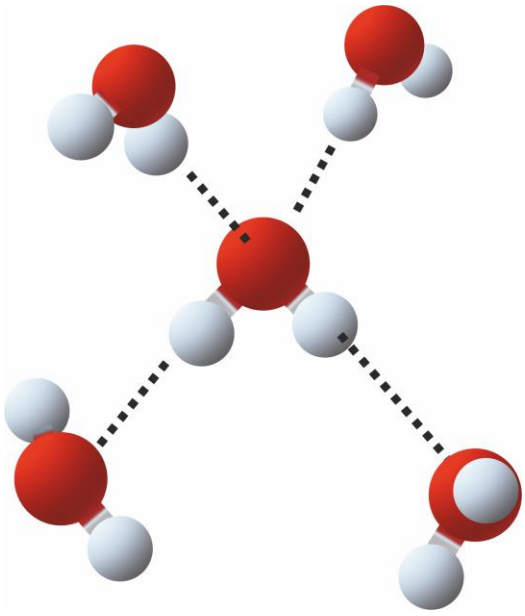

Fig. 1.1 Schematic of the tetrahedral structure of liquid water.

water. Due to the polarity of the water, the water molecules form hydration shells around the charged ions. That leads to the breaking of hydrogen bonds, accompanied by structural changes of the water network [8,13]. X-ray and neutron diffraction as well as X-ray absorption techniques were used to study the structure of the hydration shell and to determine static hydration numbers and radii [13,15]. In addition, the nature and timescales of the dynamics in the hydration shell change. Their alteration was investigated with NMR, dielectric relaxation, and linear absorption spectroscopy, where the so-called dynamic hydration number, as well as residence and reorientation times of the water molecules in the hydration shell, were determined [8,13,16]. A slow-down of the dynamics in the hydration shell of halide anions (Cl^-, Br^- and I^-) was observed with pump-probe spectroscopy [17], while a more fragile hydration shell of the Cl^--ion was found with simulations [18]. However, not only the alteration of the dynamics, but also the range of influence of the ions is highly debated. Some publications describe that not the whole bulk water, but mainly the first hydration shell of the ions is affected. In particular, the dynamics of the water molecules in the first hydration shell were found to be different from bulk water, while the dynamics in the second hydration shell resemble bulk water. This was shown in the analysis of the reorientation times of the water molecules and the frequencies of the vibrational modes [19,20]. On the other hand, effects beyond the first hydration shell were observed as well. A long-range orientational order with the addition of ions [21] and cross-correlations between the solute and the solvent in the second hydration shell were found [22]. A more detailed and clear description of the dynamics in aqueous salt solutions is still elusive.

Nevertheless, it is unambiguous that the different molecular structures and the dynamics in aqueous salt solutions cause different potential energy surfaces of water and aqueous mixtures [23]. It is of major interest to understand these differences, since a different potential energy surface alters reaction pathways in the solvent and e.g. influences the protein folding and aggregation in biology [23–26]. By investigating the molecular dynamics across a

wide frequency, respectively energy range, we can learn about the distribution and nature of the energy levels and therefore receive a more detailed understanding of the potential energy surface. Here, of major importance are the intermolecular dynamics, whose states are populated at room temperature ($\sim 200\ \mathrm{cm}^{-1}$) [27]. In water, the intermolecular motions are particularly the hydrogen-bond modes with translational and rotational degrees of freedom. Hindered translation hydrogen-bond modes are the hydrogen-bond bending ($60\ \mathrm{cm}^{-1}$) and stretching ($180\ \mathrm{cm}^{-1}$). Hindered rotational modes are the so-called librations, which occur at energies above room temperature ($350 - 700\ \mathrm{cm}^{-1}$) [28,29]. These dynamics occur on a sub-picosecond timescale. Vibrational spectroscopy techniques can monitor dynamics on such timescales, respectively, in such frequency ranges [8,30]. Therefore, vibrational spectroscopy is an appropriate tool to study the potential energy surface.

1.2 Spectroscopy

Spectroscopic techniques make use of the interactions of one or several electromagnetic fields with a sample to learn more about its properties. These interactions involve the excitation of the sample and the detection of the emitted electromagnetic field, which is detected as a function of the excitation and the emitted frequency. The detected frequencies provide information on the excited modes in the sample, giving information about the distribution of the energy levels and eigenstates as well as the population evolution [27,31,32].

Figure 1.2 gives an overview of the electromagnetic spectrum with the corresponding wavelengths and frequencies. The smaller the mass of the moving part or particle, the higher the frequency of the respective motion. For instance, the motions of water molecules relative to each other have frequencies below $200\ \mathrm{cm}^{-1}$. That means they are thermally excited at room temperature, which corresponds to energies, respectively frequencies of $\sim 200\ \mathrm{cm}^{-1}$. Electromagnetic radiation with frequencies below $1000\ \mathrm{cm}^{-1}$ (Terahertz region, often also described as far-infrared region) can investigate these hindered translations or rotations of the molecules (see Fig. 1.2). They are classified as low-frequency modes (LFMs) and reflect the intermolecular degrees of freedom of the system.

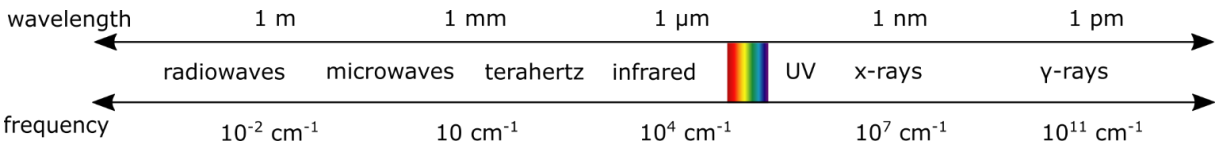

Fig. 1.2 Electromagnetic spectrum with different frequency regions and respective wavelengths [27].

1.2.1 Linear spectroscopy

One of the simplest way to probe vibrations is linear absorption spectroscopy. The incoming light induces a polarization in the sample. This polarization emits light, which is detected afterward. If light is absorbed at a certain frequency, it means that a mode at the same frequency is excited. For liquid water, the intermolecular LFMs can be observed in the THz frequency range from $50 - 1000\ \mathrm{cm}^{-1}$ ($1\ \mathrm{THz} = 33\ \mathrm{cm}^{-1}$). The linear absorption spectrum

is shown in Fig. 1.3. Absorption spectra of aqueous solutions in this range are very congested and due to their broad shape challenging to interpret [33]. Nevertheless, a broad peak with a maximum at $\sim 700\ \mathrm{cm}^{-1}$ is clearly identified. The addition of salt, known to change the water structure, also changes the properties of this peak, evidencing its sensitivity to the water structure [29]. However, this broad peak does not show clear indications for multiple components, which were identified using polarized Raman spectroscopy, revealing two to three individual libration modes, at $\sim 450\ \mathrm{cm}^{-1}$, $\sim 710\ \mathrm{cm}^{-1}$and maybe at $\sim 540\ \mathrm{cm}^{-1}$. The mode at $450\ \mathrm{cm}^{-1}$ does not show up in the linear absorption spectra, but in Raman spectra (not IR, but Raman active) [28].

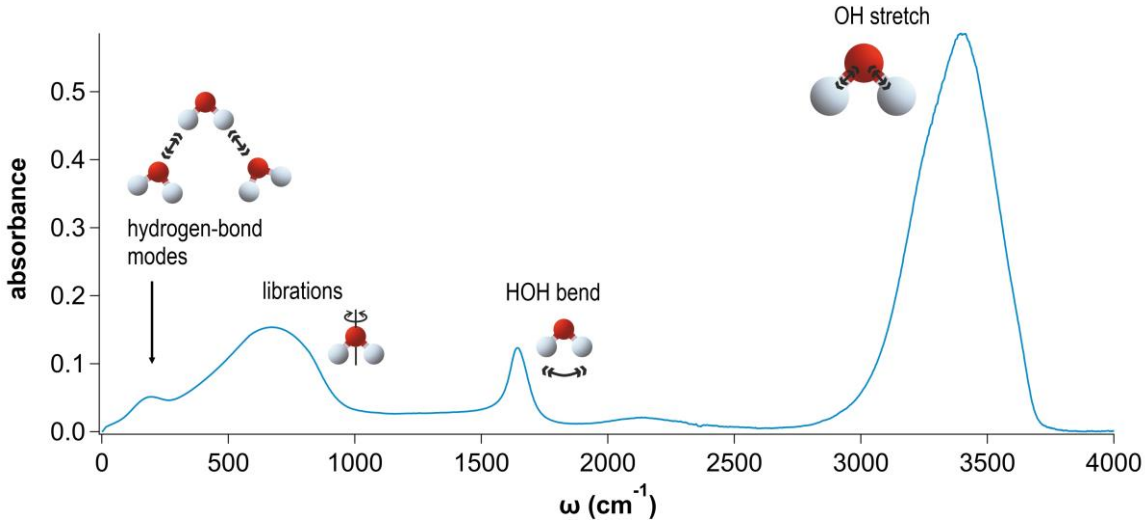

Fig. 1.3 Absorption spectrum of water at 20 °C in the range from 0 to $4000\ \mathrm{cm}^{-1}$. The data is taken from [42].

At the wing of the broad peak, a shoulder is situated at around $\sim 180\ \mathrm{cm}^{-1}$. This shoulder is attributed to hindered translations, the hydrogen-bond stretching mode [29]. Also for this mode, a shift to lower frequencies with the addition of salts is observed. Not so pronounced in the absorption spectrum is the hydrogen-bond bending mode at $\sim 60\ \mathrm{cm}^{-1}$. It can be clearly observed in the Raman spectra [34–37].

Besides the above-described modes of the water molecules, the spectrum in the THz range of aqueous salt solutions also involves modes of the ions. Rattling modes of the hydrated ions are located between 30 and $250\ \mathrm{cm}^{-1}$ [16]. Since their contribution to the absorbance is small compared to the modes of the water molecules, these rattling modes become better visible considering the difference spectra of the aqueous solutions and neat water.

As Fig. 1.3 illustrates, the spectrum of water and those of the aqueous salt solutions are very congested in the THz range. It is challenging to disentangle the different modes and to resolve correlations with the same or other modes as well as drawing further conclusions on the nature of the modes, e.g. the (in-)homogeneity. Multi-dimensional spectroscopy can help here by measuring mode-mode couplings and revealing correlations.

A candidate for the correlation with the LFMs of water is the OH-stretch mode in the mid-infrared region ($1000 - 4000\ \mathrm{cm}^{-1}$), centered at $3450\ \mathrm{cm}^{-1}$. This mode is known to be sensitive to its environment. Its center frequency correlates with the hydrogen-bond strength: weaker bound OH-groups have a higher stretching frequency [38]. Other influences from the environment on the OH-stretch mode are based on the concept of cooperativity. This concept involves the influences of the number and geometry of the neighboring water molecules on the hydrogen bond strength. In consequence, these cooperative effects influence the OH-stretch mode and its center frequency [10,11,39]. Besides this, an influence of the coupling with the other nearly resonant OH-stretch oscillators is observed. The oscillation is delocalized over several water molecules, leading to a collective mode that contributes in the same frequency range [39,40]. In addition, the second overtone of the HOH-bending mode (Fermi resonance) is discussed as another contribution to the OH-stretch peak. Both modes might overlap, and the Fermi resonance shows up as a shoulder on the red wing of the OH-stretch peak [41]. However, with linear spectroscopy, it is challenging to separate these various influences on the modes that result from anharmonicities. Here, multi-dimensional spectroscopy techniques that measure the coupling between different modes yield valuable insights.

1.2.2 Multi-dimensional spectroscopy

In contrast to linear spectroscopy, multi-dimensional spectroscopy enables access to multiple modes at once and reveals couplings and correlations between them. Multi-dimensional techniques analyze the interaction with the sample and multiple electric fields. For accurate experiments that investigate molecular dynamics, femtosecond light pulses with high intensities are useful. The development of adequate light sources in the last decades has led to a further development of multi-dimensional spectroscopy. Today it is a state-of-the-art technique to investigate nano- to femtosecond molecular dynamics in chemical, biological, and physical systems [32,43,44].

Similar to 2D Nuclear Magnetic Resonance (NMR) spectroscopy, which measures the coupling between nuclear spins [45], multi-dimensional spectroscopy can reveal the coupling between different modes that contribute to the signal [44]. This will show up as a peak in a multi-dimensional (usually 2D) spectrum. This coupling can originate from mechanical or electrical anharmonicities. Furthermore, due to the multiple interactions with the appropriate modes, 2D spectroscopy distinguishes different types of broadening, depending on the shape of that peak. Homogenously broadened peaks (roundish) point to a homogeneous environment of the molecules (see Fig. 1.4 a)), whereas different local environments can result in slightly different transition frequencies, leading to inhomogeneous broadening (the peak shows some slope, see Fig. 1.4 b)) [46]. Besides this, ultrafast multi-dimensional spectroscopy can monitor changes of the peak shape over time, by varying the delay time between the pulses (pump-probe spectroscopy) [41]. This can reveal energy relaxation pathways, for instance. In general, the addition of another dimension can help to decompose the spectrum [47].

Multi-dimensional spectra are acquired by multiple pulse experiments, where the sample interacts at least twice with one or several light fields. These interactions generate a nonlinear signal field, which is detected time- and/or frequency-resolved. The experimental implementation of multi-dimensional techniques can be considered as an extension of pump-

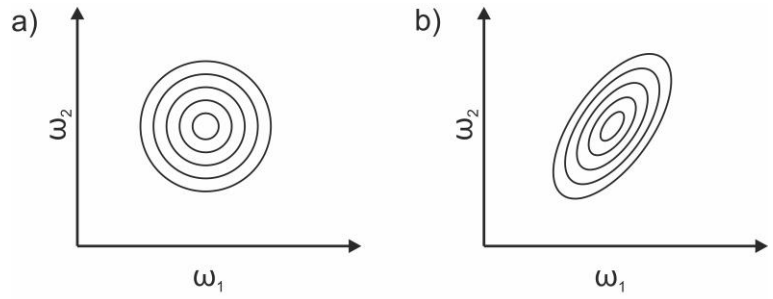

Fig. 1.4 a) Homogeneously broadened peak. b) Inhomogeneously broadened peak.

probe spectroscopy. The additional dimensions can either be obtained by scanning the pump frequencies or by varying the time delay between the different light pulses. In the latter case, where applicable, a Fourier transformation converts the data from time into frequency domain [32,44]. An overview of different 2D techniques and the frequency range they cover is shown in Fig. 1.5 [48].

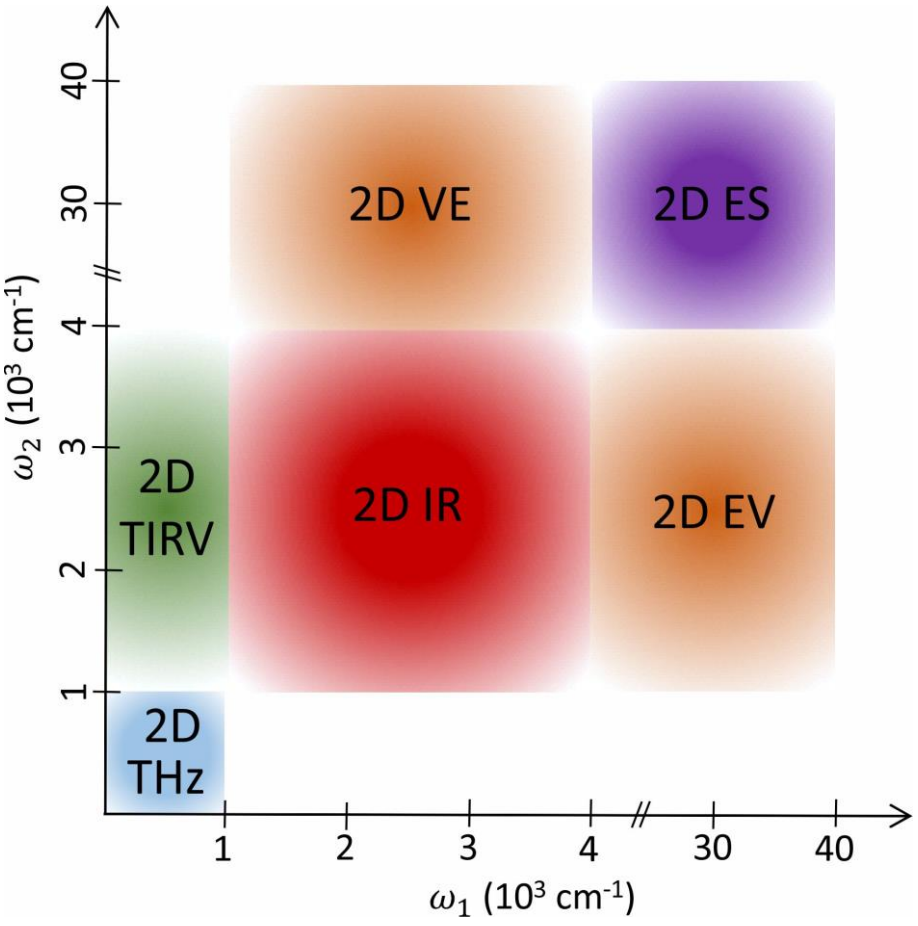

Fig. 1.5 Overview of various 2D spectroscopy techniques and the frequency range they cover. Besides the techniques along the diagonal (2D THz, 2D IR and 2D ES (electronic spectroscopy)), there are hybrid techniques like 2D electronic-vibrational (EV) or vibrational-electronic (VE) spectroscopy and 2D Terahertz-InfraRed-Visible (TIRV) spectroscopy, adopted from [48].

Multi-dimensional spectroscopy in the mid-IR range (2D-IR) has developed quickly in recent years and has provided insights into the coupling mechanisms between the OH-stretch and other vibrational modes of water [49–51]. The extension of this multi-dimensional technique to the THz range could help investigate the couplings and broadening mechanisms of the LFMs and reveal, e.g., energy dissipation pathways. Due to the challenging development of the needed high-power femtosecond light sources, multi-dimensional THz techniques are still in a nascent stage [52]. For this reason, 2D-THz spectroscopy, the extension of 2D-IR spectroscopy to the THz range, was not yet performed on liquids. Prospectively, it is promising to investigate the (in-)homogeneity of the LFMs in water with 2D-THz spectroscopy [50,53]. The first attempt to investigate this (in-)homogeneity of the LFMs of water was performed in 1994, calculating the 2D-Raman spectra of water in the THz range [46,54]. They calculated a homogeneous lifetime of about $150\ \mathrm{fs}$. The experimental implementation of this technique was applied to CS_2, CCl_4 and $CHCl_2$ [55,56], but investigations on water turned out to be challenging. A different approach was carried out in 1999 by Cho: 2D-Raman-THz spectroscopy [57]. It allows probing both, IR and Raman active modes simultaneously. The persistence of the measured echo reveals information on the local environment's heterogeneity and lifetime [58]. For water, the echo of the LFMs was found on a $100\ \mathrm{fs}$ timescale, indicating a heterogeneous distribution of the hydrogen-bond network [59]. Furthermore, 2D Raman-THz spectroscopy on aqueous salt solutions revealed a correlation between the inhomogeneity of the collective intramolecular hydrogen-bond modes and the viscosity [60]. Also promising for further investigations on aqueous salt solutions is 2D THz-Raman spectroscopy, where the pulses have a different time ordering. It has been applied to other liquids, but not yet to aqueous mixtures [61,62].

Despite the interesting insights 2D-THz techniques can give into the coupling and correlations of LFMs, they cannot access the coupling of the LFMs to the intramolecular modes of water molecules. The nature of this coupling could reveal new information on the (in-)homogeneity and (de-)localization of the modes as well as on the energy dissipation pathways, and therefore on the potential energy surface of the system [47,49,63,64]. Here, hybrid THz-IR techniques like two-dimensional Terahertz-InfraRed-Visible (2D TIRV) spectroscopy could help. In this thesis, the coupling between the LFMs and the OH-stretch mode with 2D TIRV spectroscopy [65] will be investigated and the newly gained insights into the dynamics of the water network in aqueous salt solutions will be presented.

2 THEORY

For the theoretical description of light-matter interactions, we use a semiclassical approach, where matter is treated quantum mechanically and light is described in a classical formalism. We start with the classical Maxwell's equations to describe electromagnetic fields. Together with the quantum mechanical description of the system using density matrices, this leads to the response function formalism and the introduction of Feynman diagrams. We apply these concepts to 2D TIRV spectroscopy to learn more about the intrinsic properties of aqueous salt solutions.

2.1 LIGHT-MATTER INTERACTIONS

The propagation of the electromagnetic waves is described by Maxwell's equations in a classical formalism. Maxwell's equations reveal the relation between the electromagnetic fields $\boldsymbol{E}$ and $\boldsymbol{B}$ of the light and the properties of the material (here, the charge density ρ and the current density j) [66]:

$$\boldsymbol{\nabla} \cdot \mathbf{E} = 4\pi\rho, \tag{2.1}$$

$$\boldsymbol{\nabla} \cdot \boldsymbol{B} = 0, \tag{2.2}$$

$$\boldsymbol{\nabla} \times \boldsymbol{E} = -\frac{1}{c}\frac{\partial \boldsymbol{B}}{\partial t}, \tag{2.3}$$

$$\boldsymbol{\nabla} \times \boldsymbol{B} = -\frac{1}{c}\left(4\pi j + \frac{\partial \boldsymbol{E}}{\partial t}\right). \tag{2.4}$$

Equations (2.1) - (2.4) show the differential representation of the microscopic Maxwell's equations, where c is the speed of light. From these equations we can derive the homogeneous wave equation that describes the propagation of the electromagnetic field in free space ($\rho = 0, j = 0$):

$$\nabla^2 E - \frac{1}{c^2}\left(\frac{\partial^2 E}{\partial t^2}\right) = 0. \tag{2.5}$$

One solution to this equation, describing the propagation of the electromagnetic wave in free space, is

$$E(t) = E_0 e^{-i\omega t} + E_0 e^{i\omega t}. \tag{2.6}$$

The amplitude of the electric field is represented by E_0, whereas the exponential term includes the frequency information. This solution for the electric field can be interpreted in the frequency domain as a monochromatic wave with two components, one with a positive (ω) and the other one with a negative oscillation frequency ($-\omega$). A similar representation is also possible in the time domain, where one component is going forward ($+t$) and the other one backward ($-t$) in time [67].

However, in the presence of polarizable matter, we need to substitute the electric field E by the electric displacement field $H = E + 4\pi P$ in Maxwell's equations. This electric displacement field includes the polarization P, which is induced in the medium. We assume a non-conductive medium without free charges and currents ($\rho = 0, j = 0$) and obtain the inhomogeneous wave equation of electromagnetic fields [67] that describes the fundamentals of light-matter interactions:

$$\nabla^2 E - \frac{1}{c^2}\left(\frac{\partial^2 E}{\partial t^2}\right) = \frac{4\pi}{c^2}\frac{\partial^2 P}{\partial t^2}. \tag{2.7}$$

In this equation, the polarization P is a material-dependent quantity and represents the response of the material to the applied electric field. This response results in the emission of another electric field, which is generated by the polarization and also proportional to it [44,47]:

$$E_{\mathrm{sig}}(t) \propto P(t). \tag{2.8}$$

This emitted signal field E_{sig} can be detected and analyzed to learn more about the induced polarization and thus about the properties of the involved material. For this reason, a mathematical connection between the polarization and the intrinsic properties of the material is needed to learn more about the respective material. To find this connection, we consider the polarization P, which is defined by the expectation value of the dipole moment operator μ [43]:

$$P(t) = \langle \mu \rho(t) \rangle. \tag{2.9}$$

As described in section 2.2, this representation of the system using the density matrix formalism is necessary. With the density matrix $\rho(t)$ the system can be described as a function of the time t in the Liouville space and thereby enables the representation of mixed states as well (see section 2.2). The time evolution of the system, described by density matrices, can be obtained from the Liouville-Von-Neumann equation, an equivalent of the Schrödinger equation [43]:

$$\frac{d}{dt}\rho = -\frac{i}{\hbar}[H_{\mathrm{int}}, \rho]. \tag{2.10}$$

In the case of light-matter interactions, the interaction part of the Hamiltonian H_{int} is given by the product of the dipole moment and the electric field ($H_{\mathrm{int}} = \mu \cdot E$) [44,47]. Solving this Liouville-Von-Neumann equation, we find the perturbative expansion of the density matrix [43]

$$\rho(t) = \rho^{(0)}(-\infty) + \sum_n \rho^{(n)}(t) \tag{2.11}$$

with

$$\rho^{(n)}(t) = \int_0^\infty dt_n \int_0^\infty dt_{n-1} \dots \int_0^\infty dt_1 \left(\frac{i}{\hbar}\right)^n \times [\mu(t_{n-1} + \cdots + t_1), \dots, [\mu(0), \rho(-\infty)] \dots] \times E(t - t_n)\, E(t - t_n - t_{n-1}) \dots E(t - t_n - t_{n-1} \dots - t_1). \tag{2.12}$$

The different factors in the equation describe the evolution of the density matrix over time. It starts with the density matrix at $t = -\infty$, which is altered by several interactions that occur after the time intervals $\Delta t = 0, t_1, \dots t_{n-1}$. These interactions are represented by the dipole moment operators $\mu(\Delta t)$. Note that the dipole moment operators in Eq. (2.12) are different in nature from the dipole moment operator in Eq. (2.9).

By using this perturbative expansion of the density matrix, we can calculate the polarization from Eq. (2.9) and get [32,43,44]

$$P(t) = \sum_n P^{(n)}(t) \tag{2.13}$$

with

$$P^{(n)}(t) = \int_0^\infty dt_n \int_0^\infty dt_{n-1} \dots \int_0^\infty dt_1\ S^{(n)}(t_n, t_{n-1}, .. t_1) \times E(t - t_n)\, E(t - t_n - t_{n-1}) \dots E(t - t_n - t_{n-1} \dots - t_1), \tag{2.14}$$

and the so-called response function

$$S^{(n)}(t_n, t_{n-1}, .. t_1) = \left(\frac{i}{\hbar}\right)^n \langle \mu(t_n + \cdots + t_1)\, [\mu(t_{n-1} + \cdots + t_1), \dots, [\mu(0), \rho(-\infty)] \dots] \rangle. \tag{2.15}$$

This response function includes all information about the response of a system to incoming electric fields. It is the heart of the description of light-matter interactions.

From Eqs. (2.13) and (2.14), we can see that the polarization can be expanded in powers of the incoming electric field [67]:

$$P = \varepsilon_0 \chi^{(1)} E + \varepsilon_0 \chi^{(2)} E^2 + \varepsilon_0 \chi^{(3)} E^3 + \cdots = P^{(1)} + P_{\mathrm{NL}}. \tag{2.16}$$

The coefficients are the product of the vacuum permittivity ε_0 and the respective susceptibilities $\chi^{(i)}$. The contain information about the response of the medium, respectively, the response function as can be seen by comparing (2.16) and (2.14). For further considerations, we will distinguish between the linear and nonlinear parts of the polarization. This (non-)linearity is reflected by the (non-)proportionality to the incoming electric fields. The linear polarization is the subject of linear spectroscopy; the nonlinear polarization is considered in nonlinear spectroscopy.

2.2 QUANTUM MECHANICAL DESCRIPTION OF A HARMONIC OSCILLATOR

To better understand how light-matter interactions change a system, we will consider the density matrix in more detail. The density matrix is the equivalent of the wave function, albeit in Liouville space. It describes the current state of the system. Similar to the wave function, the density matrix often uses the eigenstates of the harmonic potential (Fig. 2.1), which is given by the parabola

$$V(x) = \frac{1}{2}kx^2, \tag{2.17}$$

with k being the force constant and x the displacement [27]. A system with such a potential is called a *harmonic oscillator*. As long as the displacement is small enough, many systems can, at least locally, be approximated by such a potential. Its great advantage is that its equation of motion (Eq. (2.10)) can be solved analytically.

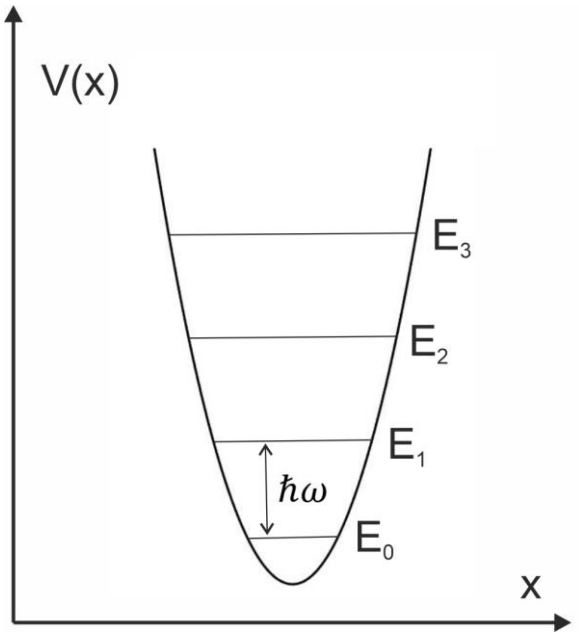

Fig. 2.1 Harmonic oscillator potential with the respective energy levels.

In the quantum mechanical picture, the resulting physical observables like the energy can only have discrete values. For the harmonic oscillator, the energy for a state with the quantum number n is given by [27]

$$E_n = \left(\frac{1}{2} + n\right)\hbar\omega. \tag{2.18}$$

The resonance frequency ω is given by $\omega = \sqrt{k/m}$ with k being the force constant and m the reduced mass. In contrast to the wave function, the density matrix $\rho = |a\rangle\langle b|$ is represented by a ket and a bra. Such a system, described by a density matrix, does not necessarily have to be in a pure state, it can also be in a mixed state.

During light-matter interactions, the occupation of these energy levels can change. As can be seen from Eq. (2.18), the resonance frequency ω is directly related to the spacing between two energy levels $\Delta E = \hbar\omega$ [27]. An incoming electric wave can now bring the system to a higher energy level by adding energy to a system (excitation) or interacting in the opposite way and de-exciting the system. We speak of a resonant interaction if the frequency of the electromagnetic wave equals the resonance frequency of the system.

2.3 Response function formalism for linear spectroscopy

To derive a connection between the polarization P and the system for linear spectroscopy, we make use of the response function introduced above. With considering the first-order terms from Eqs. (2.14) and (2.15), P follows to [43,44]

$$P^{(1)}(t) = \int_0^\infty dt_1 \; S^{(1)}(t_1)\, E(t - t_1), \tag{2.19}$$

with the response function

$$\begin{aligned} S^{(1)}(t_1) &= \frac{i}{\hbar}\langle \mu(t_1)\, [\mu(0), \rho(-\infty)]\rangle \\ &= \frac{i}{\hbar}(\langle \mu(t_1)\, \mu(0)\rho(-\infty)\rangle - \langle \mu(t_1)\rho(-\infty)\mu(0)\rangle). \end{aligned} \tag{2.20}$$

The polarization depends linearly on the incoming electric field, as well as on the linear response function. The linear response function $S^{(1)}(t_1)$ includes the change of the system, which is described by the evolution of the density matrix. The two terms in the response function (Eq. (2.20)), resulting from the commutator, show the two different possibilities of the interaction. In the first term, the interaction happens at the ket of the density matrix as the responsible dipole moment operator $\mu(0)$ acts on the left side of the density matrix. In the second term, the dipole moment operator $\mu(0)$ is on the right side of the density matrix; thus, the electric field changes the bra. In both cases, the first interaction at $t = 0$ is the excitation of the system, transmitted by the dipole moment operator $\mu(0)$. The second step at the time t_1 is represented by the dipole moment operator $\mu(t_1)$. This leads to the de-excitation of the system and the emittance of the signal electric field. Besides this, Eq. (2.20) shows that in linear spectroscopy, the polarization, and therefore the detected signal field E_{sig}, is proportional to the square of the transition dipole μ.

2.4 Response function formalism for nonlinear spectroscopy

For nonlinear spectroscopy, we need to consider higher orders of the polarization. Here, we will consider third-order non-linear spectroscopy to apply the results to 2D TIRV spectroscopy later. Equations (2.14) and (2.15) then read [43,44]

$$\begin{aligned} P^{(3)}(t) = \int_0^\infty dt_3 \int_0^\infty dt_2 \int_0^\infty dt_1 \; & S^{(3)}(t_3, t_2, t_1) \\ & \times E_3(t - t_3)\, E_2(t - t_3 - t_2\,) E_1(t - t_3 - t_2 - t_1), \end{aligned} \tag{2.21}$$

and

$$S^{(3)}(t_3, t_2, t_1) = \left(\frac{i}{\hbar}\right)^3 \langle \mu(t_3 + t_2 + t_1)\, [\mu(t_2 + t_1), [\mu(t_1), [\mu(0), \rho(-\infty)]]]\rangle. \tag{2.22}$$

Here, we introduced indices of the electric fields to better differentiate between the fields at different times, as their spectrum might vary. The commutator term includes all possible combinations of interactions. Each interaction with an incoming field can either change the bra or the ket, leading to a total of $2^3 = 8$ terms. They read [43,44]

$$\begin{aligned}
&\langle \mu(t_3 + t_2 + t_1)\, \Big[\mu(t_2 + t_1), \big[\mu(t_1), [\mu(0), \rho(-\infty)]\big]\Big]\rangle \\
&= \langle \mu(t_3 + t_2 + t_1)\mu(t_2 + t_1)\mu(t_1)\mu(0)\rho(-\infty)\, \rangle \\
&\quad -\langle \mu(t_3 + t_2 + t_1)\mu(t_2 + t_1)\mu(t_1)\rho(-\infty)\mu(0)\, \rangle \\
&\quad -\langle \mu(t_3 + t_2 + t_1)\mu(t_2 + t_1)\mu(0)\rho(-\infty)\mu(t_1)\, \rangle \\
&\quad +\langle \mu(t_3 + t_2 + t_1)\mu(t_2 + t_1)\rho(-\infty)\mu(0)\mu(t_1)\, \rangle \\
&\quad -\langle \mu(t_3 + t_2 + t_1)\mu(t_1)\mu(0)\rho(-\infty)\, \mu(t_2 + t_1)\rangle \\
&\quad +\langle \mu(t_3 + t_2 + t_1)\mu(t_1)\rho(-\infty)\mu(0)\mu(t_2 + t_1)\, \rangle \\
&\quad +\langle \mu(t_3 + t_2 + t_1)\mu(0)\rho(-\infty)\mu(t_1)\mu(t_2 + t_1)\, \rangle \\
&\quad -\langle \mu(t_3 + t_2 + t_1)\rho(-\infty)\mu(0)\mu(t_1)\mu(t_2 + t_1)\, \rangle.
\end{aligned} \tag{2.23}$$

In this mathematical description, a dipole moment operator on the left side of the density matrix corresponds to a change of the ket with the respective interaction, while a dipole moment operator on the right corresponds to a change of the bra.

A better understanding of the interactions described by these terms can be obtained by a graphical representation, e.g. the so-called Feynman diagrams. The respective Feynman-diagrams to Eq. (2.23) are shown in Fig. 2.2. The following rules apply to them [43,47]:

- The density matrix, thus the system, is represented by the bra-ket notation and two vertical lines. It evolves in time from the bottom to the top.
- Interactions with the electric fields are represented as arrows. This interaction can either be on the left (changing the ket of the density matrix) or on the right side (changing the bra of the density matrix). The frequencies of the interacting fields ω_i are labeled according to their time order, as introduced in Eq. (2.21).
- Incoming arrows on the left or outgoing arrows on the right represent an interaction with the "positive" oscillating part of the field in Eq. (2.6), outgoing arrows on the left and incoming ones on the right represent an interaction with the "negative" oscillating part. An incoming arrow is associated with an excitation of the respective state, while an outgoing one is associated with a de-excitation. However, for simplicity, we restrict ourselves to interactions with incoming arrows only.
- The last interaction is different in nature since the light is emitted. The frequency is given by the corresponding combination of $\omega_{\mathrm{sig}} = \pm\omega_1 \pm \omega_2 \pm \omega_3$. Here, we restrict ourselves to outgoing arrows that change the ket.
- After the last interaction, the system needs to be in a population state.

If the interaction order of the electric fields E_1, E_2 and E_3 changes, e.g., because in the experiment pulsed fields are used, we need to consider a possible different time ordering of

the three incoming electric fields. In this case, for each of the Feynman diagrams, respectively terms in Eq. (2.23), there are $3! = 6$ possibilities, leading to in total 48 excitation pathways for third order interactions. However, in general many of these possibilities can be ruled out. For example, the interaction order of the electric fields is fixed or only certain frequency combinations of $\omega_{\mathrm{sig}} = \pm\omega_1 \pm \omega_2 \pm \omega_3$ are detected.

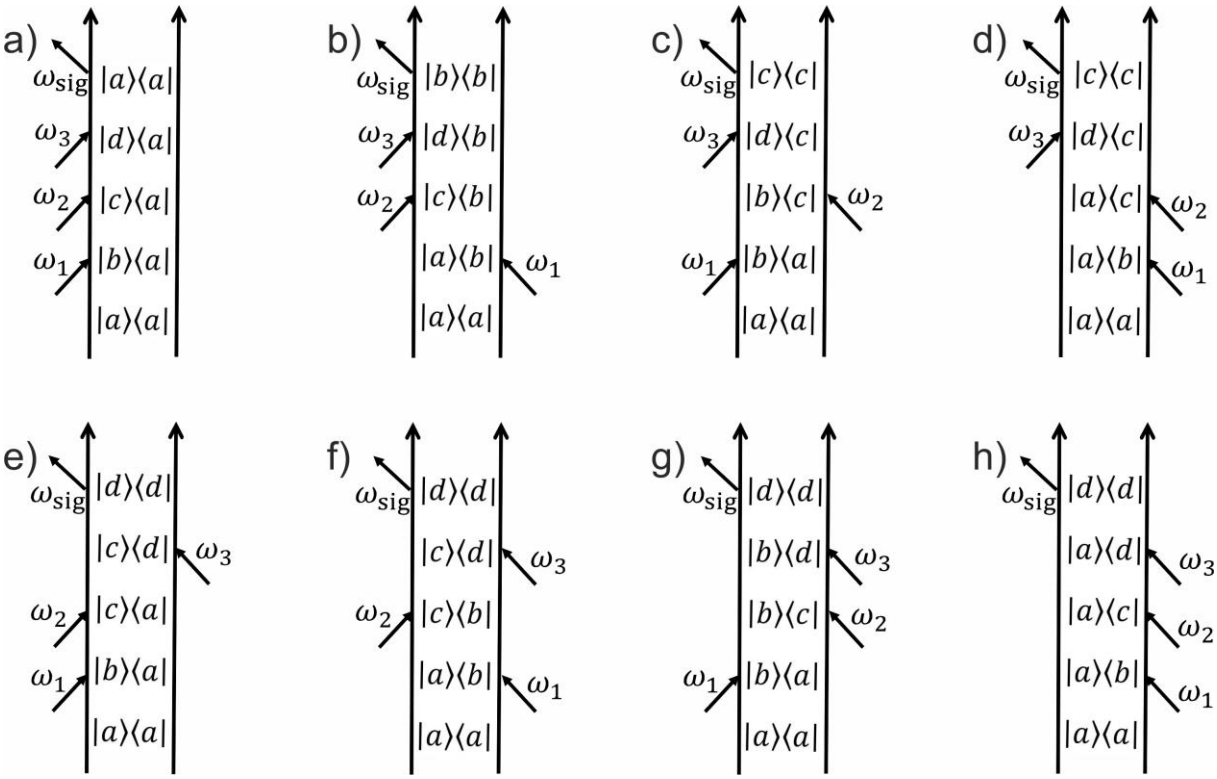

Fig. 2.2 The eight possible Feynman pathways in third-order spectroscopy, adapted from [43].

2.5 Response function formalism and Feynman diagrams for 2D TIRV spectroscopy

In this work, we apply the third-order nonlinear spectroscopy technique 2D TIRV (Terahertz-InfraRed-Visible) to study the coupling between low-frequency modes (LFMs, $\leq 1000\ \mathrm{cm}^{-1}$) and high-frequency modes (HFMs, $\geq 1000\ \mathrm{cm}^{-1}$). We assume a system with one resonance in the LFM and HFM range, respectively. To measure this coupling, we need to excite both modes, the LFM and HFM, with electric fields in the respective frequency range. First, we excite the LFM with the THz beam ($E_1 = E_{\mathrm{THz}}$). Afterward, the HFM mode is excited with an IR beam ($E_2 = E_{\mathrm{IR}}$). Finally, a narrowband 800 nm beam (E_{VIS}, VIS for visible) is used to upconvert the system into a virtual state. The signal is emitted at the frequencies $\omega_{\mathrm{sig}} = \pm\omega_{\mathrm{THz}} \pm \omega_{\mathrm{IR}} \pm \omega_{\mathrm{VIS}}$ .This excitation scheme is shown in Fig. 2.3 a).

To detect the signal, our spectrometer is tuned to $\omega_{\mathrm{det}} \approx \omega_{\mathrm{VIS}} + \omega_{\mathrm{IR}}$. Thus, we detect the signal at the frequencies $\omega_{\mathrm{sig}} \approx \omega_{\mathrm{VIS}} + \omega_{\mathrm{IR}} \pm \omega_{\mathrm{THz}}$. Thus, the frequency of the incoming IR and VIS pulse, as well as the frequency of the emitted signal, must have the same sign. This means that, in the Feynman diagrams, the IR, VIS and signal interaction have to be all on the

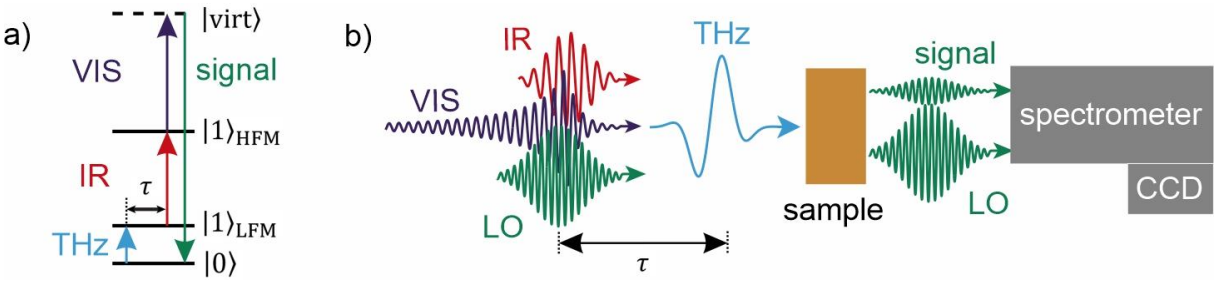

Fig. 2.3 2D TIRV schematics. a) Energy level scheme. b) Experimental implementation.

same side of the density matrix. As a result, for resonant cases, from the eight excitation pathways in Fig. 2.2, only the pathways a) and b) (and their complex conjugates g) and h)) remain.

For a full description with Feynman diagrams, where the system is described as a density matrix, an energy-level scheme is needed. We assume a five-level system (see Fig. 2.5), with one ground state $|0\rangle_{\mathrm{LFM}}|0\rangle_{\mathrm{HFM}}$, the excited LFM $|1\rangle_{\mathrm{LFM}}|0\rangle_{\mathrm{HFM}}$, the excited HFM $|0\rangle_{\mathrm{LFM}}|1\rangle_{\mathrm{HFM}}$, both modes excited $|1\rangle_{\mathrm{LFM}}|1\rangle_{\mathrm{HFM}}$ and a virtual electronic state $|virt\rangle$, that can be accessed with the VIS beam.

Figure 2.4 shows the two Feynman pathways a) and b) from Fig. 2.2, which are observed with 2D TIRV spectroscopy. In total, they become four different excitation pathways due to the five energy levels. Both states where the HFM is occupied ($|0\rangle_{\mathrm{LFM}}|1\rangle_{\mathrm{HFM}}$ and $|1\rangle_{\mathrm{LFM}}|1\rangle_{\mathrm{HFM}}$) can

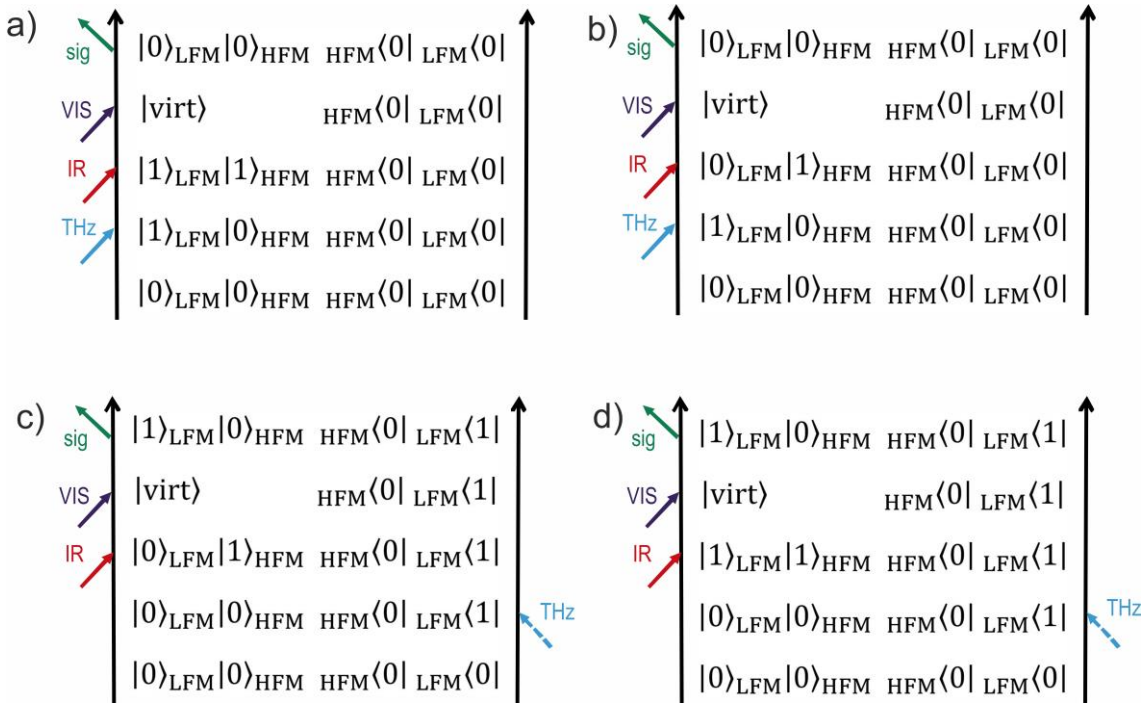

Fig. 2.4 The four possible Feynman pathways in 2D TIRV spectroscopy.

be accessed with the IR beam. However, there are four more complex conjugates pathways (corresponding to the pathways g) and h) of Fig. 2.2), but they are not different in nature. Note that we only considered resonant cases, where $\omega_i \approx (\epsilon_i - \epsilon_{i-1})/\hbar$.

Another graphical representation of the response function in Eq. (2.23) is provided by energy ladder diagrams, shown in Fig. 2.5 [68]. Their basis is the energy level scheme for the considered system. The time runs from left to right, and an arrow that points from the initial to the final state indicates each interaction with an electric field. Solid arrows describe the evolution of the ket, whereas dotted arrows describe the bra. Again, only the pathways detected in 2D TIRV spectroscopy are shown.

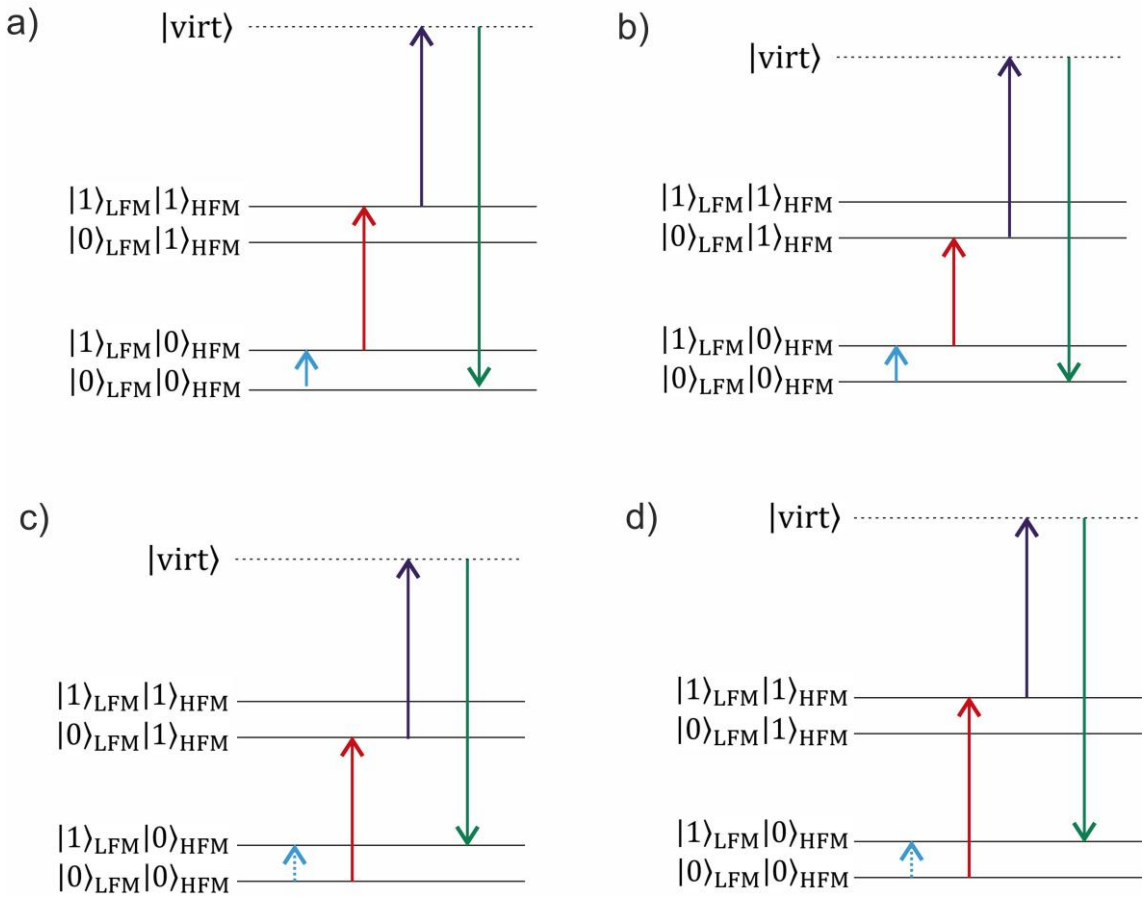

Fig. 2.5 The four possible pathway shown as energy ladder diagram.

2.6 Theoretical derivation of the 2D TIRV spectrum

The Feynman diagrams in the previous section provide a graphical description of the light-matter interactions in 2D TIRV spectroscopy. However, they do not describe the experimentally obtained spectrum. The 2D TIRV spectrum is a function of the frequencies Ω_1 and Ω_2 that correspond to the frequency of the coherence after the first and the second interaction, respectively. Thus, they represent the LFM and HFM, respectively. Both frequencies can be accessed experimentally by measuring the emitted signal field $E_{\mathrm{sig}}(\omega_{\mathrm{sig}}, \tau)$ (see section 3.2). The frequency Ω_2 can be derived from the detected frequency

ω_{sig} by subtracting the frequency of the narrowband visible pulse: $\Omega_2 = \omega_{\mathrm{sig}} - \omega_{\mathrm{VIS}}$. In contrast, the frequency Ω_1 is obtained by a Fourier transformation of the acquired data along a varied time delay τ of the THz pulse relative to the IR/VIS pulse pair (see Fig. 2.3).

However, we will start with the experimentally observable spectrum $E_{\mathrm{sig}}(\Omega_1, \Omega_3)$ as a function of Ω_1 and Ω_3. The frequency Ω_3 is the frequency of the detected signal ω_{sig}. The spectrum is given by a Fourier transformation of the electric signal field $E_{\mathrm{sig}}(\tau, t)$ in the time domain, which is a function of the varied time delay τ and the time t:

$$\begin{aligned} E_{\mathrm{sig}}(\Omega_1, \Omega_3) &= \int d\tau \int dt\, e^{i\Omega_1 \tau}\, e^{-i\Omega_3 t}\, E_{\mathrm{sig}}(\tau, t) \\ &\propto \int d\tau \int dt\, e^{i\Omega_1 \tau}\, e^{-i\Omega_3 t}\, P_{\mathrm{sig}}^{(3)}(\tau, t). \end{aligned} \tag{2.24}$$

We use here that the emitted electric signal field is proportional to the generated third-order polarization $P_{\mathrm{sig}}^{(3)}(t)$ (Eq. (2.8)). This third-order polarization is given by [43]:

$$\begin{aligned} P_{\mathrm{sig}}^{(3)}(t) = \int_0^\infty d\omega_1 \int_0^\infty d\omega_2 \int_0^\infty d\omega_3\, e^{-i(\omega_1+\omega_2+\omega_3)t}\, E_3(\omega_3) E_2(\omega_2) E_1(\omega_1) \\ \times S^{(3)}(\omega_3 + \omega_2 + \omega_1, \omega_2 + \omega_1, \omega_1). \end{aligned} \tag{2.25}$$

The frequencies ω_1, ω_2 and ω_3 are the frequencies of the first, second, and third interacting field, respectively, and can be positive as well as negative. For 2D TIRV, the electric fields are $E_1 = E_{\mathrm{THz}}$, $E_2 = E_{\mathrm{IR}}$ and $E_3 = E_{\mathrm{VIS}}$. The information about the material in which the four-wave mixing process takes place, is included in the response function $S^{(3)}$ (Eq. (2.22)). Since the phase of the THz field depends parametrically on the timing of the pulse τ ($E_{\mathrm{THz}}(\omega_1, \tau) = E_{\mathrm{THz}}(\omega_1)\, e^{-i\omega_1 \tau}$), the phase $e^{-i\omega_1 \tau}$ needs to be added. This yields

$$\begin{aligned} E_{\mathrm{sig}}(\Omega_1, \Omega_3) \propto \int d\tau \int dt \int_0^\infty d\omega_1 \int_0^\infty d\omega_2 \int_0^\infty d\omega_3\, e^{i\Omega_1 \tau}\, e^{i\Omega_3 t}\, e^{-i(\omega_1+\omega_2+\omega_3)t} \\ \times E_{\mathrm{VIS}}(\omega_3) E_{IR}(\omega_2) E_{\mathrm{THz}}(\omega_1)\, S^{(3)}(\omega_3 + \omega_2 + \omega_1, \omega_2 + \omega_1, \omega_1) \\ \times e^{-i\omega_1 \tau}. \end{aligned} \tag{2.26}$$

The integration over $d\tau$ and dt can now be performed by using $\int e^{ixy} dx = \delta(y)$:

$$\begin{aligned} E_{\mathrm{sig}}(\Omega_1, \Omega_3) \propto \int_0^\infty d\omega_1 \int_0^\infty d\omega_2 \int_0^\infty d\omega_3\, \delta(\Omega_3 - \omega_3 - \omega_2 - \omega_1)\, \delta(\Omega_1 - \omega_1) \\ \times E_{\mathrm{VIS}}(\omega_3) E_{\mathrm{IR}}(\omega_2) E_{\mathrm{THz}}(\omega_1)\, S^{(3)}(\omega_3 + \omega_2 + \omega_1, \omega_2 + \omega_1, \omega_1). \end{aligned} \tag{2.27}$$

For $E_{\mathrm{VIS}}(\omega_3)$, an infinitely narrow peak in the frequency domain is assumed, which can either have positive or negative frequencies. Therefore, $E_{\mathrm{VIS}}(\omega_3) = \delta(\Omega_{\mathrm{VIS}} - \omega_3) + \delta(\Omega_{\mathrm{VIS}} + \omega_3)$ with $\Omega_{\mathrm{VIS}} > 0$. We then evaluate one integral after another by using $\int dx\, f(x)\, \delta(a - x) = f(a)$, and get [65,69]

$$\begin{aligned} E_{\mathrm{sig}}(\Omega_1, \Omega_3) \propto\ & E_{\mathrm{IR}}(\Omega_3 - \Omega_{\mathrm{VIS}} - \Omega_1) E_{\mathrm{THz}}(\Omega_1)\, S^{(3)}(\Omega_3, \Omega_3 - \Omega_{\mathrm{VIS}}, \Omega_1) \\ & + E_{\mathrm{IR}}(\Omega_3 + \Omega_{\mathrm{VIS}} - \Omega_1) E_{\mathrm{THz}}(\Omega_1)\, S^{(3)}(\Omega_3, \Omega_3 + \Omega_{\mathrm{VIS}}, \Omega_1). \end{aligned} \tag{2.28}$$

On one side, the 2D TIRV spectrum depends on the response function at the respective frequencies, but also on the intensity of the incoming pulses of the respective electric fields. As our IR spectrum is tuned to $\Omega_{\mathrm{IR}} \approx \pm(|\Omega_3| - |\Omega_{\mathrm{VIS}}|)$, to be resonant with the HFM (remember $|\Omega_1| \ll |\Omega_2|$ and $\Omega_{\mathrm{VIS}} > 0$), for $\Omega_3 > 0$ there is no intensity of the incoming IR pulse at $\omega_{\mathrm{IR}} = \Omega_3 + \Omega_{\mathrm{VIS}} - \Omega_1$ ($E_{\mathrm{IR}}(\Omega_3 + \Omega_{\mathrm{VIS}} - \Omega_1) = 0$). Thus, for $\Omega_3 > 0$ this results in

$$E_{\mathrm{sig}}(\Omega_1, \Omega_3 > 0) \propto E_{\mathrm{IR}}(\Omega_3 - \Omega_{VIS} - \Omega_1) E_{\mathrm{THz}}(\Omega_1)\, S^{(3)}(\Omega_3, \Omega_3 - \Omega_{\mathrm{VIS}}, \Omega_1). \tag{2.29}$$

We can now replace the frequency Ω_3 by the more intuitive frequency Ω_2 that represents the HFM. For this we use $\Omega_2 = \Omega_3 - \Omega_{\mathrm{VIS}}$ (remember $\Omega_{\mathrm{VIS}} > 0$) and get the more intuitive spectrum $E_{\mathrm{sig}}(\Omega_1, \Omega_2 > 0)$, where Ω_1 represents the LFMs and Ω_2 the HFMs:

$$E_{\mathrm{sig}}(\Omega_1, \Omega_2 > 0) = E_{\mathrm{IR}}(\Omega_2 - \Omega_1) E_{\mathrm{THz}}(\Omega_1)\, S^{(3)}(\Omega_2 + \Omega_{\mathrm{VIS}}, \Omega_2, \Omega_1). \tag{2.30}$$

However, this does not mean that Ω_2 equals the frequency of the HFM in all cases. Rather we see that Ω_2 is the sum of the frequency of the IR and the THz beam ($\Omega_2 = \omega_{\mathrm{IR}} \pm \omega_{\mathrm{THz}}$). Thus Ω_2 can be the frequency of the HFM, but not necessarily.

The same considerations can be performed for $\Omega_3 < 0$, however leading to slightly different results. For $\Omega_3 < 0$, we have $E_{\mathrm{IR}}(\Omega_3 - \Omega_{\mathrm{VIS}} - \Omega_1) = 0$, so that

$$E_{\mathrm{sig}}(\Omega_1, \Omega_3 < 0) = E_{\mathrm{IR}}(\Omega_3 + \Omega_{VIS} - \Omega_1) E_{\mathrm{THz}}(\Omega_1)\, S^{(3)}(\Omega_3, \Omega_3 + \Omega_{\mathrm{VIS}}, \Omega_1). \tag{2.31}$$

For $\Omega_2 < 0$, using $\Omega_2 = \Omega_3 + \Omega_{\mathrm{VIS}}$, this leads to

$$E_{\mathrm{sig}}(\Omega_1, \Omega_2 < 0) = E_{\mathrm{IR}}(\Omega_2 - \Omega_1) E_{\mathrm{THz}}(\Omega_1)\, S^{(3)}(\Omega_2 - \Omega_{\mathrm{VIS}}, \Omega_2, \Omega_1). \tag{2.32}$$

The total signal field E_{tot}, including positive as well as negative frequencies Ω_2, is then the sum of the two spectra in Eqs. (2.30) and (2.32):

$$E_{\mathrm{tot}}(\Omega_1, \Omega_2) = E_{\mathrm{sig}}(\Omega_1, \Omega_2 > 0) + E_{\mathrm{sig}}(\Omega_1, \Omega_2 < 0). \tag{2.33}$$

These two terms will interfere at the detector and so far cannot be separated. Thus, the different signals will also interfere in the spectrum, making the analysis of the data challenging. In chapter 4, we will show how it is possible to separate both terms and therefore simplify the analysis significantly.

3 METHODS

3.1 LINEAR INFRARED SPECTROSCOPY

For the measurement of the linear absorption spectra, we use a Fourier-Transform InfraRed (FTIR) spectrometer. Compared to dispersive techniques, FTIR spectroscopy has a better signal-to-noise ratio as well as a higher spectral resolution [27,70].

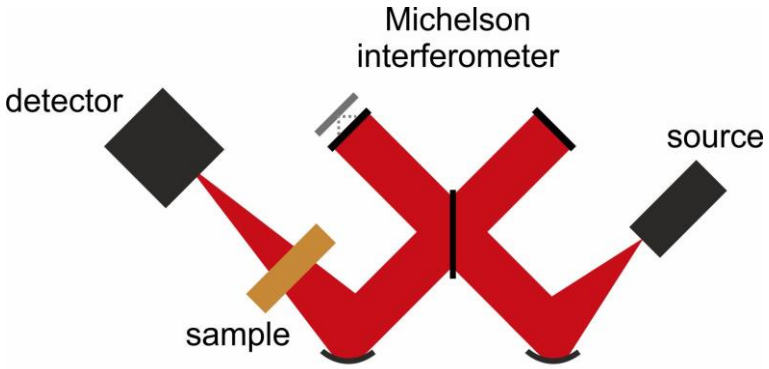

Fig. 3.1 Schematics of an FTIR spectrometer [70].

An FTIR spectrometer, shown in Fig. 3.1, consists of a light source that emits a broadband electromagnetic field. This electromagnetic field passes a Michelson interferometer, where it is split into two beams. Both beams are reflected by a mirror, travel back and are recombined. They interact with the sample and their interference is detected afterwards. This interference is detected as a function of the time delay. The time delay is generated by different beam pathway lengths in the Michelson interferometer. The acquired data in the time domain is Fourier transformed and leads to a spectrum that shows the intensity as a function of frequency. This measured intensity can be compared with the intensity without the sample (reference), and thereby the absorbance α can be calculated [70]:

$$\alpha = \log\left(\frac{I_{\mathrm{ref}}}{I_{\mathrm{sample}}}\right). \tag{3.1}$$

For the measurements in this work, we use a commercial spectrometer (Bruker Vertex 70), which is extended to measure in the frequency range from 30 to $6000\ \mathrm{cm}^{-1}$. This allows measuring the linear absorption spectra of both modes, LFMs and HFMs, in the THz and mid-infrared range, respectively. For the THz absorption spectra, we use a homemade sample cell with two silicon wafers ($0.5\ \mathrm{mm}$ thick) as windows. In between them, we placed a $\sim 10\ \mu\mathrm{m}$ thin Teflon sheet as spacer. For the absorption spectra of the HFMs in the mid-IR range, another sample cell is used to avoid a saturation in the spectra. To this end, we put the sample between two CaF_2 windows, pressed together in a mount without any spacer. However, this causes different thicknesses of the samples. Therefore, afterwards the spectra in the mid-IR and THz range were overlapped at the frequency of the OH-bending mode ($1650\ \mathrm{cm}^{-1}$), to scale the mid-IR spectrum.

3.2 TWO-DIMENSIONAL TERAHERTZ-INFRARED-VISIBLE SPECTROSCOPY

In 2D TIRV spectroscopy, we measure the coupling between LFMs and HFMs. We are aiming at a 2D spectrum, where the axes Ω_1 corresponds to the LFMs, while the second axes Ω_2 corresponds to the HFMs. To this end, we need to generate a signal, which is enhanced by both resonances. For this, we use a four-wave mixing process of a THz, IR and VIS beam (see Fig. 2.3). The broadband THz (IR) beam excites a coherence of the LFM (HFM) in the sample. The visible beam upconverts the system. After the interaction with all three beams, the signal at the frequency $\omega_{\mathrm{sig}} = \omega_{\mathrm{VIS}} + \omega_{\mathrm{IR}} \pm \omega_{\mathrm{THz}}$ is emitted. For details of this interaction and the resulting spectrum, see sections 2.5 and 2.6.

From the measured signal frequency ω_{sig}, we can derive the frequency Ω_2 of the spectrum by subtracting the frequency of the narrowband VIS beam ($\Omega_2 = \omega_{\mathrm{sig}} - \omega_{\mathrm{VIS}} = \omega_{\mathrm{IR}} \pm \omega_{\mathrm{THz}}$). In contrast, to measure the coherence of the LFM, we induce a time delay between the THz and the IR/VIS pulse pair. This time delay is varied, and the so detected signal for each frequency Ω_2 is Fourier transformed. This leads to the resolution of the spectrum along the frequency Ω_1. To perform this Fourier transformation, the signal needs to be detected heterodyned. To this end, we generate a local oscillator (LO) at the sum-frequency of the IR and VIS beam that interferes at the camera with the signal field. We measure the intensity

$$I_{\mathrm{sig}} = E_{\mathrm{LO}}^2 + 2E_{\mathrm{LO}}E_{\mathrm{sig}} + E_{\mathrm{sig}}^2 \tag{3.2}$$

that results from the interference of the electric fields of the LO (E_{LO}) and the signal (E_{sig}). To derive the signal field E_{sig} from this measured intensity I_{sig}, we need to measure the LO field separately. To increase the signal-to-noise ratio, we measure the signal and the LO differentially: a chopper (CH, Fig. 3.2) is used to chop every second THz pulse, and a vibrating motorized mirror (VM) separates the signal and the single LO field on two different rows of the camera. Thus, the LO intensity E_{LO}^2 can be subtracted. We neglect the intensity of the signal E_{sig}^2, as we ensure $E_{\mathrm{sig}} \ll E_{\mathrm{LO}}$. The residual term $2E_{\mathrm{sig}}E_{\mathrm{LO}}$ is shown in the 2D TIRV spectra.

However, for accurate data processing in the way it is described above, the phase of the measured signal needs to be stable. Consequently, the phase of all incoming pulses relative to each other needs to be stable. For this reason, all three beams are generated from the output of the same Ti:Sapphire laser ($5\ \mathrm{mJ/pulse}$, $1\ \mathrm{kHz}$ repetition rate and $60\ \mathrm{nm}$ FHWM). The output is split into three beams that generate the IR, VIS and THz beam, respectively. From the first beam ($1\ \mathrm{mJ/pulse}$), a commercial TOPAS with a NDFG (non-collinear difference frequency generation) unit generates a broadband mid-IR beam. Its central frequency is tunable, and the FWHM is $\sim 300\ \mathrm{cm}^{-1}$. This broadband mid-IR beam is combined with the narrowband VIS beam, generated from the second beam. Before it is combined with the mid-IR beam it passed a 4*f* pulse shaper [71], which reduces the bandwidth of a fraction of the Ti:Sapphire output to $\sim 1\ \mathrm{nm}$. After their combination, the IR/VIS pulse pair generates the local oscillator (LO). In the different experiments in this work, this generation was performed in different ways. Thus, the exact generation is discussed in each chapter separately.

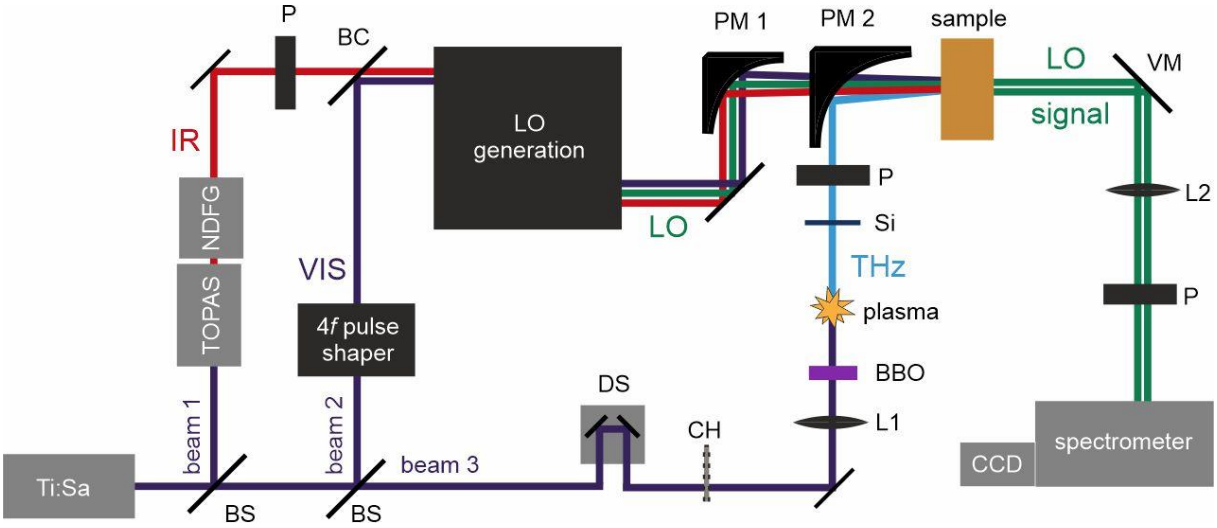

Fig. 3.2 Experimental 2D TIRV setup showing the beam pathway of the IR, VIS and THz pulse. BS: beam splitter, P: polarizer, BC: beam combiner, DS: delay stage, CH: chopper, L: lens, Si: silicon wafer, PM: parabolic mirror, VM: vibrating motorized mirror.

To generate the THz beam, the third 800 nm beam is focused and passes through a $100\ \mu m$ thick type I BBO crystal that generates the second harmonic at $400\ nm$. Both beams are focused (lens L1) and generate a gas plasma that emits a broadband THz pulse [72,73]. The spectrum of the THz pulse is shown in Fig. 3.3. A silicon wafer (Si) in the subsequent beam pathway blocks the 800 nm and 400 nm beams, while it passes the THz pulse. Two parabolic mirrors (PM) collimate and then focus the THz beam at the sample position, where the IR/VIS pulse pair is focused as well. The beams interact via the above-described four-wave mixing process with the sample, and a signal is emitted. This signal as well as the LO beam are collimated with a lens (L2) and travel through the spectrometer to the CCD camera, where the

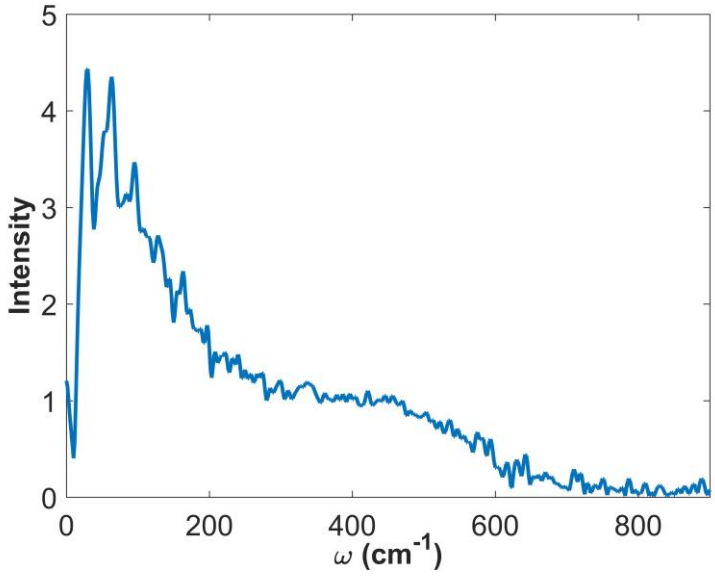

Fig. 3.3 Spectrum of electric field of the THz pulse, measured using terahertz-field-induced second harmonic generation [74–77].

signal is detected in a frequency-resolved manner. Polarizers (P) in all beam pathways allow a selective detection of specific polarization combinations of the incoming and emitted fields. However, in this work, we only considered the case when all beams are polarized horizontally.

The experimental implementation of 2D TIRV spectroscopy described here reflects the state at the beginning of my PhD project in 2017. At this time, the data acquisition and processing did not allow to separate positive and negative frequencies of Ω_2. Consequently, excitation pathways with different signs of the frequency Ω_2 (see section 2.5) could not be separated, the interpretation of the 2D TIRV spectra was very challenging. We developed a procedure for a separation of these excitation pathways, which is described in chapter 4. It is shown that a time delay between the emitted signal and the local oscillator can help to distinguish the excitation pathways in different quadrants of the spectrum. The developed procedure is applied to various model samples (chapter 4) as well as to the spectra of the aqueous salt solutions in chapters 5 and 6.

4 DISTINGUISHING DIFFERENT EXCITATION PATHWAYS IN 2D TIRV SPECTROSCOPY

Contributions to this chapter: All authors conceived the project. L. Vietze constructed the experimental setup and performed the 2D TIRV measurements. All authors discussed the results and contributed to the manuscript.

Paper manuscript is in preparation.

4.1 INTRODUCTION

Infrared vibrational spectroscopy is often used to study ultrafast dynamics on a nanometer length scale in condensed phase substances. For example, homogeneous line broadening and spectral diffusion of a vibrational chromophore reflect the rates of local structure fluctuations and are measured in linear infrared absorption spectroscopy and non-linear two-dimensional infrared (2D IR) spectroscopy [47,78,79]. Another example is the decay of the vibrational excitation anisotropy, which is measured in transient absorption spectroscopy. In the absence of intermolecular energy transfer, the anisotropy decay is caused by the reorientation of a vibrational chromophore due to intra- and/or intermolecular motions, and, thus, reflects the rate of molecular rotation in the densely packed environment of the condensed phase [80,81]. The typical time scale of molecular reorientation and molecular structure fluctuations measured by vibrational spectroscopy is in the range of a few tens of femtoseconds to several picoseconds. The energies of such motions are in the terahertz frequency range ($< 1000\ \mathrm{cm}^{-1}$) and they constitute low-frequency modes of a sample. Generally speaking, the capability of infrared vibrational spectroscopy to reveal the molecular dynamics is due to the coupling between a high-frequency vibrational chromophore (O-H, N-H, C=O, C= N stretch etc.) and low-frequency intra- and intermolecular motions. Thus, infrared vibrational spectroscopy employs a high-frequency mode (HFM) and measures its coupling with the low-frequency modes (LFMs) of molecular motions to reveal the latter. The measurement of the HFM-LFM coupling, in this case, is implemented indirectly, i.e., by probing the state of the HFM only. To measure the coupling directly, we have recently developed two-dimensional Terahertz-InfraRed-Visible (2D TIRV) spectroscopy [65,82]. In 2D TIRV spectroscopy, we excite LFMs and HFMs using broadband terahertz (THz) and mid-infrared (IR) pulses, respectively. Coupled LFM and HFM resonances enhance the mixing of the THz and IR fields, which is then reflected in the signal emitted by a sample. We have previously used 2D TIRV spectroscopy to measure the coupling in liquid water and organic-inorganic perovskites [65,82]. However, in these previous implementations of 2D TIRV spectroscopy, we could not separate distinct excitation pathways. Mixing of different excitation pathways complicates the spectra significantly. To facilitate the analysis of the experimental data, signals generated by different excitation pathways need to be separated. In this work, we develop a procedure to separate these different signals and plot them individually in the two-dimensional spectrum.

Mixing of signals generated by different excitation pathways is common in different spectroscopy techniques. Sometimes such mixing can be beneficial. A prominent example is absorption spectroscopy, where mixing of signals from two complex conjugate pathways

produces an absorption spectrum, rather than a dispersion or mixed absorption-dispersion spectrum. A similar advantage - obtaining an absorptive spectrum - is achieved in 2D IR spectroscopy by mixing signals from the rephasing and non-rephasing excitation pathways [83]. In contrast, in 2D TIRV spectroscopy (similar to 2D Raman-THz spectroscopy [84] and 2D DOVE spectroscopy [85]), excitation pathways are neither rephasing nor non-rephasing, and their superposition cannot produce an absorptive spectrum. Instead, such a superposition generates an interference pattern, which is challenging to interpret, as illustrated by the 2D TIRV spectrum of liquid water in Fig. 4.1. It shows a complicated pattern and a minimum intensity at $\Omega_2 \approx 3250\ \mathrm{cm}^{-1}$ due to the interference of different excitation pathways, as proposed in [65].

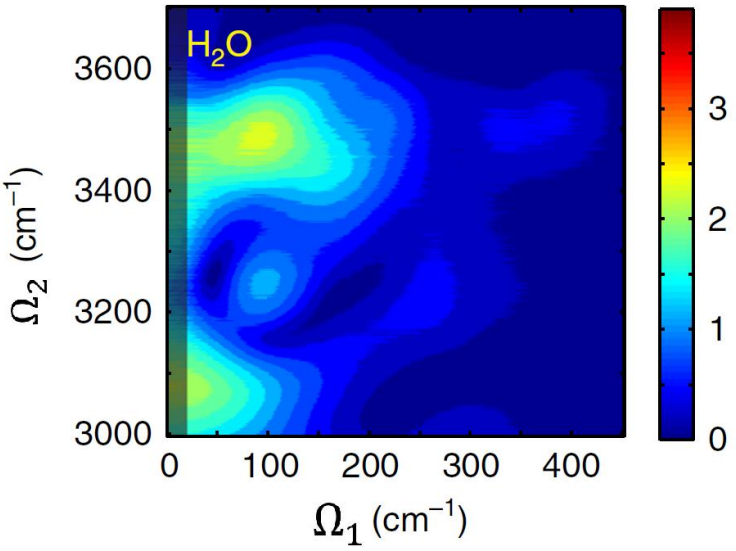

Fig. 4.1 Absolute-value 2D TIRV spectrum of H_2O, reproduced from Ref. [65]. Note the different local maxima in the signal, which can be shown to originate from the interference of distinct excitation pathways.

Consequently, to simplify the spectrum, we need to separate excitation pathways via coherence states with positive and negative frequencies, which all are excited in 2D TIRV spectroscopy [65,69]. A similar need to separate signals produced by coherences with positive and negative frequencies appears in phase-resolved sum-frequency generation (SFG) spectroscopy. In SFG spectroscopy, the separation allows extracting the real (dispersive) and imaginary (absorptive) parts of the optical susceptibility [86,87]. We adapt this approach of phase-resolved SFG spectroscopy to 2D TIRV spectroscopy. In the theoretical section below, we consider the principles of 2D TIRV spectroscopy and formulate a procedure to separate the signals from the different excitation pathways. We validate this procedure using CaF_2 and nitrogen gas as two model samples. After validating the approach, we use it to obtain the dispersive and absorptive components of the 2D TIRV response of liquid water, and thereby verify the previous interpretation of the 2D TIRV spectrum of liquid water.

4.2 PRINCIPLES OF 2D TIRV SPECTROSCOPY

Here, we describe the principles of 2D TIRV spectroscopy only briefly, more details can be found elsewhere [65,69]. 2D TIRV spectroscopy employs broadband terahertz (THz), broadband mid- infrared (IR) and narrowband visible (VIS) pulses to excite a sample. These interactions generate a signal that is spectrally resolved and detected. In general, interactions of the sample with THz and IR pulses can be resonant as well as non-resonant. Resonant interactions enhance the 2D TIRV signal, and such enhancement appears in different quadrants of the two-dimensional spectrum for different excitation pathways. To illustrate this, we consider an example of a simple five-level system in Fig. 4.2. The system is composed of two sub-systems corresponding to the high- and low-frequency oscillators. The high-frequency oscillator is represented by its ground and excited vibrational states $|0\rangle_{\mathrm{HFM}}$ and $|1\rangle_{\mathrm{HFM}}$, respectively. Similarly, the states $|0\rangle_{\mathrm{LFM}}$ and $|1\rangle_{\mathrm{LFM}}$ represent the low-frequency oscillator. Hence, the states of the complete system are $|i\rangle_{\mathrm{LFM}}|j\rangle_{\mathrm{HFM}}$ $(i, j = 0,1)$. In addition to the vibrational states the system has a virtual state $|\mathrm{virt}\rangle$, which represents the non-resonant electron excitation (polarizability). When such a system interacts with the THz, IR and VIS pulses, the excitation pathways are represented by four distinct Feynman/ energy ladder diagrams in Fig. 4.2 (there are another four complex conjugate pathways, which contain the same information about the system) [43,47,68]. The THz pulse excites a transition between the ground and excited states of the low-frequency oscillator. After the THz excitation, the IR pulse promotes a transition to the vibrationally excited state of the high-frequency oscillator. The IR transition can conserve the state of the LFM (diagrams A and C) or change it (diagrams B and D). We did not find any evidence for contributions of other pulse orderings (e.g., the interaction with the IR beam before the interaction with the THz beam).

A general view of a 2D TIRV spectrum is shown in Fig. 4.3. The signal is plotted as a function of the THz excitation frequency ω_1 and combined THz and IR excitation frequency ω_2. The latter, ω_2 axis, is the frequency of a coherence state that is excited in a sample after the interaction with both THz and IR pulses. The excitation pathways of Fig. 4.2 appear in the 2D TIRV spectrum at different positions. The signals generated by the pathways A-D and their complex conjugates A*-D* are shown schematically in Fig. 4.3 a). The signal generated via pathways A and B oscillates at positive frequencies ω_1 and ω_2 after THz and IR excitations, respectively. This signal appears in the first, upper right quadrant of the spectrum. In contrast, the signals generated via pathways C and D oscillate at a negative frequency ω_1 and positive frequency ω_2 and appear in the second quadrant of the spectrum. Another distinction is the location of the signals A and B in the first quadrant. Whereas both of these signals have the same frequency ω_1, their ω_2-frequencies are different. The frequency ω_2 of pathway B equals the frequency of the HFM vibration. The frequency ω_2 of pathway A equals the sum of the frequencies of HFM and LFM. Thus, the resonant signal A appears shifted to higher frequency relative to the frequency of the HFM. In the second quadrant, signal D is located at the frequency ω_1 of the LFM and the frequency ω_2 of the HFM, whereas the signal generated via pathway C has a ω_2-frequency equal to the difference of the HFM and LFM frequencies. In general, the resonant 2D TIRV signal has a ω_2-frequency of the HFM when the two-quantum transition (transition when the excitation of both LFM and HFM changes) happens at interaction with the IR pulse. As shown in Fig. 4.3 a), the complex conjugate pathways A*, B*, C* and D* oscillate with the same ω_1- and ω_2-frequencies as the pathways A-D, with,

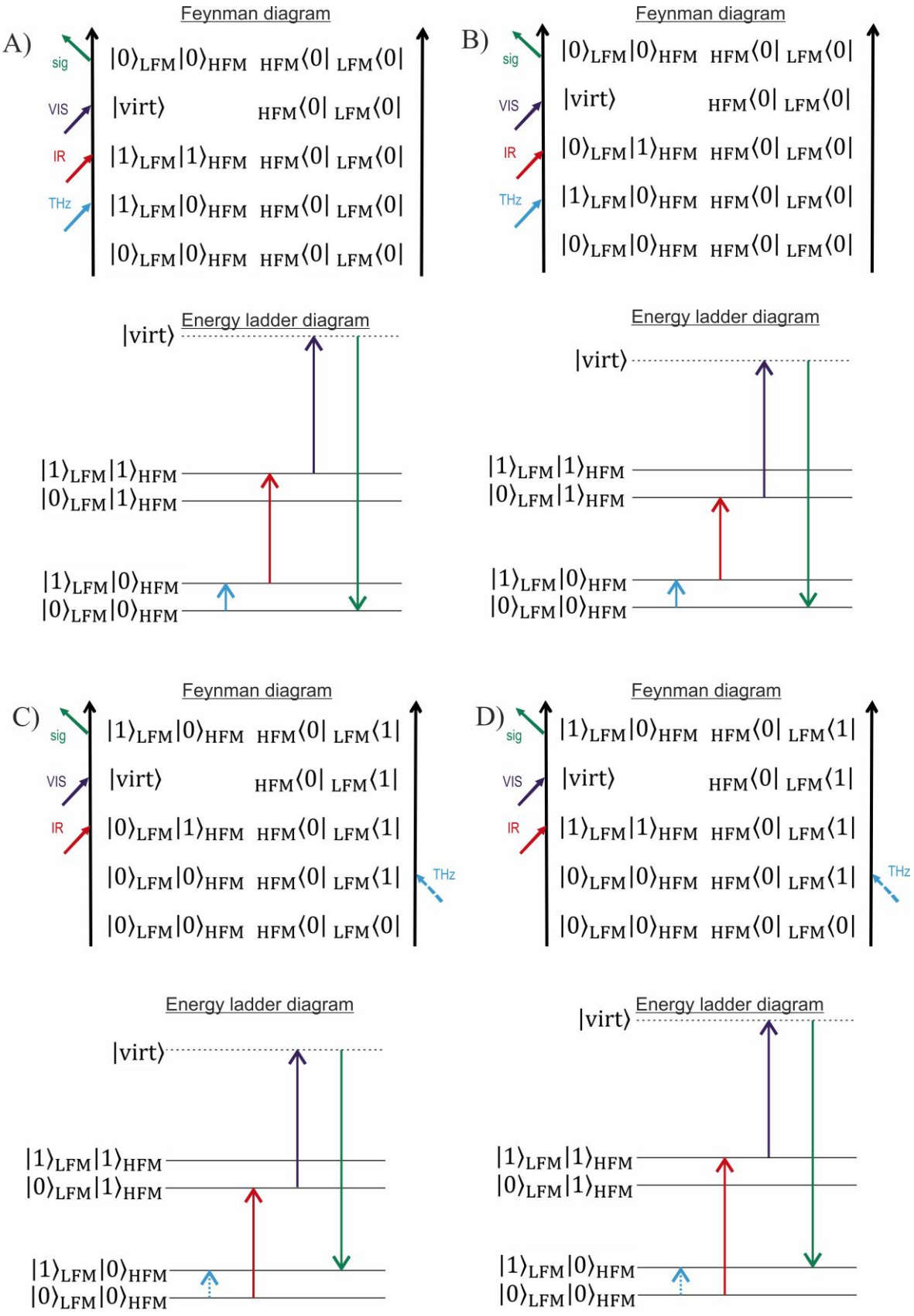

Fig. 4.2 Excitation pathways for 2D TIRV spectroscopy. The top and bottom rows show the graphical representation using Feynman and energy ladder diagrams, respectively.

however, opposite sign. Accordingly, signals generated via pathways A*/ B* and C*/D* appear in the third and fourth quadrants, respectively.

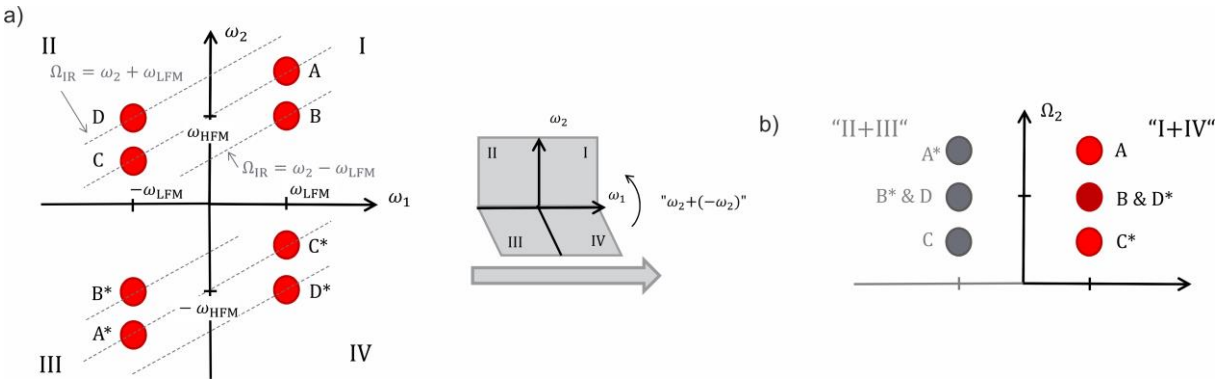

Fig. 4.3 Schematic 2D TIRV spectrum. a) Signals generated by excitation pathways A-D in Fig. 4.2 and their complex conjugate pathways A*-D* are shown in four quadrants of a 2D TIRV spectrum. The dashed lines show points in the spectrum, for which the signal is generated by the same IR frequency. b) The 2D TIRV spectrum, which results from the superposition of quadrants I and IV, as illustrated by the grey cartoon between panels a) and b). In b), the superposition of quadrants II and III is shown in grey.

We note that the ω_2-frequency of the 2D TIRV signal never coincides with the IR frequency (Ω_{IR}) that promotes the transition of the HFM. This is due to the 2D TIRV excitation taking place only via coherence states, and is in contrast to, e.g., 2D IR spectroscopy, which employs a population state as well. For instance, for pathway A in Fig. 4.2, the IR frequency equals that of the HFM, and the signal appears at a higher ω_2 frequency. Signal B appears at the frequency of the HFM, but is generated by IR light with a frequency lower than the HFM frequency. Depending on the excitation pathway, the IR frequency can be also higher than ω_{HFM}, which is the case for pathway D. Therefore, in 2D TIRV spectroscopy, a resonant peak can have a ω_2-frequency of the HFM, but never the frequency of the IR light that generates the signal (Table 4.1). However, for small ω_1, the difference between the IR and ω_2-frequencies is small.

Table 4.1 Frequencies ω_1, ω_2 and Ω_{IR} as a function of ω_{LFM} and ω_{HFM} for the different excitation pathways in 2D TIRV spectroscopy.

pathway	A	B	C	D
ω_1	ω_{LFM}	ω_{LFM}	$-\omega_{LFM}$	$-\omega_{LFM}$
ω_2	$\omega_{HFM} + \omega_{LFM}$	ω_{HFM}	$\omega_{HFM} - \omega_{LFM}$	ω_{HFM}
Ω_{IR}	ω_{HFM}	$\omega_{HFM} - \omega_{LFM}$	ω_{HFM}	$\omega_{HFM} + \omega_{LFM}$

With the experimental approach of our previous work, we were not able to separate all four quadrants of a 2D TIRV spectrum. This limitation stems from how the ordinate axis of the 2D spectrum was derived. In our previous experiments, this frequency was obtained by

subtracting frequency of the VIS pulse from frequency of the signal, $\Omega_2 = \Omega_{\mathrm{sig}} - \Omega_{\mathrm{VIS}}$. Hence, Ω_2 cannot be negative and we distinguish it from ω_2 in a), which can be both positive and negative. In our previous work, we analyzed the superposition of the first and fourth quadrants of the spectrum [65,82], as it is shown schematically in Fig. 4.3 b). In the present work, we elaborate a quadrant separation procedure, which enables the derivation of the ω_2-frequency and thus splits the total 2D TIRV spectrum into the sum and difference frequency generation components (between the IR and THz fields). For the resonant signal, this partitioning isolates different excitation pathways in different quadrants of the spectrum (Fig. 4.3 a)), which facilitates their analysis.

4.3 Theoretical description of the quadrant separation procedure in 2D TIRV spectroscopy

In 2D TIRV spectroscopy, we measure the spectrum by four-wave mixing of a broadband terahertz (THz), a broadband mid-infrared (IR), and a narrowband visible (VIS) pulse in the sample. We use heterodyne detection and measure the interference of the signal and local oscillator (LO) pulses at the detector. After processing the data, the 2D TIRV spectrum Γ is given by (Eqs. (2.30), (2.32) and (2.33)):

$$\begin{aligned}\Gamma(\Omega_2 + \Omega_{\mathrm{VIS}}, \Omega_1) \propto\ & S^{(3)}(\Omega_2 + \Omega_{\mathrm{VIS}}, \Omega_2, \Omega_1) E_{\mathrm{THz}}(\Omega_1) E_{\mathrm{IR}}(\Omega_2 - \Omega_1) E^0_{\mathrm{VIS}} \\ & E_{\mathrm{LO}}(-\Omega_2 - \Omega_{\mathrm{VIS}}) \\ & + S^{(3)}(-\Omega_2 - \Omega_{\mathrm{VIS}}, -\Omega_2, \Omega_1) E_{\mathrm{THz}}(\Omega_1) E_{\mathrm{IR}}(-\Omega_2 - \Omega_1) \\ & E^0_{\mathrm{VIS}}{}^{*} E_{\mathrm{LO}}(\Omega_2 + \Omega_{\mathrm{VIS}}),\end{aligned} \tag{4.1}$$

where $E_{\mathrm{THz}}(\omega)$, $E_{\mathrm{IR}}(\omega)$, $E_{\mathrm{LO}}(\omega)$ are the spectra of the THz, IR and LO pulses, respectively. The VIS pulse is approximated by an infinitely narrow spectrum with the frequency $\Omega_{\mathrm{VIS}} > 0$ and the amplitude $\left|E^0_{\mathrm{VIS}}\right|$. $S^{(3)}(\omega_3, \omega_2, \omega_1)$ is the frequency-dependent third-order non-linear optical response function of the sample. The coordinate Ω_1 of the two-dimensional spectrum Γ reflects the LFM coherence excited by the THz pulse. The coordinate Ω_2 reflects the coherence excited by the IR pulse, which is either HFM or HFM+LFM state depending on the excitation pathway (see alsoTable 4.1).

In Eq. (4.1), we use capital Ω to denote frequencies and distinguish these variables from the small ω in the previous section for the following reason: It is important that the frequencies Ω_1 and Ω_2 are derived in different ways in the experiment. The coordinate Ω_1 is obtained by a Fourier transformation of the acquired data along the varied time delay of the THz pulse relative to the IR/VIS pulse pair. It can be positive as well as negative ($-\infty < \Omega_1 < +\infty$). Thus, the response function $S^{(3)}(\dots, \dots, \Omega_1 > 0)$ and $S^{(3)}(\dots, \dots, \Omega_1 < 0)$ appears in the different quadrants $\Gamma(\dots, \Omega_1 > 0)$ and $\Gamma(\dots, \Omega_1 < 0)$ of the 2D TIRV spectrum, respectively. In contrast, the coordinate Ω_2 is obtained from the frequency of the detected signal by subtracting Ω_{VIS}. The frequency of the signal is measured by a grating-based spectrometer and is positive-valued. Thus, the coordinate Ω_2 is positive ($\Omega_2 > 0$) in Eq. (4.1). The inability of the grating-based spectrometer to separate positive and negative frequencies causes the mixing of the two parts of the response function, $S^{(3)}_{+} = S^{(3)}(\dots, \Omega_2, \dots)$ and $S^{(3)}_{-} = S^{(3)}(\dots, -\Omega_2, \dots)$, in the 2D TIRV spectrum (schematically shown in Fig. 4.3 b)). These two parts, similar to the

rephasing and non-rephasing spectra in 2D IR spectroscopy, have different physical meanings and need to be separated.

To separate $S_+^{(3)}$ and $S_-^{(3)}$ we adopt the method developed for phase-resolved SFG spectroscopy [86]. Phase-resolved SFG spectroscopy makes use of an increased time delay between the LO and signal pulses at the detector. A selecting Fourier transformation of the interference between the LO and signal allows separating the $\chi^{(2)}$ and $\chi^{(2)^*}$ parts of the spectrum. Below we show that by using a similar procedure for 2D TIRV spectroscopy, we can likewise separate the different parts, $S_+^{(3)}$ and $S_-^{(3)}$, of the measured response function.

When the LO pulse, $E_{\mathrm{LO}}(t)$ is shifted in time by Δ, its spectrum is modulated by a linear phase shift. In our notation, the electric field of the shifted pulse $E'_{\mathrm{LO}}(t) = E_{\mathrm{LO}}(t+\Delta)$ and $\Delta > 0$ corresponds to a LO pulse that arrives at the detector at an earlier times. The 2D TIRV spectrum measured with the offset LO pulse is given by

$$\begin{aligned}\Gamma(\Omega_2+\Omega_{\mathrm{VIS}},\Omega_1) \propto\ & S^{(3)}(\Omega_2+\Omega_{\mathrm{VIS}},\Omega_2,\Omega_1)\\ & E_{\mathrm{THz}}(\Omega_1)E_{\mathrm{IR}}(\Omega_2-\Omega_1)E^0_{VIS}E_{\mathrm{LO}}(-\Omega_2-\Omega_{\mathrm{VIS}})e^{i(\Omega_2+\Omega_{\mathrm{VIS}})\Delta}\\ & +S^{(3)}(-\Omega_2-\Omega_{\mathrm{VIS}},-\Omega_2,\Omega_1)\\ & E_{\mathrm{THz}}(\Omega_1)E_{\mathrm{IR}}(-\Omega_2-\Omega_1){E^0_{\mathrm{VIS}}}^*E_{\mathrm{LO}}(\Omega_2+\Omega_{\mathrm{VIS}})e^{-i(\Omega_2+\Omega_{\mathrm{VIS}})\Delta}.\end{aligned} \tag{4.2}$$

To separate the $S_+^{(3)}$ and $S_-^{(3)}$ parts of the response function, we perform a Fourier transformation of the spectrum Γ along the spectrometer frequency $\Omega_2+\Omega_{\mathrm{VIS}}$:

$$\begin{aligned}\Gamma(x,\Omega_1) \propto\ & \int_{-\infty}^{+\infty} d(\Omega_2+\Omega_{\mathrm{VIS}})\ S^{(3)}(\Omega_2+\Omega_{VIS},\Omega_2,\Omega_1)E_{\mathrm{THz}}(\Omega_1)E_{\mathrm{IR}}(\Omega_2-\Omega_1)\\ & E^0_{\mathrm{VIS}}E_{\mathrm{LO}}(-\Omega_2-\Omega_{\mathrm{VIS}})e^{i(\Omega_2+\Omega_{\mathrm{VIS}})\Delta}e^{-i(\Omega_2+\Omega_{\mathrm{VIS}})x}\\ & +\int_{-\infty}^{+\infty} d(\Omega_2+\Omega_{\mathrm{VIS}})\,S^{(3)}(-\Omega_2-\Omega_{VIS},-\Omega_2,\Omega_1)E_{\mathrm{THz}}(\Omega_1)E_{\mathrm{IR}}(-\Omega_2-\Omega_1)\\ & {E^0_{\mathrm{VIS}}}^*E_{\mathrm{LO}}(\Omega_2+\Omega_{\mathrm{VIS}})e^{-i(\Omega_2+\Omega_{\mathrm{VIS}})\Delta}e^{-i(\Omega_2+\Omega_{\mathrm{VIS}})x}.\end{aligned} \tag{4.3}$$

In phase-resolved SFG spectroscopy, a similar transformation is often considered as a transformation of the signal from the frequency (spectrum) back to the time domain (pulse) [86]. We can write the hybrid time-frequency function $\Gamma(x,\Omega_1)$ as composed of the two terms A' (for Ω_2) and A'' (for $-\Omega_2$)

$$\Gamma(x,\Omega_1) = A'(x-\Delta,\Omega_1) + A''(x+\Delta,\Omega_1). \tag{4.4}$$

Here $A'(x,\Omega_1)$ is given by

$$\begin{aligned}A'(x,\Omega_1) \propto\ & \int_{-\infty}^{+\infty} d(\Omega_2+\Omega_{\mathrm{VIS}})\ S^{(3)}(-\Omega_2-\Omega_{VIS},-\Omega_2,\Omega_1)\\ & E_{\mathrm{THz}}(\Omega_1)E_{\mathrm{IR}}(\Omega_2-\Omega_1)E^0_{\mathrm{VIS}}E_{\mathrm{LO}}(-\Omega_2-\Omega_{\mathrm{VIS}})e^{-i(\Omega_2+\Omega_{\mathrm{VIS}})x}\end{aligned} \tag{4.5}$$

and $A''(x,\Omega_1)$ by

$$A''(x,\Omega_1) \propto \int_{-\infty}^{+\infty} d(\Omega_2+\Omega_{\mathrm{VIS}})\, S^{(3)}(-\Omega_2-\Omega_{\mathrm{VIS}},-\Omega_2,\Omega_1) \\ E_{\mathrm{THz}}(\Omega_1)E_{\mathrm{IR}}(-\Omega_2-\Omega_1){E^0_{\mathrm{VIS}}}^{*}E_{\mathrm{LO}}(\Omega_2+\Omega_{\mathrm{VIS}})e^{-i(\Omega_2+\Omega_{\mathrm{VIS}})x}. \tag{4.6}$$

In principle, the response functions $S_{+}^{(3)}$ and $S_{-}^{(3)}$ can be obtained by the inverse Fourier transformation of $A'(x,\Omega_1)$ and $A''(x,\Omega_1)$, respectively. For any physical response function $S^{(3)}$ and electromagnetic fields E_{THz}, E_{IR} and E_{LO} the functions $A'(x,\Omega_1)$ and $A''(x,\Omega_1)$ are non-zero only for a certain range of $x=[-a,+a]$ as it is schematically shown in Fig. 4.4 a). It is also likely that these functions overlap within the range $x=[-a,+a]$, and thus cannot be separated. However, in the time-frequency function $\Gamma(x,\Omega_1)$ the time delay Δ of the LO pulse shifts A' and A'' in opposite directions along the coordinate axis x (Eq. (4.4), Fig. 4.4 b)). In principle, for any physical $A'(x,\Omega_1)$ and $A''(x,\Omega_1)$ we can find a value of the time delay Δ that will separate them. For this Δ, the range $x=[-a+\Delta,+a+\Delta]$, where $A'(x-\Delta,\Omega_1)$ is non-zero, and the range $x=[-a-\Delta,+a-\Delta]$, where $A''(x+\Delta,\Omega_1)$ is non-zero, do not overlap.

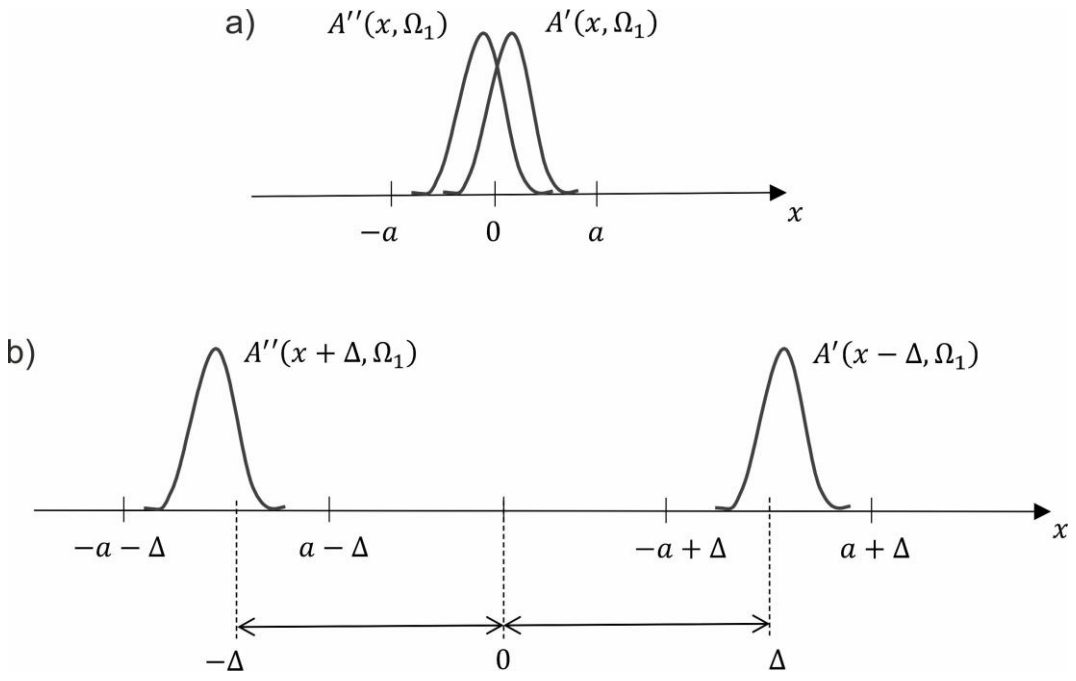

Fig. 4.4 Schematic visualization of the functions $A'(x,\Omega_1)$ and $A''(x,\Omega_1)$ as a function of the variable x (panel a) and their position along the coordinate axis x after introducing a time delay Δ (panel b).

When $A'(x-\Delta,\Omega_1)$ and $A''(x+\Delta,\Omega_1)$ are separated, we can perform their inverse Fourier transformation over the coordinate x separately and obtain the spectra $\Gamma'(\omega,\Omega_1)$ and $\Gamma''(\omega,\Omega_1)$:

$$\Gamma'(\omega,\Omega_1)=\int_{-a+\Delta}^{+a+\Delta} A'(x-\Delta,\Omega_1)e^{i\omega x}dx=\int_{-\infty}^{+\infty} A'(x-\Delta,\Omega_1)e^{i\omega x}dx, \tag{4.7}$$

$$\Gamma''(\omega,\Omega_1) = \int_{-a-\Delta}^{+a-\Delta} A''(x+\Delta,\Omega_1)\, e^{i\omega x} dx = \int_{-\infty}^{+\infty} A''(x+\Delta,\Omega_1)\, e^{i\omega x} dx. \tag{4.8}$$

By substituting Eq. (4.5) into Eq. (4.7), we obtain

$$\begin{aligned}
\Gamma'(\omega,\Omega_1) \propto & \int_{-\infty}^{+\infty}\int_{-\infty}^{+\infty} d(\Omega_2+\Omega_{\mathrm{VIS}})\, dx\; S^{(3)}(-\Omega_2-\Omega_{\mathrm{VIS}},-\Omega_2,\Omega_1) \\
& E_{\mathrm{THz}}(\Omega_1)E_{\mathrm{IR}}(\Omega_2-\Omega_1)E^0_{\mathrm{VIS}}E_{\mathrm{LO}}(-\Omega_2-\Omega_{\mathrm{VIS}})e^{-i(\Omega_2+\Omega_{\mathrm{VIS}})(x-\Delta)}e^{i\omega x} \\
= & \int_{-\infty}^{+\infty} d(\Omega_2+\Omega_{\mathrm{VIS}})\; S^{(3)}(-\Omega_2-\Omega_{VIS},-\Omega_2,\Omega_1) \\
& E_{\mathrm{THz}}(\Omega_1)E_{\mathrm{IR}}(\Omega_2-\Omega_1)E^0_{\mathrm{VIS}}E_{\mathrm{LO}}(-\Omega_2-\Omega_{\mathrm{VIS}}) \\
& e^{i(\Omega_2+\Omega_{\mathrm{VIS}})\Delta}\int_{-\infty}^{-\infty} e^{-i(\Omega_2+\Omega_{\mathrm{VIS}})x}e^{i\omega x}dx \\
= & \int_{-\infty}^{+\infty} d(\Omega_2+\Omega_{\mathrm{VIS}})\, S^{(3)}(-\Omega_2-\Omega_{\mathrm{VIS}},-\Omega_2,\Omega_1) \\
& E_{\mathrm{THz}}(\Omega_1)E_{\mathrm{IR}}(\Omega_2-\Omega_1)E^0_{\mathrm{VIS}}E_{\mathrm{LO}}(-\Omega_2-\Omega_{\mathrm{VIS}}) \\
& e^{i(\Omega_2+\Omega_{\mathrm{VIS}})\Delta}\delta(\omega-\Omega_2-\Omega_{\mathrm{VIS}}) \\
= & S^{(3)}(-\Omega_2-\Omega_{\mathrm{VIS}},-\Omega_2,\Omega_1)E_{\mathrm{THz}}(\Omega_1)E_{\mathrm{IR}}(\Omega_2-\Omega_1)E^0_{\mathrm{VIS}} \\
& E_{\mathrm{LO}}(-\Omega_2-\Omega_{\mathrm{VIS}})e^{i(\Omega_2+\Omega_{\mathrm{VIS}})\Delta}\Big|_{\Omega_2+\Omega_{\mathrm{VIS}}=\omega}.
\end{aligned} \tag{4.9}$$

Equation (4.9) can be written as

$$\begin{aligned}
\Gamma'(\Omega_2+\Omega_{\mathrm{VIS}},\Omega_1) \propto & S^{(3)}(-\Omega_2-\Omega_{\mathrm{VIS}},-\Omega_2,\Omega_1)E_{\mathrm{THz}}(\Omega_1)E_{\mathrm{IR}}(\Omega_2-\Omega_1)E^0_{\mathrm{VIS}} \\
& E_{\mathrm{LO}}(-\Omega_2-\Omega_{\mathrm{VIS}})e^{i(\Omega_2+\Omega_{\mathrm{VIS}})\Delta}.
\end{aligned} \tag{4.10}$$

Similarly, by substituting Eq. (4.6) into Eq. (4.8) we obtain for $-\Omega_2$

$$\begin{aligned}
\Gamma''(\Omega_2+\Omega_{\mathrm{VIS}},\Omega_1) \propto & S^{(3)}(-\Omega_2-\Omega_{\mathrm{VIS}},-\Omega_2,\Omega_1)E_{\mathrm{THz}}(\Omega_1)E_{\mathrm{IR}}(-\Omega_2-\Omega_1){E^0_{\mathrm{VIS}}}^* \\
& E_{\mathrm{LO}}(\Omega_2+\Omega_{\mathrm{VIS}})e^{-i(\Omega_2+\Omega_{\mathrm{VIS}})\Delta}.
\end{aligned} \tag{4.11}$$

Equations (4.10) and (4.11) show that after the inverse Fourier transformation the two parts $S_+^{(3)}$ and $S_-^{(3)}$ of the spectrum of the response function are separated in the corresponding spectra Γ' and Γ''.

The considerations above can be boiled down into the following quadrant separation (QS) procedure to separate the two parts of the response function:

1. Create a time delay for the LO pulse relative to the signal pulse.
2. Measure the 2D TIRV data in the time domain by varying the time delay between the THz pulse and the IR/VIS pulse pair. For each time delay heterodyned, frequency-resolved detection is employed.

3. Perform the Fourier transformation for the acquired time-domain data to obtain the frequency domain spectrum $\Gamma(\Omega_2 + \Omega_{\mathrm{VIS}}, \Omega_1)$.
4. For the spectrum $\Gamma(\Omega_2 + \Omega_{\mathrm{VIS}}, \Omega_1)$, perform the Fourier transformation over the frequency axis $\Omega_2 + \Omega_{\mathrm{VIS}}$ to obtain the hybrid time-frequency domain functions $A'(x - \Delta, \Omega_1)$ and $A''(x + \Delta, \Omega_1)$.
5. Perform the inverse Fourier transformation separately for the functions $A'(x - \Delta, \Omega_1)$ and $A''(x + \Delta, \Omega_1)$ by applying proper window functions. The transformation generates the spectra $\Gamma'(\Omega_2 + \Omega_{\mathrm{VIS}}, \Omega_1)$ and $\Gamma''(\Omega_2 + \Omega_{\mathrm{VIS}}, \Omega_1)$.

After implementing the QS procedure, we can plot the new spectrum $\tilde{\Gamma}$ as a function of the variables ω_1 and ω_2, which can be positive and negative:

$$\tilde{\Gamma}(\omega_2, \omega_1) = \begin{cases} \Gamma'(\omega_2 + \Omega_{\mathrm{VIS}}, \omega_1), \omega_1 > 0, \omega_2 > 0 \text{ (quadrant I)} \\ \Gamma'(\omega_2 + \Omega_{\mathrm{VIS}}, \omega_1), \omega_1 < 0, \omega_2 > 0 \text{ (quadrant II)} \\ \Gamma''(-\omega_2 + \Omega_{\mathrm{VIS}}, \omega_1), \omega_1 < 0, \omega_2 < 0 \text{ (quadrant III)} \\ \Gamma''(-\omega_2 + \Omega_{\mathrm{VIS}}, \omega_1), \omega_1 > 0, \omega_2 < 0 \text{ (quadrant IV).} \end{cases} \tag{4.12}$$

The new spectrum $\tilde{\Gamma}$ is composed of four quadrants, each of which represents the corresponding quadrant of the response function $S^{(3)}$ (convoluted with the spectra of the THz, IR and LO pulses). Only two of these four quadrants contain different information, and quadrants I (II) and III (IV) contain complex conjugate data.

To explain the nature of the signal in the different quadrants of the 2D TIRV spectrum, we consider Eqs. (4.10)-(4.12) in more detail. We seek to determine how signal frequency relates to frequencies of the THz and IR fields. This relationship is given by the variable frequency Ω_2 in Eqs. (4.10) and (4.11). In the previous section, the frequency Ω_2 is defined as the difference between the signal frequency and frequency Ω_{VIS} of the VIS pulse (see [65,69]), and from this definition it follows that $\Omega_2 > 0$. We consider the signal in the four quadrants separately:

- **Quadrant I**. The signal is given by Eq. (4.10) with $\Omega_1 > 0$. We denote the frequencies of the THz and IR fields by $\Omega_{\mathrm{THz}} (= |\Omega_1|)$ and $\Omega_{IR} (= |\Omega_2 - \Omega_1|)$, respectively. Using this notation, we can write $\Omega_2 = \Omega_{\mathrm{THz}} + \Omega_{\mathrm{IR}}$. Thus, the signal in the first quadrant is emitted at the sum-frequency of the IR and THz fields.
- **Quadrant II**. The signal is given by Eq. (4.10) with $\Omega_1 < 0$. We obtain $\Omega_2 = \Omega_{\mathrm{IR}} - \Omega_{\mathrm{THz}}$, because for this quadrant $\Omega_1 = -\Omega_{\mathrm{THz}}$. Thus, the signal in the second quadrant is emitted at the difference-frequency of the IR and THz fields.
- **Quadrant III**. The signal is given by Eq. (4.11) with $\Omega_1 < 0$. For this quadrant $\Omega_1 = -\Omega_{\mathrm{THz}}$ and $\Omega_{\mathrm{IR}} = |-\Omega_2 - \Omega_1| = \Omega_2 + \Omega_1$, and we obtain $\Omega_2 = \Omega_{\mathrm{IR}} + \Omega_{\mathrm{THz}}$. Similar to the first quadrant, the signal in the third quadrant is emitted at the sum-frequency of the IR and THz fields.
- **Quadrant IV**. The signal is given by Eq. (4.11) with $\Omega_1 > 0$. For this quadrant $\Omega_1 = \Omega_{\mathrm{THz}}$ and, similar to the third quadrant, $\Omega_{\mathrm{IR}} = |-\Omega_2 - \Omega_1| = \Omega_2 + \Omega_1$. Thus, $\Omega_2 = \Omega_{\mathrm{IR}} - \Omega_{\mathrm{THz}}$ and the signal is emitted at the difference-frequency of the IR and THz fields, which is similar to the second quadrant.

In summary, the signal in quadrants I and III (II and IV) is generated via sum-frequency (difference-frequency) mixing of the THz and IR fields.

4.4 EXPERIMENTAL IMPLEMENTATION

To implement the QS procedure, we modify the experimental setup described in our previous work [65]. The procedure requires an increased time delay between the 2D TIRV signal and LO pulses at the detector. This time delay needs to be stable during the measurements with fluctuations $\ll 1$ fs. To generate and delay a LO with such a high time delay stability, we use a displaced Sagnac interferometer.

A layout of the experimental setup is shown in Fig. 4.5. The output of an amplified Ti:Sapphire laser (5 mJ/pulse, 1 kHz repetition rate, about 60 nm FWHM) is split by the beam splitters BS1 and BS2 into beam 1 (1.0 mJ/pulse), beam 2 (0.8 mJ/pulse) and beam 3 (1.1 mJ/pulse). Beam 1 pumps a commercial TOPAS equipped with a non-collinear difference frequency generation (NDFG) unit. The output of the NDFG is a mid-infrared pulse (IR) with a few microjoules of energy, tunable central frequency, and a typical full width at half maximum of about 300 cm^{-1}. The IR pulse is polarized horizontally with the polarizer P1 and then aligned to the beam combiner BC, where it is overlapped with the horizontally polarized narrowband VIS pulse (about 1nm FWHM). The VIS pulse is generated from beam 2 using a $4f$ pulse shaper with an optical slit as mask [71]. After the beam combiner BC, the IR/VIS pulse pair is aligned to the displaced Sagnac interferometer (DS interferometer) to generate the LO pulse.

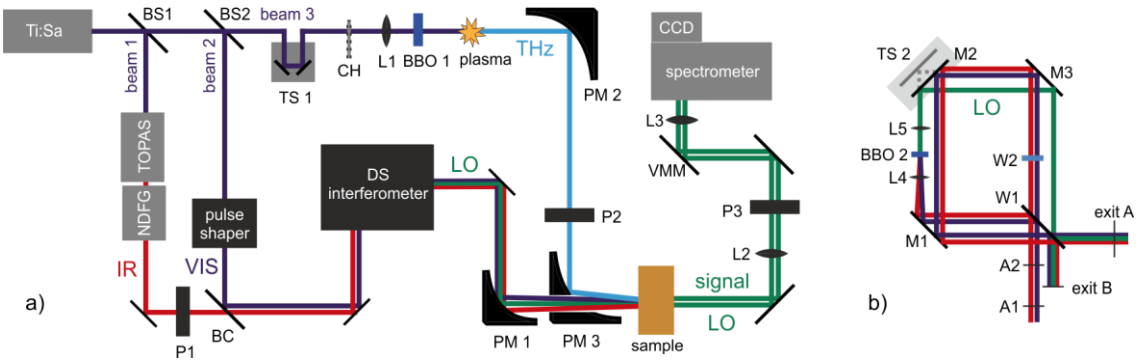

Fig. 4.5 Scheme of a) the experimental setup for 2D TIRV spectroscopy and b) displaced Sagnac interferometer (labeled DS interferometer in panel a)).

The DS interferometer (Fig. 4.5 b)) is composed of a CaF_2 wedge-shaped window W1 and three silver mirrors M1, M2, and M3. Each of these optical elements has a diameter of 2'', and the wedge of the CaF_2 window is 1°. The IR/VIS pulse pair passes through the window W1, with a small fraction reflected from both the front and the back surfaces. We block the reflection from the front surface and align the reflection from the back surface to pass the clockwise pathway in the interferometer. In the clockwise pathway, the lens L4 (CaF_2, $d = 1/2''$, $f = 5$ cm) focuses the IR/VIS light at the crystal BBO 2 (a 10 µm thick type 1 BBO crystal on a 2 mm UVFS substrate, Newlight Photonics Inc.). The light produced by sum-frequency generation of the IR and VIS fields in the crystal is collimated by the lens L5 (NBK7, $d = 1/2''$, $f = 5$ cm, AR coating). The collimated beam follows the clockwise pathway, and a fraction of it is reflected from the window W1. This reflected light is the LO for the 2D TIRV measurements. At exit A of the interferometer, the LO is combined with the main fraction of

the IR/VIS light, which travels the counterclockwise pathway. All three beams, the LO and IR/VIS pulses, are focused by the parabolic mirror PM1 ($d = 1.5''$, $f = 8''$, bare gold), and overlapped with the THz pulse at the sample.

The THz pulse is generated from beam 3. To this end, beam 3 is focused in a nitrogen atmosphere by the lens L1 ($\mathrm{NBK7}, f = 20\ \mathrm{cm}$). Before the focus, beam 3 passes through a $100\ \mu\mathrm{m}$ thick type I BBO crystal (BBO1) to generate its second harmonic. The focused light ionizes the nitrogen gas, and the non-linear mixing of beam 3 and its second harmonic in the plasma generates a broadband THz pulse [72,73]. The spectrum is shown in Fig. 3.3. The emitted THz pulse is collimated by the parabolic mirror PM2, polarized horizontally by the polarizer P2 and focused by the parabolic mirror PM3 at the sample (PM2 and PM3 are 90° off-axis parabolic mirror with a protected silver coating).

The THz, IR, and VIS pulses interact with the sample, and four-wave mixing of these three fields generates the signal field. The signal propagates together with the LO, which passes through the sample. Lens L2 ($f = 25\ \mathrm{cm}$) collimates the signal and LO field, and both beams are focused on the entrance slit of the spectrometer (Acton SP2300) by lens L3 ($d = 2''$, $f = 10\ \mathrm{cm}$). After passing the spectrometer, they are detected by a CCD camera (Andor Newton 971 EMCCD). We use polarizer P3 to select horizontal polarization of the signal field.

To enhance the sensitivity of the experiment, we measure the signal differentially. To this end, we use a chopper CH (Thorlabs MC2000B with blade MC2F57) to modulate the THz beam at the rate of 500 Hz and a vibrating motorized mirror (galvanometer) VMM to separate the LO and LO plus signal field into two rows 1 and 2 at the chip of the CCD camera. The measured intensity in those two rows is given by:

$$I_1 = E_{\mathrm{LO}}^2 \tag{4.13}$$

and

$$I_2 = E_{\mathrm{LO}}^2 + 2E_{\mathrm{LO}}E_{\mathrm{sig}} + E_{\mathrm{sig}}^2, \tag{4.14}$$

where E_{LO} and E_{sig} are amplitudes of electric field of the LO and signal, respectively. The difference $I_2 - I_1$of these two signals contains the intensity of the signal field E_{sig}^2 and the interference term between the signal and LO fields $2E_{\mathrm{LO}}E_{\mathrm{sig}}$.

To align the DS interferometer, we use an alignment laser and the following procedure. We start with the Sagnac interferometer in its non-displaced configuration and align the alignment beam through the irises A1 and A2 (Fig. 4.5 b)). Then, we overlap the clock- and counterclockwise beam pathways inside the interferometer by observing the alignment beam on a paper card. Next, we displace the mirror M2, which is installed on the horizontal translation stage TS 2, to offset the clock- and counterclockwise beam pathways (as shown in Fig. 4.5 b)). Then, we improve the collinearity of the clock- and counterclockwise pathways by monitoring the interference at the exit B of the interferometer. When the two pathways are collinear, we mark the position of the clockwise beam close to the mirror M2 and install the lens L4. We adjust the position of L4 by monitoring the beam at the mark. Next, we install the lens L5 and adjust its position by monitoring the interference between the clock- and

counterclockwise beams at exit B. To adjust the time delay between the clock- and counterclockwise beams, we install a $4\ \mathrm{mm}$ thick CaF_2 window W2 in the counterclockwise pathway

4.5 Results and discussion

To validate the approach described in the theoretical section, we use CaF_2 and nitrogen gas as two model samples. Nitrogen gas is often used in terahertz field induced second harmonic (TFISH) generation to measure the time profile of a THz pulse [88,89]. This material represents the case of a non-resonant interaction with all three pulses (THz, IR and VIS) in the frequency range of the present work. In contrast, CaF_2 represents the case of resonant interaction with the THz pulse and a non-resonant interaction with the IR and VIS pulses.

4.5.1 2D TIRV spectroscopy of CaF_2

Figure 4.6 a) shows the time-domain 2D TIRV data measured for a $2\ \mathrm{mm}$ thick CaF_2 window (step 2 of the QS procedure) by scanning the time delay between the THz pulse and the IR/VIS pulse pair. The ordinate axis Ω_2 is obtained by subtracting Ω_{VIS} from the signal frequency. By a Fourier transformation over the horizontal axis of these time-domain data, we obtain the 2D TIRV spectrum in Fig. 4.6 b) (step 3 of the QS procedure). The two peaks in this spectrum at $\Omega_1 = \pm 66\ \mathrm{cm}^{-1}$ correspond to the resonant excitation of the CaF_2 phonon mode by the THz pulse [65,90]. The third peak at $\Omega_1 = 0\ \mathrm{cm}^{-1}$ is generated mainly by the homodyne-detected 2D TIRV signal field (which is the intensity of this electromagnetic wave). The two quadrants I and II in Fig. 4.6 b) contain complex conjugate data: The spectrum in quadrant I is composed of the sum of the two parts of the CaF_2 response function, $S^{(3)}(\Omega_2 + \Omega_{\mathrm{VIS}}, \Omega_2, \Omega_1 > 0)$ and $S^{(3)}(-\Omega_2 - \Omega_{\mathrm{VIS}}, -\Omega_2, \Omega_1 > 0)$ (convoluted with the spectra of the THz, IR and LO pulses, Eq. (4.1)). Similarly, the spectrum in quadrant II is composed of the sum of $S^{(3)}(\Omega_2 + \Omega_{\mathrm{VIS}}, \Omega_2, \Omega_1 < 0)$ and $S^{(3)}(-\Omega_2 - \Omega_{\mathrm{VIS}}, -\Omega_2, \Omega_1 < 0)$. The response along the Ω_2 -axis reflects the bandwidth of the infrared laser pulse.

Figure 4.6 c) shows the hybrid time-frequency data produced by Fourier transformation of the (complex-valued) data in Fig. 4.6 b) over the vertical axis (step 4 of the QS procedure). The peaks α1 and α2, located at $\omega_1 = \mp 66\ \mathrm{cm}^{-1}$ and $x = \pm 4.1\ \mathrm{ps}$, are produced by the interference between the 2D TIRV signal and the LO. These two peaks correspond to the neat 2D TIRV spectrum of CaF_2. The other five peaks (β, γ1, γ2, δ1, and δ2) are artifacts of the measurement. Peak β, located at $\omega_1 = 0\ \mathrm{cm}^{-1}$ and $x = 0\ \mathrm{ps}$, stems from the homodyne-detected 2D TIRV signal field. Peaks γ1 and γ2 are located at $\omega_1 = \mp 66\ \mathrm{cm}^{-1}$ and $x = \pm 0.2\ ps$, which indicates the existence of a second local oscillator pulse. This local oscillator ghost has a $0.2\ ps$ time delay relative to the 2D TIRV signal pulse. The interference between the signal and the LO ghost pulse produces the peaks γ1 and γ2. The peaks δ1 and δ2 are located at $\omega_1 = 0\ \mathrm{cm}^{-1}$ and $x = \pm 3.9\ ps$. The frequency ω_1 of these peaks shows that they are generated by a 2D TIRV signal, which does not oscillate with the time delay between the THz and IR/VIS pulses. The nature of this signal is not yet fully clear to us. However, from the time x of δ1 and δ2, we conclude that they are produced by interference with the LO rather than the LO ghost.

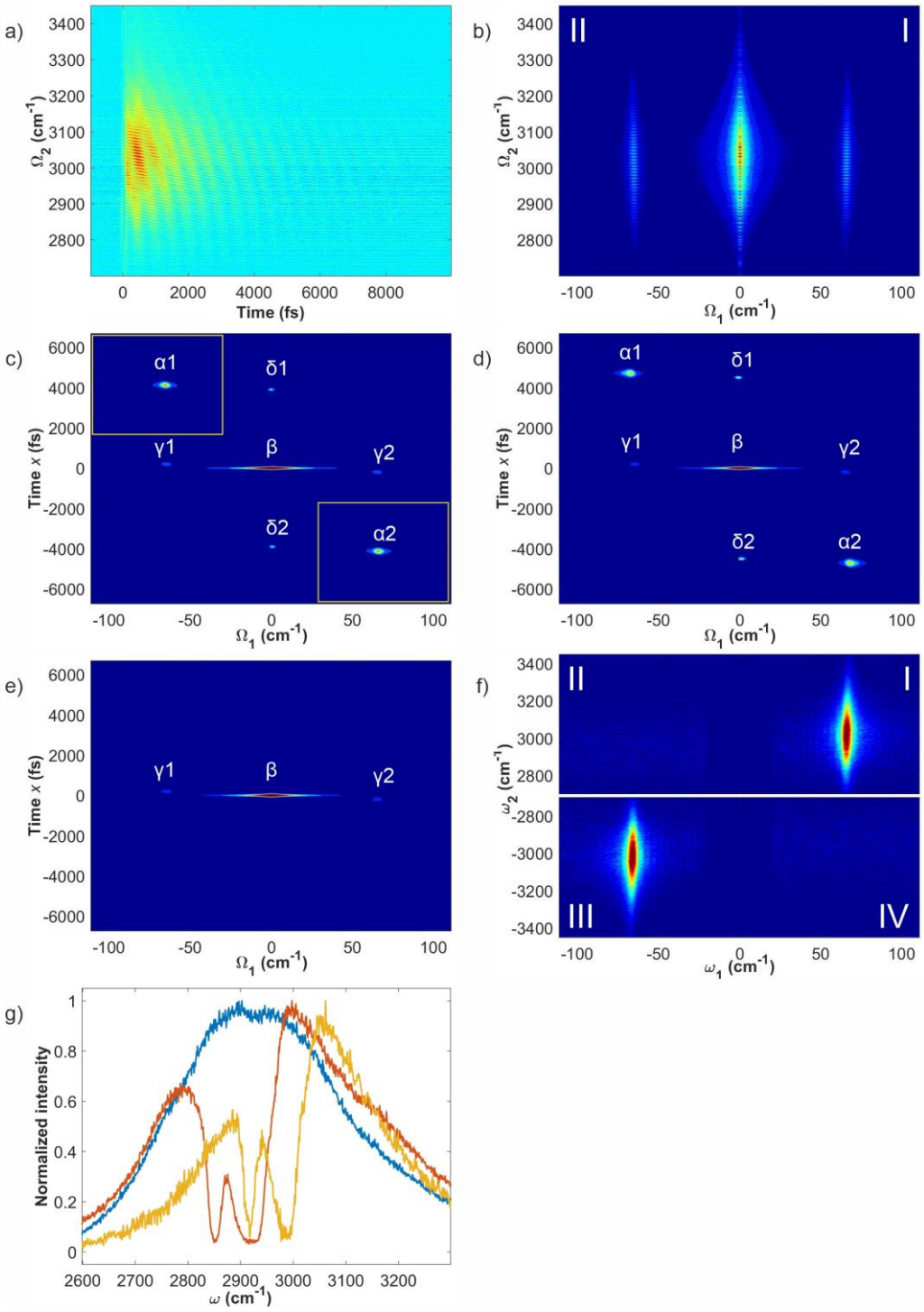

Fig. 4.6 Measured 2D TIRV spectroscopy data of a CaF_2 sample. a) 2D TIRV signal measured for different time delays (horizontal axis) between the THz and IR/VIS pulses (step 2 of the QS procedure). b) Absolute-value 2D TIRV spectrum obtained by Fourier transformation of the data in a) (step 3 of the QS procedure). c) Hybrid time-frequency representation of the 2D TIRV data obtained by Fourier transformation of the data in b) along the vertical axis (step 4 of the QS procedure). d) and e) The same as c) measured with an additional time delay of the LO and blocked LO, respectively. f) Absolute-value 2D TIRV spectrum of CaF2 obtained by inverse Fourier transformation of peaks $\alpha 1$ and $\alpha 2$ in c). g) Profile of the absolute-value 2D TIRV spectrum of CaF_2 along the ω_2 axis measured with modulated IR pulse (yellow line). Blue and red lines show spectra of the original and modulated IR pulses, respectively.

In our setup, we use a collinear geometry, in which the IR and VIS pulses travel together after the BC (Fig. 4.5 a)). Therefore, it is likely that the LO ghost is produced by sum-frequency generation of the IR and VIS pulses upon reflection on one or several of the mirrors on their pathway. To verify the assignment of the peaks in Fig. 4.6 c), we perform two additional measurements. In the first measurement, we install an additional CaF_2 plate of $\approx 0.42\ \mathrm{mm}$ thickness into the LO pathway in the DS interferometer. This plate increases the optical path length to the detector for the LO by about $0.6\ \mathrm{ps}$ and causes a shift of the peaks α1 and α2 to $x = \pm 4.7\ \mathrm{ps}$ as well as the peaks δ1 and δ2 to $x = \pm 4.5\ \mathrm{ps}$ (Fig. 4.6 d)). We note that all other peaks remain at their initial positions. In the second measurement, we block the LO beam in the DS interferometer. This leads to a disappearance of all peaks, except for the peaks β, γ1, and γ2 (Fig. 4.6 e)). The results of these two additional measurements are consistent with the assignment of the peaks.

To implement step 5 of the QS procedure using Eqs. (4.7),(4.8) we need to determine the integration limits $\pm a + \Delta$ and $\pm a - \Delta$ for the functions A' and A'', respectively. To this end, we need to determine the sign of the LO time offset Δ. This sign can be found by comparing the data in Figs. 4.6c) and d). The LO optical path length increases by adding the CaF_2 plate, and simultaneously the time delay between the LO and signal pulses increases. Thus, the LO arrives at the detector after the signal pulse and $\Delta < 0$. Therefore, the inverse Fourier transformation of the peaks α2 (A') and α1 (A'') generates Γ' and Γ'', respectively. We use a rectangular window function to filter out the peaks β, γ1, γ2, δ1 and δ2 before the inverse Fourier transformation (yellow rectangle in Fig. 4.6 c)). Figure 4.6 f) shows the obtained 2D TIRV spectrum for CaF_2 after the last Fourier transformation (step 5 of the QS procedure). In this plot, we use the variables $-\infty < \omega_1, \omega_2 < +\infty$ for the frequency axes. The CaF_2 response appears only in the first and third quadrants of the spectrum, which means that only interactions with $\omega_2 = \Omega_{\mathrm{IR}} + \Omega_{\mathrm{THz}}$ contribute to the signal generation. Such generation can be considered using the pathways A and/or B in Fig. 4.2 with a second virtual state instead of the HFM state.

In order to verify this conclusion, we modulate the spectrum of the IR pulse before it interacts with the sample. We use a thin ($\sim 10\ \mu\mathrm{m}$) polyethylene film to deplete the IR intensity at $2850\ \mathrm{cm}^{-1}$ and $2920\ \mathrm{cm}^{-1}$ by the C-H stretch absorption. Figure 4.6 g) shows a comparison of the original IR spectrum, the modulated IR spectrum and the profile of the 2D TIRV spectrum of CaF_2 along the ω_2-axis, which is measured with the modulated IR spectrum. The depletion of the IR spectrum causes two minima in the 2D TIRV spectrum, which are offset by $+66\ \mathrm{cm}^{-1}$ relative to the frequencies of the C-H vibrations. This offset is exactly the frequency of the phonon resonance excited by the THz pulse. Thus, for CaF_2, the frequency of the signal is given by the sum of the THz and IR (and VIS) frequencies, which confirms the conclusion above that only the excitation pathways A and/or B contribute to the signal generation in the first quadrant.

4.5.2 2D TIRV spectroscopy of nitrogen gas

Figure 4.7 shows the 2D TIRV spectrum of nitrogen gas obtained by using the QS procedure. We show here the spectrum only for positive ω_2 frequencies (quadrants I and II) since quadrants III and IV contain complex conjugate information. In contrast to CaF_2, the nitrogen signal appears only in the second quadrant. The broad line shape of the peak is consistent with

the non-resonant character of the nitrogen response. For the signal to appear in the second quadrant, it should be produced by difference frequency generation between the IR and THz pulses. Indeed, the peak has an apparent slope where higher THz frequencies correspond to lower frequencies of the signal. To better measure the slope of the peak, we use a depleted IR spectrum, similar to the CaF_2 measurements. The absorption lines in the IR spectrum at $2850\ \mathrm{cm}^{-1}$ and $2920\ \mathrm{cm}^{-1}$ cause a depletion of the 2D TIRV spectrum along the lines $\omega_2 = \omega_1 + 2850\ \mathrm{cm}^{-1}$ and $\omega_2 = \omega_1 + 2920\ \mathrm{cm}^{-1}$ (red dashed lines in Fig. 4.7 b)).

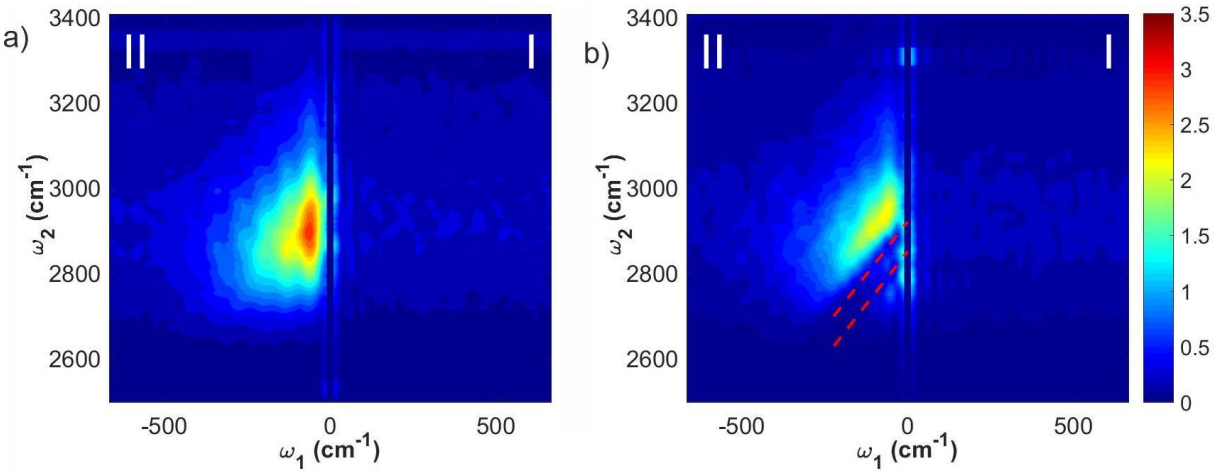

Fig. 4.7 Absolute-value 2D TIRV spectra of nitrogen gas measured using a) the original and b) modulated IR pulse.

In conclusion, the data for CaF_2 and nitrogen gas validate the ability of the QS procedure to separate different excitation pathways in 2D TIRV spectroscopy. We can now use it for substances with more complex 2D TIRV responses, such as liquid water. The 2D TIRV spectrum of liquid water has previously been shown to be very complicated due to the overlay of signals belonging to different quadrants. In the following, we employ the QS procedure to separate the different excitation pathways and disentangle the different contributions to the overall 2D TIRV spectrum of neat H_2O.

4.5.3 2D TIRV spectroscopy of liquid H_2O

Figure 4.8 shows the 2D TIRV spectrum of neat liquid water at room temperature. In contrast to CaF_2 and nitrogen, the response of water appears in all quadrants of the spectrum. The peaks α and β dominating the first and second quadrants are located at ($\omega_1 \approx 125\ \mathrm{cm}^{-1}$, $\omega_2 \approx 3440\ \mathrm{cm}^{-1}$) and ($\omega_1 \approx -125\ \mathrm{cm}^{-1}, \omega_2 \approx 3240\ \mathrm{cm}^{-1}$), respectively. Based on previous work [65], we assign these peaks to the coupling between the intramolecular OH-stretch and intermolecular hydrogen-bond stretch and bending modes. The separation of the different excitation pathways into different quadrants eliminates the characteristic minimum of intensity at $\Omega_2 \approx 3250\ \mathrm{cm}^{-1}$ (Fig. 4.1 and [65]), which is consistent with the interpretation that the minimum originates from the interference of signal of different quadrants. In addition to the peaks α and β, the spectrum contains the peaks γ and δ, which have not been observed before. We assign these peaks to the coupling between the OH-stretch and the librational

modes of water. Detailed investigation of the 2D TIRV spectrum of water is beyond the scope of this chapter, but will be provided in chapter 5 and 6.

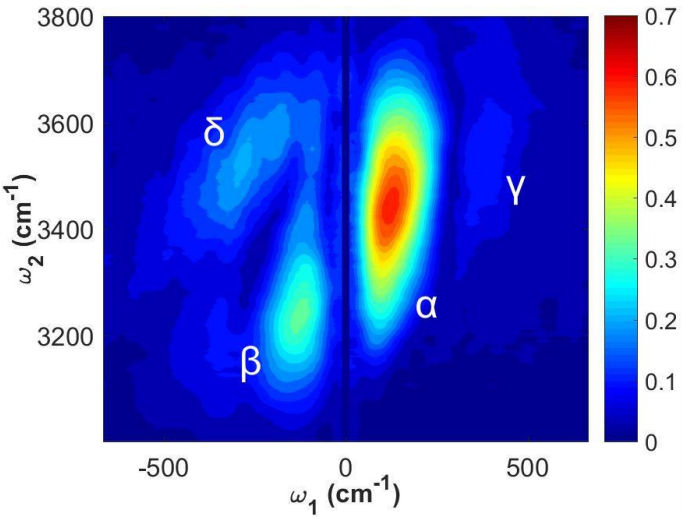

Fig. 4.8 Absolute-value 2D TIRV spectrum of liquid water with separated quadrants (only positive ω_2-frequencies are shown).

4.6 Conclusions

In non-linear spectroscopy that does not excite population states, the interference of different excitation pathways can make the interpretation of the spectra not straightforward. This is particularly true for 2D TIRV spectroscopy, where sum- and difference frequency mixing between infrared and terahertz fields can lead to complex line shapes. The quadrant separation procedure reported here provides a method to disentangle excitation pathways and analyze them separately. Some materials like CaF_2 and N_2 have one dominating type (sum- or difference-) of frequency mixing. Even for such simple cases, the method is useful for determining the excitation pathway producing the signal. It is even more beneficial for samples that generate signals via both sum- and difference-frequency mixing, as illustrated by the case of liquid water. Interestingly, the ratio between sum- and difference-frequency mixing of infrared and terahertz fields varies dramatically for different samples. Further research is needed to explain this phenomenon. Nevertheless, this newly developed quadrant separation procedure in 2D TIRV spectroscopy paves the way for quantitatively studying the coupling between LFMs and HFMs in a wide variety of biological and soft matter.

5 COUPLING BETWEEN THE WATER OH-STRETCH AND THE LIBRATION MODES IN NEAT WATER AND IN THE HYDRATION SHELL OF HALIDE ANIONS

Contributions to this chapter: M. Grechko and M. Bonn conceived the project. L. Vietze and M.G. designed the details and L.V. performed the 2D TIRV and FTIR measurements. P. Seliya collected additional FTIR data. M. G. performed the MD simulations. L. V., J. Hunger., and M.G. developed the model. All authors discussed the results and contributed to the manuscript.

Paper manuscript is in preparation.

5.1 INTRODUCTION

Water is one of the most common substances on earth and plays an important role in many biological, chemical and technical processes [1,8]. In most cases, water acts as a solvent for other substances, from simple charged ions to complex molecules like proteins. These solvation processes, as well as other reactions in water, are driven by the thermodynamic potentials of the water [23]. Those potentials are closely connected to the energy landscape. At room temperature, the thermally populated low-frequency modes (LFM) contribute to it. In water, those LFMs are intermolecular motions of the molecules. These are motions of the molecules relative to each other, which can originate from a translational or rotational degree of freedom. In particular, the energy landscape and thereby also the nature of the LFMs in the direct environment of the solute, determine reaction pathways. A better understanding of LFMs, and therefore of the energy landscape, will lead to a better understanding of the reaction pathways. Furthermore, since the intermolecular dynamics in the collective water network are closely connected to the intramolecular modes [49,63,64], also the coupling to other modes in the direct environment of the solute significantly influences the reactions. In particular, the coupling determines energy dissipation pathways. While much progress has been made in understanding solute-induced changes in the water structure and dynamics, the influence of simple solutes on the coupling between inter- and intramolecular degrees of freedom is still elusive. We will use 2D TIRV to investigate the influence of ions on the coupling between the low-frequency librations and the intramolecular OH-stretch mode.

Ions are one of the most common solutes and can also serve as a model example formore complex charged solutes. With the addition of ions, due to the partial charges of the water molecules, hydrogen bonds are broken, and the tetrahedral structure of the water network is disrupted. At the same time, the water molecules form hydration shells around the ions [13]. This leads to structural changes in the water network and simultaneously alters the dynamics in the hydrogen-bond network. How long-ranging these effects on the structure and dynamics of the water network are, is highly debated. While some publications found that mainly the first hydration shell around the ions is disturbed [19,20], others observed also effects well beyond the first hydration shell [21,22]. However, the influence of the ions on thermodynamic potentials, regulating various processes in water, is non-negligible. Here, we chose a set of potassium salts with the anions chloride, bromide and iodide. We will focus on the influence of the halide anions on the water network, as the one of the potassium cation is known to be small [13,91]. The different anions are all monovalent, but differ in their size

$$Cl^- < Br^- < I^-.$$

Thus, they have different charge densities, what also influences the hydrogen bonds. All of them are weaker than the hydrogen bonds between two water molecules, however the hydrogen bonds with iodide are the weakest. Therefore, we expect iodide to change the structure and dynamics of the water network the most compared to the bulk. We will investigate how these changes alter the coupling between the librational modes and the OH-stretch vibration. We report the direct measurement of this coupling in aqueous salt solutions with 2D TIRV spectroscopy. Linear absorption spectra in the THz and IR range complement the 2D TIRV measurements.

5.2 Results and Discussion

5.2.1 2D TIRV spectroscopy of aqueous solutions of KCl, KBr and KI

Similar to other two-dimensional spectroscopy techniques, 2D TIRV spectroscopy measures the coupling between vibrational modes by probing the third-order non-linear optical response function $S^{(3)}$ of a sample. In the particular case of 2D TIRV spectroscopy, this response function directly discloses the LFM-HFM coupling by resonance peaks in the spectrum. To measure $S^{(3)}$, we use the sample induced optical mixing of terahertz (THz) and mid-infrared (IR) pulses, subsequently upconverted by a visible (VIS) pulse. This mixing is enhanced by both the low- and high-frequency resonances (Fig. 5.1), which are excited by the THz and IR pulses, respectively. The first resonance in the low-frequency range is identical to the LFM of a sample measured by linear absorption spectroscopy. In contrast, the second resonance, which is in the high-frequency range, can be either a HFM or a combination HFM+LFM vibration, depending on the excitation pathway (Fig. 5.1). The 2D TIRV spectrum is plotted against the frequencies of those resonances ω_1 (low) and ω_2 (high). One needs to keep in mind that a measured 2D TIRV spectrum is given by the product of the $S^{(3)}$ spectrum and the spectra of laser pulses used in the experiment. In this work, we plot absolute-value spectra, which reflect the amplitude of the sample response function $S^{(3)}$.

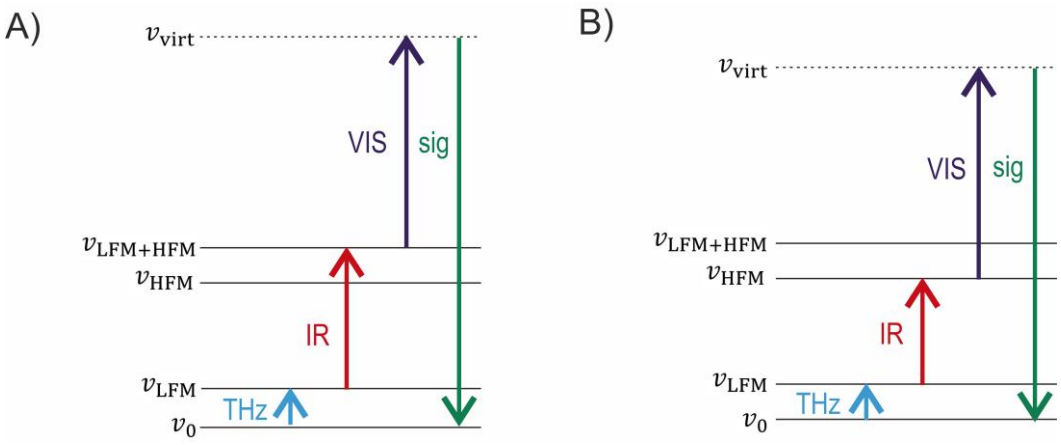

Fig. 5.1 Excitation pathways in 2D TIRV spectroscopy that can contribute to the signal in the first quadrant.

Figure 5.2 shows the first quadrant of the measured absolute-value 2D TIRV spectrum of neat water. The spectrum is composed of two broad peaks: α with a maximum intensity at ($\omega_1 = 80\ \mathrm{cm}^{-1}$, $\omega_2 = 3370\ \mathrm{cm}^{-1}$) and γ with a maximum intensity at ($\omega_1 = 400\ \mathrm{cm}^{-1}$, $\omega_2 = 3480\ \mathrm{cm}^{-1}$). The peaks α and γ are separated by a minimum at $\omega_1 \approx 290\ \mathrm{cm}^{-1}$. This intensity minimum is relatively sharp along the ω_1-axis and broad along the ω_2-axis, and thus indicates that the peaks α and γ overlap and interfere destructively around $\omega_1 = 290\ \mathrm{cm}^{-1}$. This interpretation is further supported by the changes of the 2D TIRV line shapes with the addition of salt (see the discussion below).

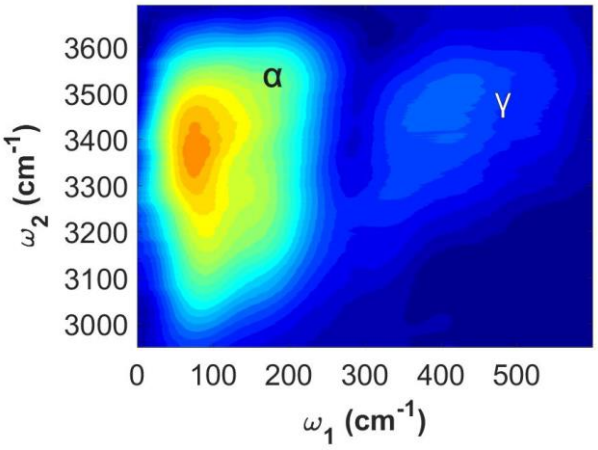

Fig. 5.2 First quadrant of the absolute-value 2D TIRV spectrum of neat water.

In our previous work, we have shown that peak α reflects the coupling between the intramolecular OH-stretch and the intermolecular hydrogen-bond stretch and bending modes [65]. A significantly improved signal-to-noise ratio in the present work also enables also an unambiguous detection of peak γ, which was barely observable in our previous study. This peak is in the frequency range $300\ \mathrm{cm}^{-1} \lesssim \omega_1 \lesssim 600\ \mathrm{cm}^{-1}$, i.e. at the red-wing of the broad libration band of liquid water (Fig. 5.3, [28,37]). Thus, we assign peak γ to the coupling between the water OH-stretch mode and the libration modes. The appearance of the water libration modes as a peak at $\omega_1 \approx 400\ \mathrm{cm}^{-1}$ in the 2D TIRV spectrum is due to the limited bandwidth of the THz pulse (Fig. 3.3) and, thus, an inefficient excitation of the water librations at higher frequencies.

Ions alter the coupling between the OH-stretch and the intermolecular modes, and the 2D TIRV spectra in Fig. 5.4 reflect this change. This figure shows the first quadrant of the absolute-value spectra of KCl, KBr and KI aqueous solutions at 1 M, 2 M, and 4M concentration of salts. All spectra are normalized to the water concentration in the samples (Fig. 5.10 in the Supplementary Information, for non-normalized spectra, see Fig. 5.12 in the Supplementary Information). The spectra of the most dilute 1 M KCl and KBr samples resemble the water spectrum within the uncertainty of our experiment. With the increase of the KCl concentration, the intensities of both peaks, α and γ , increase monotonically (Fig. 5.5 a)), however the change of their line shapes is minor. The signal also increases monotonically for the other two salts KBr and KI, increasing their concentration. For KBr and

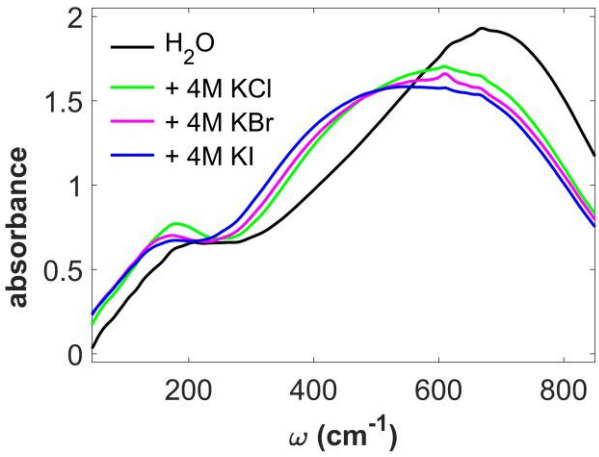

Fig. 5.3 Linear absorption spectrum of neat water (black) and the 4M KCl (green), KBr (magenta) and KI (blue) solutions in the range $50\ \mathrm{cm}^{-1} \lesssim \omega \lesssim 850\ \mathrm{cm}^{-1}$.

KI the signal enhancement is accompanied by a change of the 2D TIRV line shapes. The most pronounced difference of the line shapes is a gradual displacement of peak γ to lower ω_1-frequencies (Fig. 5.5 b)), which can already be seen for the 1 M sample in the case of KI. This shift of the intensity of peak γ causes a shift of the intensity minimum that is produced by destructive interference between the peaks α and γ, from $\omega_1 \approx 290\ \mathrm{cm}^{-1}$ for neat water to $\omega_1 \approx 200\ \mathrm{cm}^{-1}$ for 4 M KI. The shift of peak γ is more prominent for KI than for KBr and KCl, and for the 4 M sample its displacement reaches $\Delta\omega_1 \approx 90\ \mathrm{cm}^{-1}$.

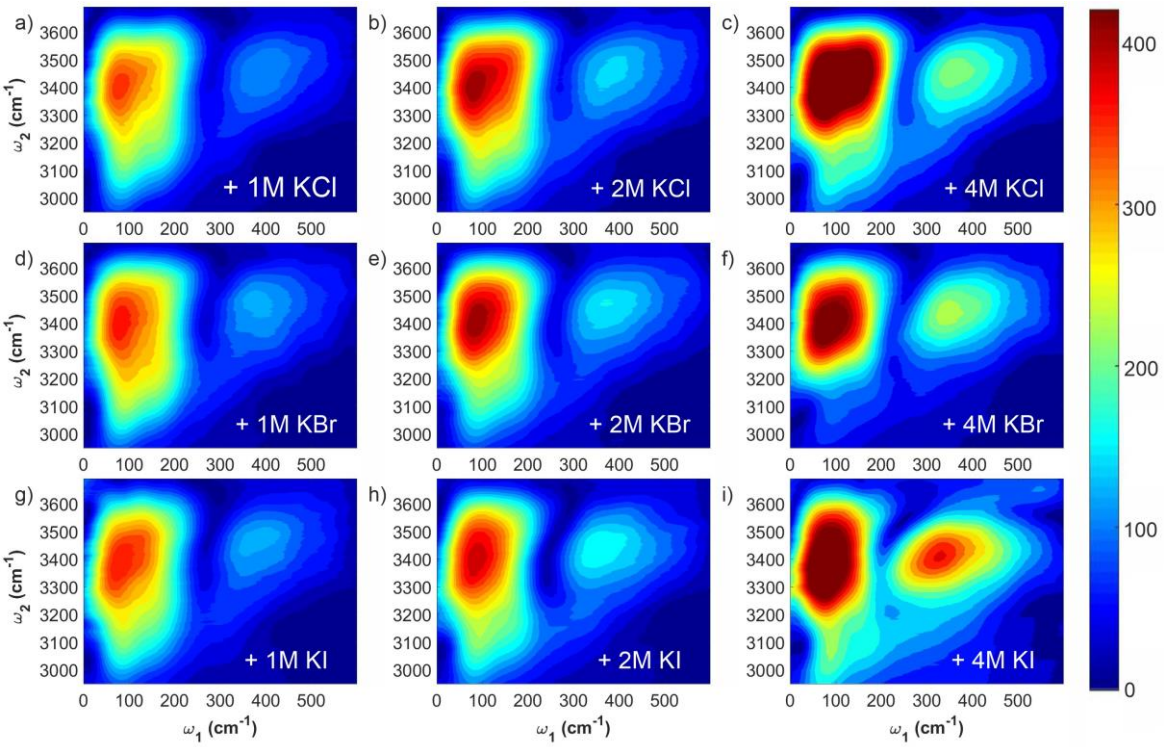

Fig. 5.4 First quadrant of the absolute-value 2D TIRV spectra of the aqueous salt solutions (1M, 2M and 4M concentrations of KCl, KBr and KI, respectively). The spectra are normalized to the water concentration in the corresponding samples.

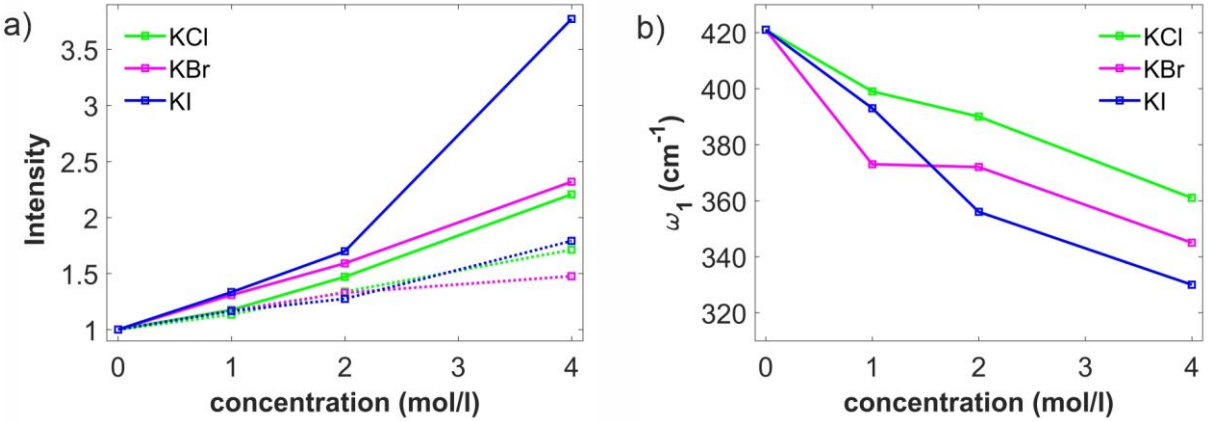

Fig. 5.5 a) Intensity of the 2D TIRV spectra shown in Fig. 5.4 at the maximum of the peaks γ (solid lines) and α (dotted lines). b) Position along the ω_1-axis of the maximum of peak γ.The drastic increase of the 2D TIRV signal intensity for the concentrated halides solutions indicates that the ions significantly enhance the efficiency of the signal generation. This gain in efficiency can be due to the increasing efficiency of the excitation of water vibrations (i.e. increasing transition dipole moments and/or polarizability of those), the increasing vibrational density of states (VDOS) of the water libration modes in the frequency range of our THz pulse as well as increasing coupling strength between the OH-stretch and libation modes. Below we discuss the contributions of these different mechanisms to the change of the 2D TIRV spectra.

5.2.2 Libration of water in the hydration shell of Cl^-, Br^- and I^-

The shift of peak γ along the ω_1-axis in the presence of ions indicates a significant change of the water libration modes that are coupled with the OH-stretch vibration in the hydration shell of ions. Indeed, the linear absorption spectra show a significant change of the water libration band for salt solutions (Fig. 5.3) [29,92,93]. In the presence of ions, the spectral density of the water libration shifts to lower frequencies. For neat water, the maximum of the libration band is at around $680\ \mathrm{cm}^{-1}$. It is generated by e.g. twisting, wagging or rocking motions [28,94–96]. The addition of salts displaces the libration maximum to the red by up to $\sim 100\ \mathrm{cm}^{-1}$ for the 4M solution of KI (Fig. 5.3). This shift of the peak is accompanied by its broadening and the appearance of a shoulder in the range $300\ \mathrm{cm}^{-1} \lesssim \omega \lesssim 500\ \mathrm{cm}^{-1}$. The intensity of this shoulder increases monotonically with the concentration of the ions and depends on the nature of the anion. For a given concentration, the shoulder scales in the sequence Cl^- < Br^- < I^-, i.e. inverse to the charge density of the anion. Whereas for KCl the spectral changes can, in principle, be caused by the formation of the hydration shell around both ions, K^+ and/or Cl^-, the enhancement of the $300 - 500\ \mathrm{cm}^{-1}$ shoulder for KBr and KI can be attributed to the hydration shell of the halide anions Br^- and I^-.

To obtain an insight into how the water libration modes change in the hydration shell of halide anions we perform classical molecular dynamics (MD) simulations for neat water and aqueous salt solutions with concentrations of 1.5 M of KCl, KBr and KI, respectively. The libration modes of a water molecule are determined predominantly by the motion of its hydrogen atoms. Thus, to analyze the librations, we shall utilize their velocity autocorrelation function $\mathrm{VAC}_\mathrm{H}(t) = \langle \vec{v}_\mathrm{H}(0)\vec{v}_\mathrm{H}(t)\rangle$, where $\vec{v}_\mathrm{H}$ is the velocity vector of a hydrogen atom and the angle

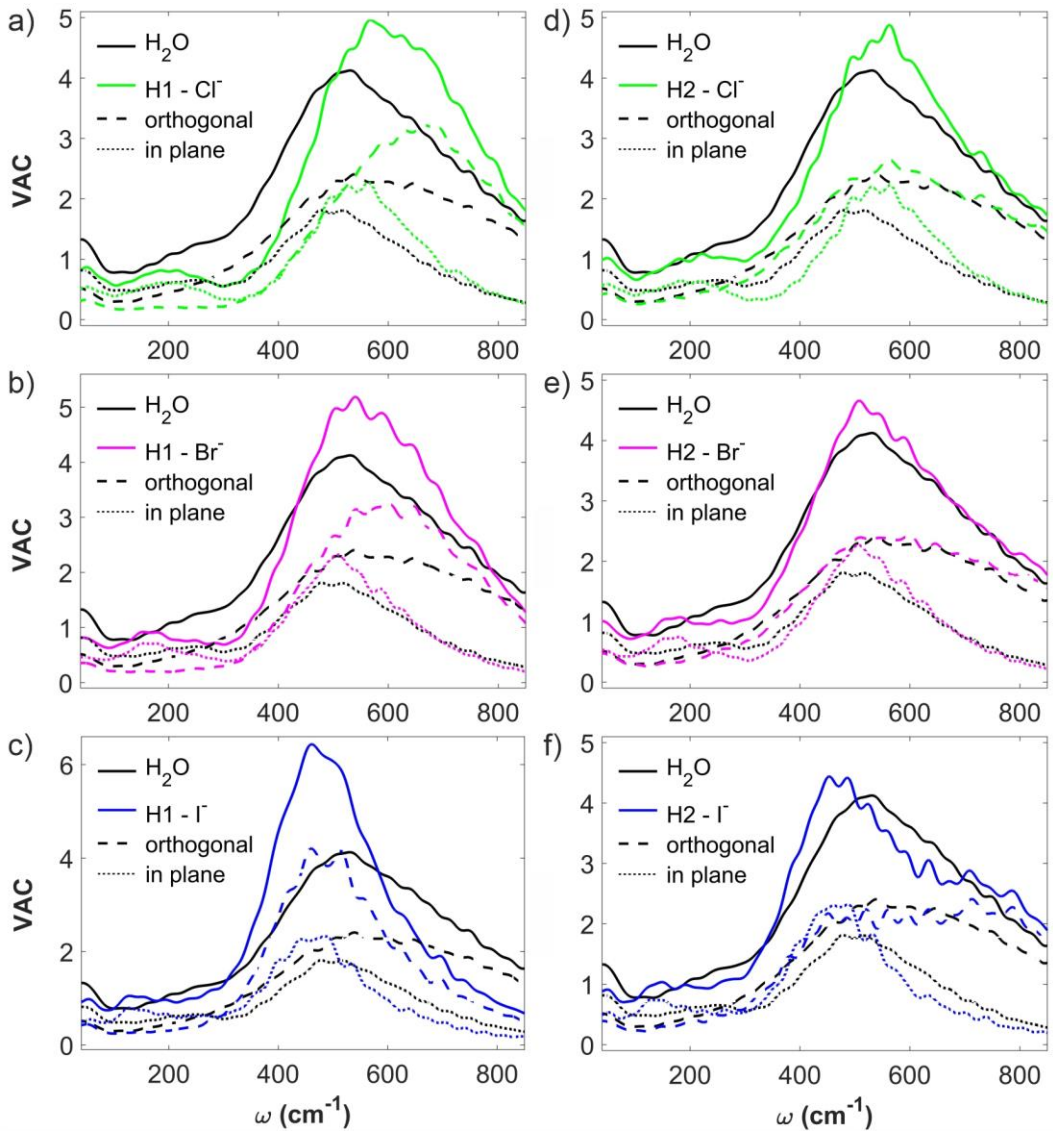

Fig. 5.6 Real part of the spectrum of the velocity autocorrelation function (VAC) for the proton in bulk water (black) and the proton in the first hydration shell of the anions Cl^- (green), Br^- (magenta), and I^- (blue). The panels a)-c) and d)-f) show VAC of H1 and H2, respectively. Dashed lines show the contribution of the motion orthogonal to the plane of the water molecule ($\mathrm{VAC}_{\mathrm{H}}^{\perp}$), dotted lines show the contribution of the motion in plane ($\mathrm{VAC}_{\mathrm{H}}^{\parallel}$).

brackets denote the ensemble averaging. The spectrum of a VAC reflects vibrations that are present in a molecular system [97], and for a given atom, it shows the vibrational modes that this atom contributes to. Figure 5.6 shows the real part of the $\mathrm{VAC}_{\mathrm{H}}$ spectrum of the hydrogen atoms of neat water in the range from 40 to $850\ \mathrm{cm}^{-1}$. Details of the calculation are given in the Supplementary Information. The dominant feature of this spectrum is the broad libration peak in the range from $300\ \mathrm{cm}^{-1}$ to $900\ \mathrm{cm}^{-1}$, with a maximum at $\sim 520\ \mathrm{cm}^{-1}$. In addition to the librations, the spectrum contains much less pronounced hindered translation motions (hydrogen-bond stretch and bending) below $300\ \mathrm{cm}^{-1}$. We compare the $\mathrm{VAC}_{\mathrm{H}}$ spectrum of neat water with that of water hydrogen atoms in the hydration shell of Cl^-, Br^- and I^-. To this end, first we need to determine the hydrogen atoms that form the hydration shell of the anions. Their radial distribution functions ($\mathrm{RDF}_{\mathrm{H}}$) in the proximity of Cl^-, Br^- and I^- are shown

in Fig. 5.7. The H-atoms closest to the ions constitute the first peak located at $0.222\ \mathrm{nm}$, $0.236\ \mathrm{nm}$ and $0.294\ \mathrm{nm}$ for Cl^-, Br^- and I^- respectively. We label these atoms H1 (Fig. 5.8). The spectra of the velocity autocorrelation function of the H1 atoms, $\mathrm{VAC_{H1}}$, are shown in Fig. 5.6. These spectra demonstrate that the maximum of the H1 libration shifts to higher frequencies ($\sim 575\ \mathrm{cm^{-1}}$) for Cl^- and is similar to that of neat water for Br^-. We find the most significant spectral change for I^-. The hydrogen atoms close to I^- librate at lower frequencies ($\sim 480\ \mathrm{cm^{-1}}$) and the spectrum is significantly narrower (located between $300\ \mathrm{cm^{-1}}$ and $700\ \mathrm{cm^{-1}}$), compared to that of neat water, Cl^- and Br^-. At the same time the libration motion of the second proton of the water molecules in the first hydration shell, which we label H2 (Fig. 5.8), changes only moderately (Fig. 5.6).

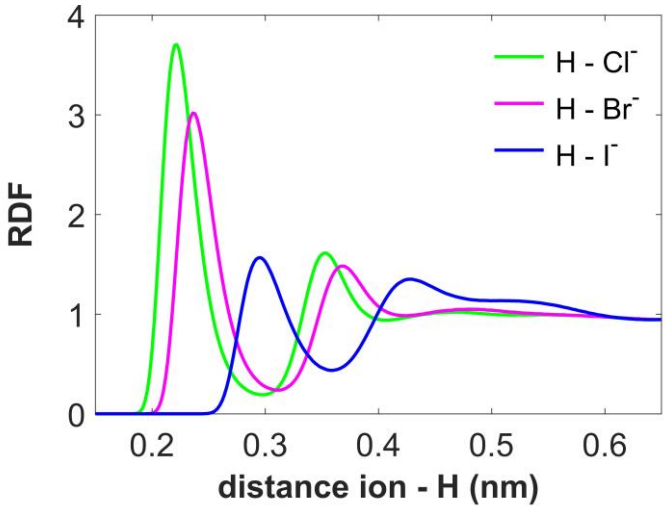

Fig. 5.7 Radial distribution function (RDF) for the proton next to the Cl^- (green), Br^- (magenta) and I^- anion (blue).

We can decompose the water libration into the hydrogen motion in the instantaneous H-O-H plane ($\vec{v}_{\mathrm{H}}^{\parallel}$) and orthogonal to this plane ($\vec{v}_{\mathrm{H}}^{\perp}$) (Fig. 5.8). The former can be associated with rocking and the latter with twisting/ wagging modes of a water molecule [95,96]. The total $\mathrm{VAC_H}(t) = \langle \vec{v}_{\mathrm{H}}^{\parallel}(0)\vec{v}_{\mathrm{H}}^{\parallel}(t)\rangle + \langle \vec{v}_{\mathrm{H}}^{\perp}(0)\vec{v}_{\mathrm{H}}^{\perp}(t)\rangle = \mathrm{VAC_H^{\parallel}}(t) + \mathrm{VAC_H^{\perp}}(t)$ is the sum of both parts (details are given in the Supplementary Information), and, thus, the spectrum of the proton vibration is sum of the spectra of the vibrations in and perpendicular to the instantaneous H-O-H plane. The individual spectra of $\mathrm{VAC_H^{\parallel}}$ and $\mathrm{VAC_H^{\perp}}$ for neat water as well as for the protons H1 and H2 in the hydration shell of Cl^-, Br^- and I^- are shown in Fig. 5.6 with dotted and dashed lines. These spectra demonstrate that the change of the librations between different ions is mainly due to the change of the $\mathrm{VAC_{H1}^{\perp}}$, i.e. the motion of the H1 proton perpendicular to the plane of the water molecule. The spectrum of the $\mathrm{VAC_{H1}^{\perp}}$, which is broadened to the higher frequencies for neat H_2O ($550 - 900\ \mathrm{cm^{-1}}$), contracts and becomes almost identical to the $\mathrm{VAC_{H1}^{\parallel}}$ spectrum for the sample with I^-.

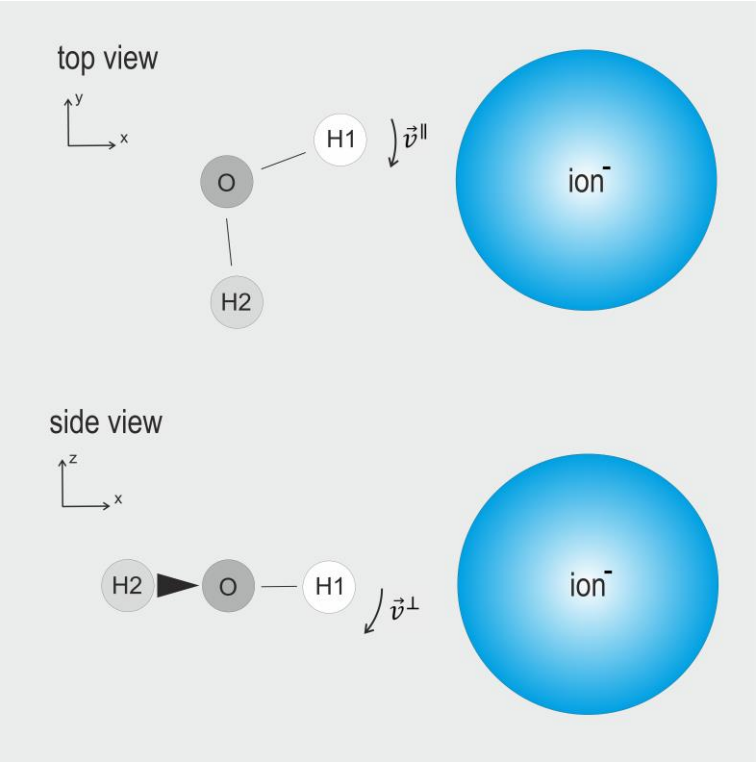

Fig. 5.8 Schematic of a water molecule in the hydration shell of an anion, and of the proton velocity in plane ($\vec{v}^{\parallel}$) and orthogonal to the plane ($\vec{v}^{\perp}$) of the water molecule. The tendency of the water librations to shift to the red in the sequence Cl^-, Br^- and I^- in the MD calculations is consistent with the change of their absorption spectra in Fig. 5.3. Moreover, the libration of the H1 atom in the hydration shell of I^- composes a relatively sharp peak between $350\ \mathrm{cm}^{-1}$ and $600\ \mathrm{cm}^{-1}$, similar to the $300 - 500\ \mathrm{cm}^{-1}$ shoulder in the absorption spectrum. Thus, we attribute this shoulder predominantly to the libration motion of the H1 atom.

5.2.3 Coupling between the water OH-stretch and the libration modes in the hydration shell of halide anions

Now, we can propose connections between the changes in the $\mathrm{VAC}_{\mathrm{H1}}$, the absorption and the 2D TIRV spectra. To this end, we consider the case of 4M KI as the most prominent one. The replacement of the water-water hydrogen bonds by the weaker water-I^- bonds causes the shift of the H1 libration to the red and increases their VDOS in the $350 - 600\ \mathrm{cm}^{-1}$ range by up to 50% (Fig. 5.6). However, this increasing density of states of the H1 atoms can account for an increase of only ~ 1.17 of the absorbance as the latter includes also absorption by bulk water (details of this estimation are given in the Supplementary Information). Instead, we see an increase of ~ 1.5 of the absorbance around $\sim 375\ \mathrm{cm}^{-1}$ (Fig. 5.3). This estimate shows that the relatively small number of the H1 atoms whittles down the increase of their VDOS, even for the highly concentrated 4M solution of KI. Therefore, a part of the increasing absorption can be attributed to an enhanced transition dipole moment of the water libration in the hydration shell of the highly polarizable I^--anion. Ab initio molecular dynamics calculations show that ion solvation causes no significant changes of the water molecule's dipole moment [20,22]. However, partial charges on the position of the hydrogen and oxygen atoms of the water molecules generate a local electrical field with field strength up to

$100\ \mathrm{MV/cm}$, fluctuating at terahertz frequencies [98]. This field acts onto the electrons of the halide anions and polarizes them substantially. Such an additional local polarization can enhance the transition dipole moment of the terahertz vibrational modes of water [20,22]. For this mechanism, one can expect that: among all protons the effect is the most pronounced for the H1 librations ($350 - 600\ \mathrm{cm^{-1}}$), because of their proximity to an ion; the contribution of the ion to the transition dipole scales with the ion polarizability and is the largest for I^-. As a result, we conclude that the new libration mode of H1 with increased infrared activity generates the pronounced shoulder of the libration peak in the absorption spectrum. At the same time, the coupling between the new libration mode of H1 and the OH1-stretch vibration in the hydration shell of I^- (Fig. 5.13 in the Supplementary Information) enhances the 2D TIRV signal around $\omega_1 = 350\ \mathrm{cm^{-1}}$. The latter appears as a red-shift of the peak γ in Fig. 5.4.

The 2D TIRV spectra show a surprisingly high increase of the intensity, given that at best only a quarter of all hydrogen atoms are H1 atoms that are strongly affected by the ions. To assess how much of this signal enhancement can be due to the increased vibrational density of states and the increased transition dipole moments, we need first to consider the mechanism that generates the 2D TIRV signal. In 2D TRIV spectroscopy, either the vibrational excitation by the infrared pulse or the non-resonant electronic excitation by the visible pulse is a two-quantum transition, i.e. it changes simultaneously the quantum numbers of both, the LFM and HFM (Fig. 5.1) [65,69]. The excitation pathway with the two-quantum transition at the interaction with the visible pulse (pathway A in Fig. 5.1) appears in a spectrum at the frequency $\omega_2 = \omega_{\mathrm{HFM}} + \omega_{\mathrm{LFM}}$. If this was the pathway that gives rise to peak γ, its ω_2-frequency would be $\omega_2 \approx 3800\ \mathrm{cm^{-1}}$, given by sum of the OH-stretch and the libration frequency. In contrast, peak γ is located at $\omega_2 \approx 3450\ \mathrm{cm^{-1}}$, which is close to the frequency of the OH-stretch mode. Hence, peak γ is produced via the two-quantum transition occurring at the interaction with the infrared pulse (pathway B in Fig. 5.1). One can draw the same conclusion from reported theoretical calculations [99].

For the excitation pathway B, the signal per water molecule is linearly proportional to the product $\langle n_{\mathrm{libr}} n_{\mathrm{OH}} \mu_{\mathrm{libr}} \mu_{\mathrm{coupl}} \alpha \rangle$, where n_{libr} and n_{OH} are the VDOSs of the librational and the OH-stretch modes per water molecule, respectively. The transition dipole moments μ_{libr} and μ_{coupl} excite the libration (v_{libr}) and the OH-stretch (v_{OH}) motion, α is the polarizability of the molecular system responsible for non-resonant electronic transition, and the angle brackets denote the ensemble average. We note that μ_{coupl} is not the transition dipole moment that gives rise to the linear absorption spectrum of the OH-stretch mode, because, in contrast to the absorbance, the OH-stretch excitation is accompanied by the simultaneous quenching of the libration in pathway B. Instead, it reflects the coupling between the water OH-stretch and the libration motion. For a simple assessment, we approximate $\langle n_{\mathrm{libr}} n_{\mathrm{OH}} \mu_{\mathrm{libr}} \mu_{\mathrm{coupl}} \alpha \rangle \approx \langle n_{\mathrm{libr}} \mu_{\mathrm{libr}} \rangle \langle n_{\mathrm{OH}} \mu_{\mathrm{coupl}} \rangle \langle \alpha \rangle$. The VDOS of the OH-stretch per water molecule does not change with the type and concentration of the ion, thus n_{OH} is constant for all samples. From the absorption spectrum in Fig. 5.3, we can find an upper limit for the gain of $\langle n_{\mathrm{libr}} \mu_{\mathrm{libr}} \rangle$ in the $300 - 500\ \mathrm{cm^{-1}}$ spectral range to be ~ 1.5 for the 4M KI solution. This upper limit assumes that the absorption increases solely due to the increasing density of libration states. For the increase of the average polarizability $\langle \alpha \rangle$ of water in the 4M KI sample we obtain a factor of ~ 1.5, based on previous theoretical and experimental work [100,101]. Thus, the terms

$\langle n_{\mathrm{libr}}\mu_{\mathrm{libr}}\rangle$ and $\langle\alpha\rangle$ together may cause an enhancement of the 2D TRIV signal for the 4M KI sample by a factor of at most ~ 2.3, which is lower than the measured value of 3.8 (Fig. 5.5). We note that the actual increase of peak γ is likely to be even higher because of the destructive interference with the also increasing peak α in the 2D TIRV spectrum (Fig. 5.5).

An additional enhancement of peak γ can stem from the increasing coupling term $\langle\mu_{\mathrm{coupl}}\rangle$ due to the polarization of the ion. Previous calculations by Ito and Tanimura demonstrate that the coupling between the OH-stretch and the libration modes has a predominantly electrical character [99]. This means that it originates from the dependence of the water dipole moment μ on both coordinates, q of the OH-stretch and $Q = r_{\mathrm{OH}} \cdot \theta$ of the libration (Fig. 5.9). Such a coupling is linearly proportional to the second derivative $\vec{\mu}'' = \frac{\partial^2\vec{\mu}(q,Q)}{\partial q \partial Q}$ of the molecular dipole moment $\vec{\mu}(q,Q)$. We evaluate $\vec{\mu}''_{\mathrm{X}}$ using a model of a water molecule next to a polarizable point X (Fig. 5.9), where X = H_2O, Cl^-, Br^-, I^-. This model simulates the hydrogen bonding to another water molecule for neat water and an ion for salt solutions. In this model, the only moving atom is the hydrogen atom H1, with a charge of $0.52e$ and an oxygen-hydrogen distance of 0.96 Å (TIP4P-Ew water model). The distance between the oxygen atom and the ion R_{OX} is taken at the maximum of the radial distribution function produced by the MD simulations (Fig. 5.14 in the Supplementary Information) and equals to 2.76 Å, 3.16 Å, 3.30 Å and 3.88 Å for X = H_2O, Cl^-, Br^- and I^-, respectively. The derivative is calculated at the maximum of the distribution of the angle θ (Fig. 5.9 and Fig. 5.14 in the Supplementary Information). We thus obtain $|\vec{\mu}''_{\mathrm{X}}|$ equals to 0.425 e/Å, 0.485 e/Å, 0.523 e/Å and 0.488 e/Å for a H_2O complex with H_2O, Cl^-, Br^- and I^-, respectively. This model demonstrates that the polarizability of the anion can indeed enhance electrical coupling between the OH-stretch and libration modes, although this gain is moderate.

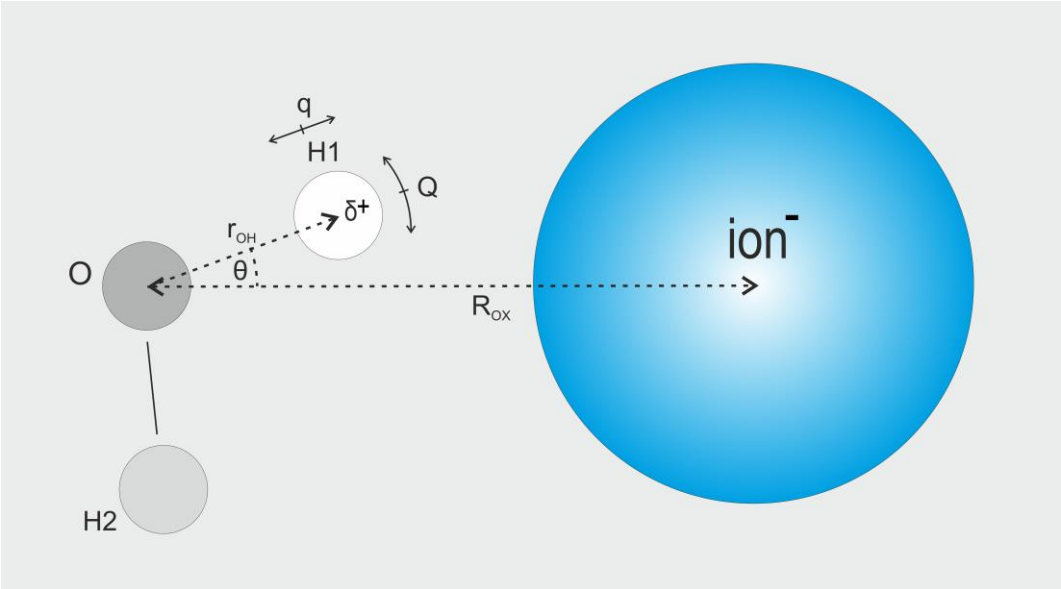

Fig. 5.9 Schematic of the polarization model.

We note a discrepancy between the experimental results and the behavior of the calculated $\mathrm{VAC_H}$ for the KCl and KBr samples. In the case of KCl, the libration band shifts to the red in the absorption spectrum, whereas the VAC of the H1 atom, $\mathrm{VAC_{H1}}$, shifts to the blue. For KBr the red-shift of the libration modes is observable in both, the linear and the 2D TIRV spectra, but is not captured by the change of $\mathrm{VAC_{H1}}$. These discrepancies can be due to the non-polarizable force field employed in this work. Although the parameters of the ions utilized in the MD simulations are optimized for the TIP4P-Ew water model and, thus, implicitly include the influence of the water's and ion's polarizability on the intermolecular forces, a more accurate description requires a polarizable force field. Also, a quantitative comparison between the measured spectra and the computations is impossible without taking the polarization explicitly into account. We anticipate that future works utilizing polarizable / ab-initio level of theory will further advance the understanding of water librations.

In summary, the marked increase of the 2D TIRV signal most likely results from a combination of different mechanisms. We found that besides the increased linear transition dipoles, an increased coupling can explain the changes in the 2D TIRV spectra of the aqueous salt solutions. This coupling is transmitted by the polarizability of the ion next to the water molecule. A complete description most likely needs to take into account additional effects as charge transfer [102]. In particular, the coupling near the polarizable ion is enhanced. Our 2D TIRV measurements have an enhanced sensitivity for the water in the hydration shell of the ion.

5.3 METHODS

5.3.1 Linear absorption spectroscopy

The linear absorption spectra are measured using a commercial Bruker Vertex 70, extended to measure absorption spectra in the range from 30 to $6000\ \mathrm{cm^{-1}}$. To measure absorption spectra in the far-infrared (terahertz) frequency range, we use two different homemade sample cells. One of them is a flow sample cell equipped with silicon ($0.5\ \mathrm{mm}$ thick) windows. Another sample cell is equipped with diamond ($2\ \mathrm{mm}$ thick) windows and does not allow to flow the sample. In both cases, the windows are separated by a $\sim 10\ \mu\mathrm{m}$ thick Teflon spacer. The invariant path length of the flow sample cell was verified by multiple measurements of the neat water spectrum. The results obtained by using the silicon and diamond sample cells are identical within the accuracy of our experiment. To measure the absorption spectra in the mid-infrared range, we use a sample cell composed of two CaF_2 windows ($2\ \mathrm{mm}$ thick) without any spacer. This configuration causes varying path length when we change the samples. To correct for the varying path length in the mid-infrared spectral range, we use the intensity of the H-O-H bending mode obtained for different samples using the flow silicon sample cell and scale accordingly the spectra measured with the CaF_2 sample cell.

5.3.2 2D TIRV spectroscopy

Our 2D TIRV spectroscopy setup is described in detail in chapter 3 and 4. In brief, we split the output of an amplified Ti:Sapphire laser ($5\ \mathrm{mJ/pulse}$, $1\ \mathrm{kHz}$ repetition rate, about $60\ \mathrm{nm}$ FWHM) into three beams (each $\sim 1\ \mathrm{mJ/pulse}$), from which we generate the broadband mid-IR (centered at $\sim 3400\ \mathrm{cm^{-1}}$, $300\ \mathrm{cm^{-1}}$ FWHM, $\sim 1\ \mu\mathrm{J/pulse}$), VIS (centered at $800\ \mathrm{nm}$,

$1\ \mathrm{nm}$ FWHM, $\sim 7\ \mu\mathrm{J/pulse}$) and THz beam (Fig. 3.3), respectively. All beams are polarized horizontally, interact with the sample and generate the signal field. We detect the horizontally polarized signal field using a spectrometer and a CCD camera.

Here, we do not use a displaced Sagnac interferometer as in chapter 4 but produce the local oscillator (LO) by sum-frequency mixing of the IR and VIS pulses at the surface of a gold mirror coated with a protective Y_2O_3 layer. The path length of $183\ \mathrm{cm}$ from the LO generation to the sample position generates a time delay of $\approx 100\ \mathrm{fs}$ between the 2D TIRV signal and LO due to the dispersion between the IR and LO beam in nitrogen gas. At the sample position, this leads to an offset in time by $\sim 100\ \mathrm{fs}$. For the broad water spectrum, this time delay is enough to apply the quadrant separation procedure of chapter 4.

5.3.3 Molecular dynamics calculations

We perform classical molecular dynamics (MD) simulations using the GROMACS 2020.1 software. The calculations are implemented for a molecular system in a 3 nm cubic box. The neat water is composed of 909 H_2O molecules. For the salt solutions, we use 861 H_2O molecules, 24 K^+ cations and 24 Cl^-, Br^- or I^- anions. These compositions correspond to a 1.5 M concentration of KCl, KBr and KI, respectively. We use the force field parameters of Joung and Cheatham [103] for the ions and the TIP4P-Ew model for water. We employ a particle-mesh Ewald (PME) summation with a grid spacing of $0.12\ \mathrm{nm}$ and a fourth-order interpolation, Lorentz-Berthelot combining rules for the Lennard-Jones potential and a $0.9\ \mathrm{nm}$ cutoff for electrostatic and van der Waals forces. Each system is equilibrated first for $1\ \mathrm{ns}$ for a NVT ensemble at $298\ \mathrm{K}$ using a Nosé-Hoover thermostat with a time constant of $1\ \mathrm{ps}$, and then for $1\ \mathrm{ns}$ for a NPT ensemble at 298 K and 1 bar using a Nosé-Hoover thermostat and a Parrinello-Rahman barostat with time constants of $1\ \mathrm{ps}$ and $3\ \mathrm{ps}$, respectively. This was followed by a $1\ \mathrm{ns}$ NPT production run using a Nosé-Hoover thermostat and a Parrinello-Rahman barostat with time constants of $5\ \mathrm{ps}$ and $12\ \mathrm{ps}$, respectively. All equilibration and production are performed with a time step of $0.5\ \mathrm{fs}$, and for the analysis, the coordinates and velocities are saved every $4\ \mathrm{fs}$ in a production run.

5.4 SUPPLEMENTARY INFORMATION

5.4.1 Water concentration in the aqueous salt solutions

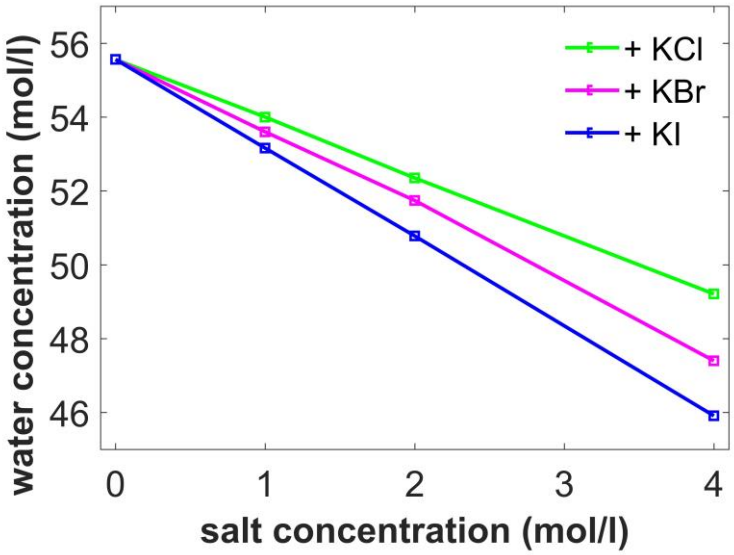

Fig. 5.10 Water concentration in the aqueous salt solutions.

5.4.2 Data processing

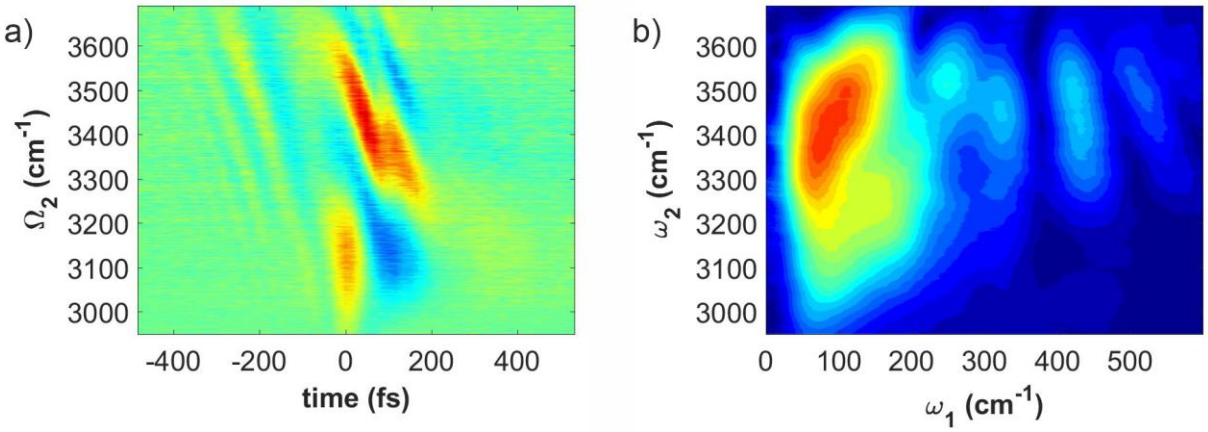

Fig. 5.11 Time-domain 2D TIRV data for neat water. b) First quadrant of the absolute-value 2D TIRV spectrum of neat water. The spectrum is obtained by Fourier transform of the time-domain data in panel "a" in the time interval $t_{start} = -500$ fs to $t_{end} = +500$ fs.

The 2D TIRV spectrum of water obtained by a Fourier transform of the time-domain data in the full time interval (Fig. 5.11 a)), contains an interference pattern in the first quadrant (Fig. 5.11b)). This interference is located at the position of peak γ and is due to the relatively small time delay (~ 150 fs) between the signal and LO. Because of this small time delay both peaks γ (from the first quadrant) and δ (from the second quadrant) appear in the first quadrant of the spectrum and interfere. We eliminate the contribution of peak δ by restricting

the time interval in the time-domain data to ($t_{\text{start}} = -50$ fs, $t_{\text{end}} = +450\ fs$) before the Fourier transformation in step 3 of the quadrant separation procedure (chapter 4). To this end, we use a window function $W(t)$ given by a combination of the cumulative distribution function of the Normal distribution

$$W(t) = \left(\frac{1}{\sigma\sqrt{2\pi}}\int_{-\infty}^{t} \exp(-\frac{(x - t_{\text{start}})}{2\sigma^2}\,dx\right) \cdot \left(1 - \frac{1}{\sigma\sqrt{2\pi}}\int_{-\infty}^{t} \exp(-\frac{(x - t_{\text{end}})}{2\sigma^2}\,dx\right) \tag{5.1}$$

with $\sigma = 50$ fs. Thus the obtained first quadrant of the 2D TIRV spectrum demonstrates an excellent agreement with the spectrum measured using the displaced Sagnac interferometer (chapter 4). This comparison confirms the elimination of peak δ from the spectrum. We note that peak δ, which can be obtained by restricting the time interval in the time-domain data to ($t_{\text{start}} = -450$ fs, $t_{\text{end}} = +50\ fs$), changes similar to peak γ with addition of salts (the data are not shown).

5.4.3 2D TIRV spectra of aqueous salt solutions

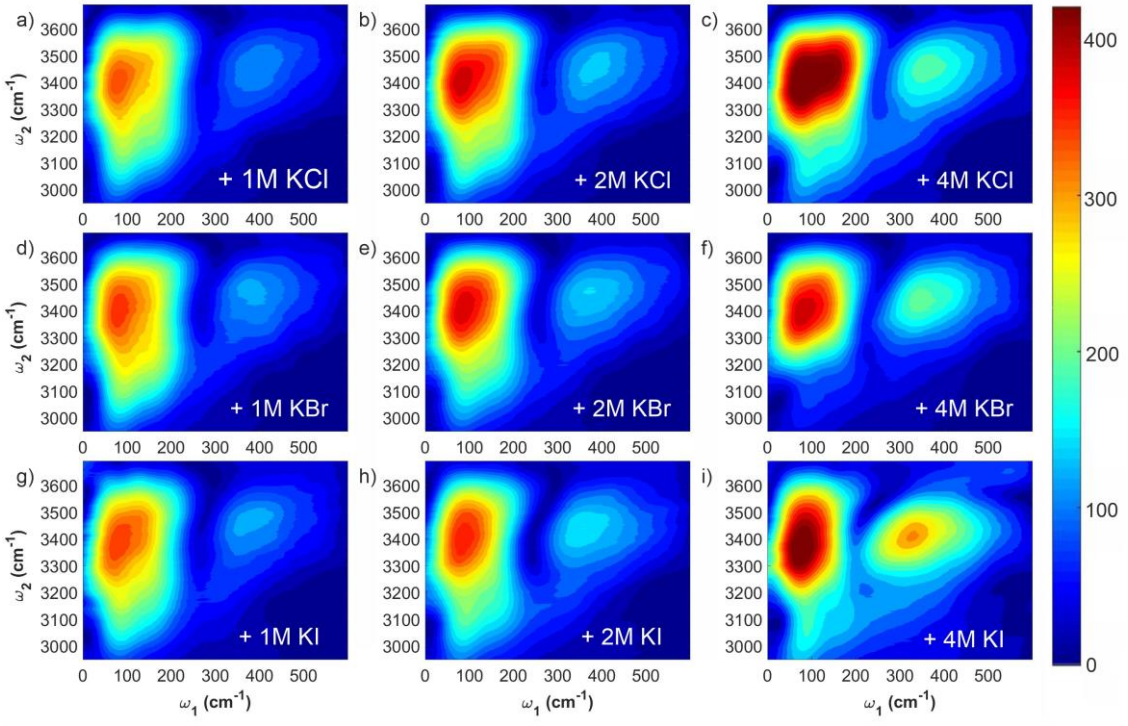

Fig. 5.12 First quadrants of the 2D TIRV spectra of the aqueous salt solutions (1M, 2M and 4M concentrations of KCl, KBr and KI, respectively) without normalizing them to water concentration in the corresponding samples.

5.4.4 Linear absorption spectrum in the OH-stretch frequency range

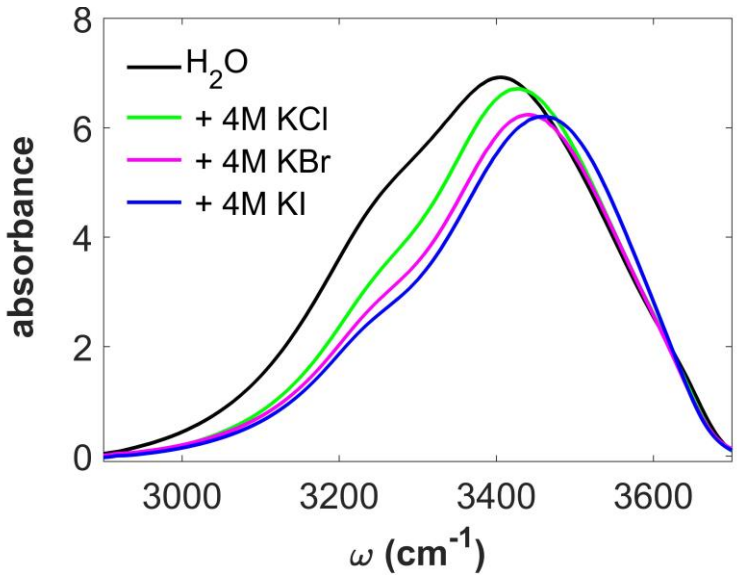

Fig. 5.13 Linear absorption spectrum of neat water (black) and the 4M KCl (green), KBr (magenta) and KI (blue) solutions in the OH-stretch frequency range ($2900\ \mathrm{cm}^{-1} \lesssim \omega \lesssim 3700\ \mathrm{cm}^{-1}$).
The spectra are normalized to water concentration in the corresponding samples.

5.4.5 Configuration of the hydration shell of the anions

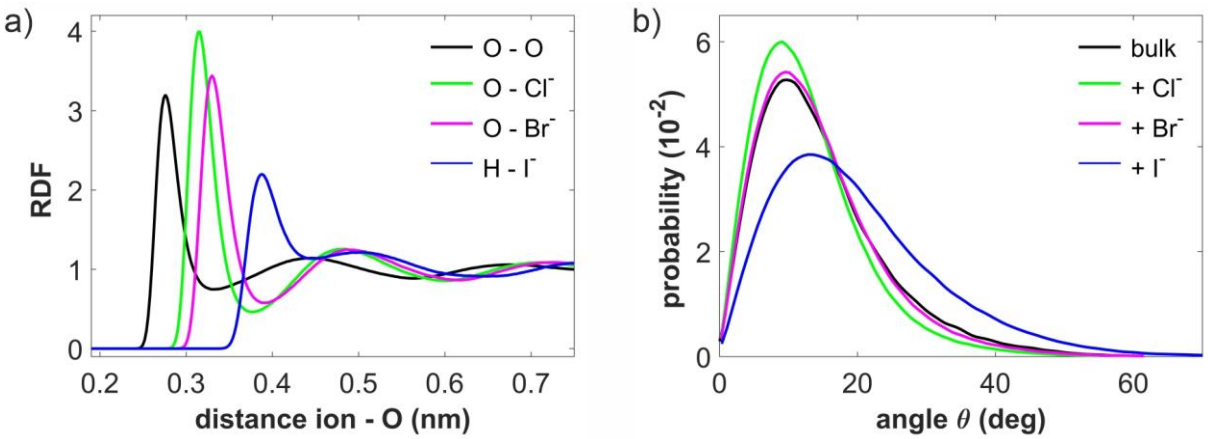

Fig. 5.14 a) Radial distribution function (RDF) for the oxygen atom next to the Cl^- (green), Br^- (magenta) and I^- anion (blue). b) Distribution for the angle θ (Fig. 5.9) in bulk water (black) and in the presence of the Cl^- (green), Br^- (magenta) and I^- anion (blue).

5.4.6 The velocity autocorrelation function of the hydrogen atom

The velocity autocorrelation function $\mathrm{VAC_H}(t) = \langle v_\mathrm{H}(0) v_\mathrm{H}(t) \rangle$ is calculated for a time period of 1 ps and is normalized to $\mathrm{VAC_H}(t = 0) = 1$ for neat water and the 1.5 M samples of KCl, KBr and KI. Figure 5.15 shows the $\mathrm{VAC_H}(t)$ for neat water, which demonstrates that the autocorrelation function decays to almost 0 at $t = 1$ ps. Thus, this time interval is sufficient to sample the libration of the water molecule (the same conclusion has been reached for the salt samples, which are not shown here). On the other hand, the period of 1 ps does not exceed the reorganization time of the hydrogen bonds, and therefor during this period most of the H1 and H2 hydrogen atoms remain in the hydration shell of Cl^-, Br^- and I^-.

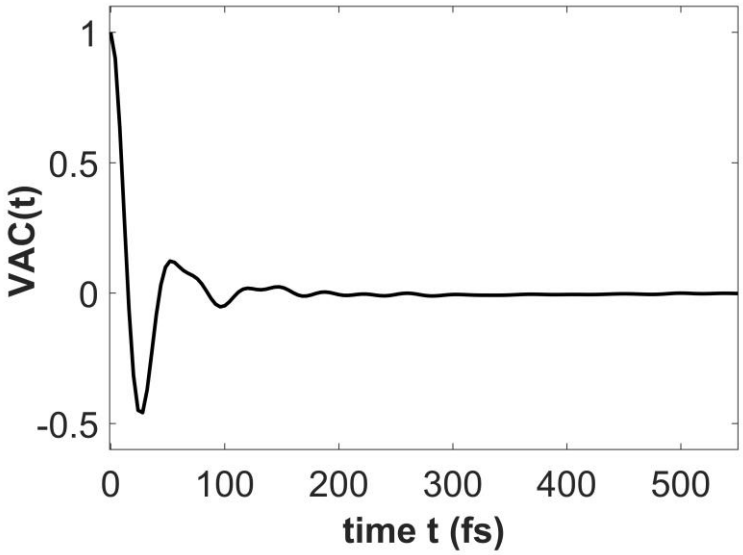

Fig. 5.15 Velocity autocorrelation function VAC(t) for the proton in neat water.

The spectrum $\mathrm{VAC_H}(\omega)$ is calculated by a fast Fourier transform (FFT) of the time-domain function $\mathrm{VAC_H}(t)$ with $\mathrm{VAC_H}(0) = 0.5$ to take into account the discreteness of the FFT.

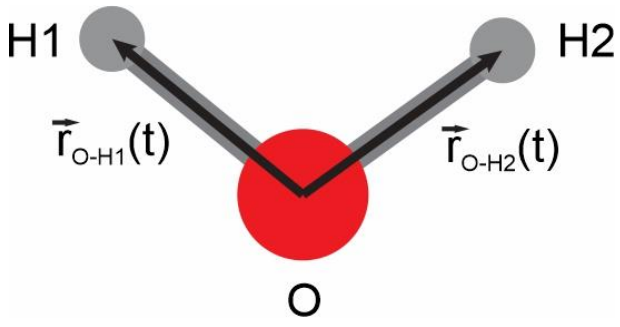

Fig. 5.16 Schematic of a water molecule with the vectors $\vec{r}_{\mathrm{O\text{-}H1}}(t)$ and $\vec{r}_{\mathrm{O\text{-}H2}}(t)$.

To calculate $v_{\mathrm{H}}^{\parallel}(0)$, $v_{\mathrm{H}}^{\parallel}(t)$, $v_{\mathrm{H}}^{\perp}(0)$ and $v_{\mathrm{H}}^{\perp}(t)$ we determine the unit vector orthogonal to the plane of the water molecule

$$\vec{n}(t) = \frac{\vec{r}_{\text{O-H1}}(t) \times \vec{r}_{\text{O-H2}}(t)}{|\vec{r}_{\text{O-H1}}(t) \times \vec{r}_{\text{O-H2}}(t)|}. \tag{5.2}$$

Here, $\vec{r}_{\text{O-H1}}(t)$ and $\vec{r}_{\text{O-H2}}(t)$ are time-dependent vectors between the oxygen atom O and the hydrogen atoms H1 and H2, respectively (Fig. 5.16).

Thus, the velocities are given by

$$\vec{v}_{\mathrm{H}}^{\perp}(0) = \left(\vec{v}_{\mathrm{H}}(0) \cdot \vec{n}(0)\right) \cdot \vec{n}(0), \tag{5.3}$$

$$\vec{v}_{\mathrm{H}}^{\perp}(t) = \left(\vec{v}_{\mathrm{H}}(t) \cdot \vec{n}(0)\right) \cdot \vec{n}(0), \tag{5.4}$$

$$\vec{v}_{\mathrm{H}}^{\perp}(t) = \left(\vec{v}_{\mathrm{H}}(t) \cdot \vec{n}(0)\right) \cdot \vec{n}(0), \tag{5.5}$$

$$\vec{v}_{\mathrm{H}}^{\parallel}(t) = \vec{v}_{\mathrm{H}}(t) - \vec{v}_{\mathrm{H}}^{\perp}(t). \tag{5.6}$$

5.4.7 The change of the hydrogen VDOS in the presence of I^-

The water concentration in neat water at standard conditions is 55.5 M, thus the concentration of the water's hydrogen atoms is 110 M. This concentration decreases to 92 M for the sample with 4 M of KI (Fig. 5.10). We assume that there are 7.6 water molecules in the hydration shell of I^- on average (obtained from the MD calculations). Thus, the concentration of H1 atoms in the 4 M KI sample is $7.6 \cdot 4\ \mathrm{M} = 30.4\ \mathrm{M}$ and the concentration of all other hydrogen atoms is $92\ \mathrm{M} - 30.4\ \mathrm{M} = 61.6\ \mathrm{M}$. These H1 atoms have a 1.5 times higher vibrational density of states in the $350 - 600\ \mathrm{cm}^{-1}$ frequency range, and for all other hydrogens we assume an invariant vibrational density of states (Fig. 5.6). Therefore, the average increase of the vibrational density of states per hydrogen atom is given by the ratio $(1.5 \cdot 30.4\ \mathrm{M} + 61.6\ \mathrm{M})/92\ \mathrm{M} \approx 1.17$.

6 INHOMOGENEITY OF THE HYDROGEN-BOND MODES IN LIQUID WATER AND HALIDE SALTS SOLUTIONS

Contributions to this chapter: M. Grechko and M. Bonn conceived the project. L. Vietze and M.G. designed the details and L.V. performed the 2D TIRV and FTIR measurements. L. V. and M.G. analyzed the results. All authors discussed the results and contributed to the manuscript.

Paper manuscript is in preparation.

6.1 INTRODUCTION

Water and aqueous solutions are ubiquitous in our daily-life. They play a crucial role in biology and chemistry, where water most often acts as solvent for various substances and provides the environment for chemical reactions [1,2]. The unique molecular properties of water that influence reaction pathways are not yet fully understood, but frequently related to the presence of hydrogen bonds that connect the water molecules with each other [3,4,6]. Hydrogen bonding leads to the formation of a tetrahedral water network, which is highly dynamic. At room temperature (thermal energy $\sim 200\ \mathrm{cm}^{-1}$), mainly the so-called low-frequency hydrogen-bond modes are thermally excited and thus responsible for the dynamics of the network. They result from the translational degrees of freedom and are classified as the so-called hydrogen-bond bending ($\sim 60\ \mathrm{cm}^{-1}$) and stretching ($\sim 180\ \mathrm{cm}^{-1}$) modes [29,34,35]. As the water molecules and thus the hydrogen bonds are involved in the collective water network, the hydrogen bonds and their modes cannot be considered independent of each other. The strength of one hydrogen bond is influenced by the number and geometry of the other hydrogen bonds that a given water molecule forms [10,11]. Furthermore, the surrounding hydrogen bonds influence the intramolecular dynamics of the water molecules. For example, the frequency of the OH-stretch mode correlates with the strength of the hydrogen bond [9]. Investigations on these couplings between the modes are not only of fundamental interest, but also enable to learn more about energy dissipation pathways that are crucial for reaction pathways in aqueous solutions.

In this work, we employ 2D Terahertz-InfraRed-Visible (2D TIRV) spectroscopy to study the coupling and correlations of the intermolecular hydrogen-bond modes and the intramolecular OH-stretch mode. To further see the impact of an altered environment, respectively, a different configuration of hydrogen bonds, we investigate the influence of halide anions on this coupling. Ions solved in water alter the structure of the water network as the water molecules form a hydration shell around the ions. This leads to a disruption of the water network and changes in its structure and dynamics [8,13]. The halide anions Cl^-, Br^- and I^- for example weaken the hydrogen bonds, which can be seen indirectly by a red shift of the OH-stretch mode's center frequency [33]. A slowdown of the hydration shell dynamics of these anions was found with pump-probe spectroscopy [17], while a more fragile hydration shell was observed with MD simulations [18]. The direct observation of the hydrogen-bond modes is possible in the far-infrared, respectively THz range ($\sim 50 - 200\ \mathrm{cm}^{-1}$). The hydrogen-bond stretching mode shows up as a shoulder at $\sim 180\ \mathrm{cm}^{-1}$ of the librational peak (centered at $\sim 700\ \mathrm{cm}^{-1}$) that dominates the absorption spectrum in this range [29] (Fig. 6.1). Spectral

changes upon the addition of salt are mainly caused by rattling modes of the ions [16]. In such measurements, it is challenging to identify spectral changes due to altered dynamics of the water network. The hydrogen-bond bending mode at $\sim 60\ \mathrm{cm}^{-1}$ is not so pronounced in the absorption spectrum but can be more clearly distinguished in Raman spectra [34–37].

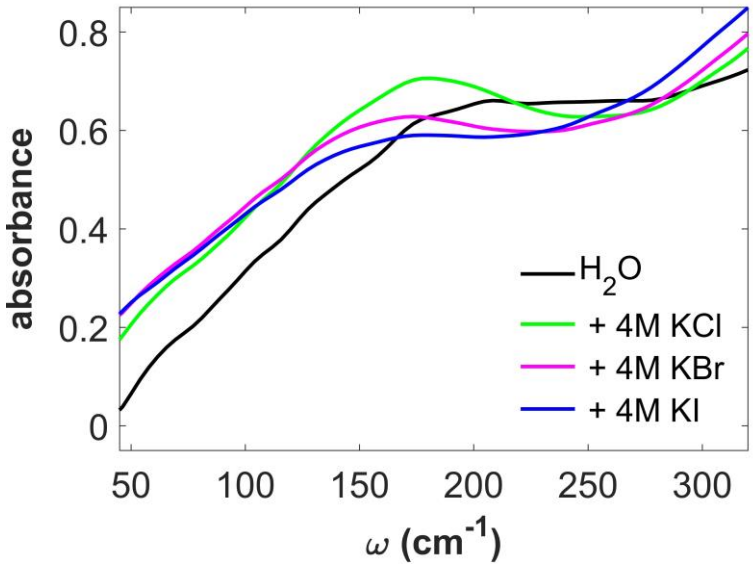

Fig. 6.1 Linear absorption spectra of water and 4 M aqueous salt solutions in the hydrogen-bond mode frequency range.

To disentangle the congested spectra in the spectral range of the low-frequency modes (LFMs), where the hydrogen-bond modes are located, multidimensional spectroscopy can help by adding a second dimension. This also enables to reveal correlations with the same or other modes and thus to investigate the (in-)homogeneity of the hydrogen-bond modes. For hydrogen-bond modes such investigations were performed with 2D Raman-terahertz spectroscopy, where the change of the inhomogeneity with the addition of cations was analyzed [60]. Hamm et al. observed an induced inhomogeneity for this mode by the cations. The magnitude of the induced inhomogeneity depends on the cation species and its propensity to structure the water.

So far, no studies were performed on the coupling and possible correlations of the hydrogen-bond modes with other modes, like the intramolecular OH-stretch mode, to learn more about their coupling. Multidimensional spectroscopy techniques like 2D TIRV that can access both modes simultaneously are an appropriate tool for this. A direct measurement of this coupling in neat water was performed in [65]. Here, studying the changes with the addition of halide anions allows us to see how these anions change the dynamics of the hydrogen-bond network and if they contribute to the inhomogeneity of the network.

To measure the 2D TIRV signal, we need to measure a signal that is enhanced by both modes, the LFM as well as the HFM. To this end, we induce a four-wave-mixing process of a THz, mid-IR, and visible beam. The frequency of the abscissa Ω_1 in the obtained two-dimensional spectrum equals the frequency of the LFM mode ($\Omega_2 = \omega_{\mathrm{LFM}}$), while the ordinate Ω_2

monitors the coherence after the second interaction and thus represents the HFM. A more detailed description is given elsewhere [65,69].

6.2 RESULTS AND DISCUSSION

Figure 6.2 shows the second quadrant of an absolute-value 2D TIRV spectrum of neat water in the frequency range of hydrogen-bond stretch and bending modes. The peak in this spectrum, which we labeled β in chapter 4, has a maximum intensity at $(\omega_1 = -85\ \mathrm{cm}^{-1}, \omega_2 = 3150\ \mathrm{cm}^{-1})$. The ω_1- frequency of this peak is significantly lower than the $\sim 180\ \mathrm{cm}^{-1}$ frequency of the hydrogen-bond stretch vibration in neat liquid water at room temperature [29]. The apparent position of the peak along the ω_1- axis is significantly

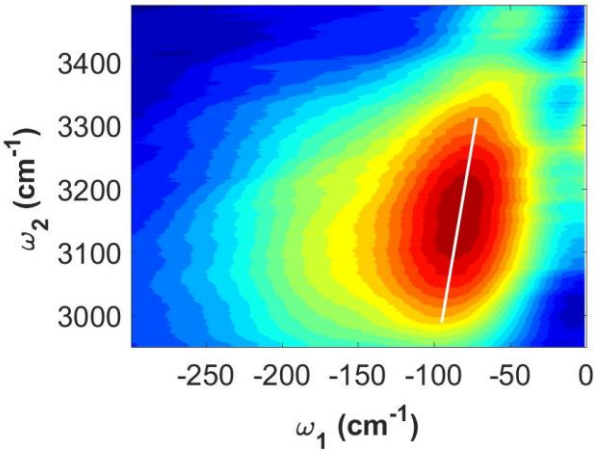

Fig. 6.2 The second quadrant of absolute-value 2D TIRV spectrum of neat water (H_2O). The white line shows the center line of the peak.

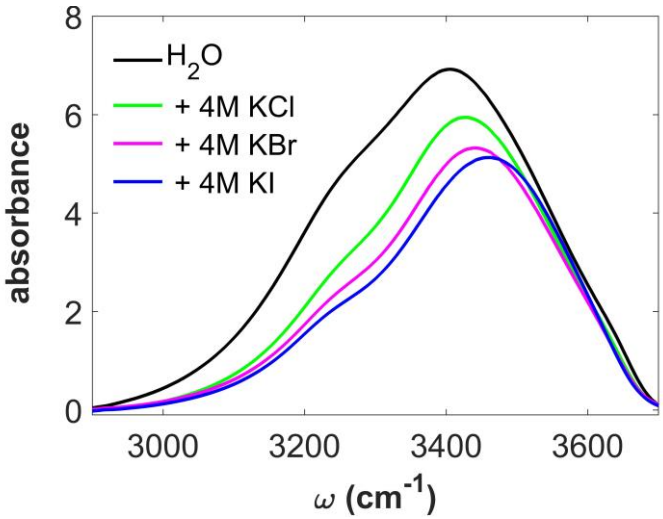

Fig. 6.3 Linear absorption spectrum of the OH-stretch mode for water and 4 M aqueous salt solutions.

influenced by the spectrum of the THz pulse (Fig. 3.3) employed in the experiment. Due to its maximum intensity around $100\ \mathrm{cm}^{-1}$, our THz pulse excites vibrations in this frequency range more efficiently and, thus, produces an enhanced 2D TIRV signal. Because of this and the fact that peak β is detectable up to $\omega_1 = 250\ \mathrm{cm}^{-1}$, we assign this peak to the coupling between the OH-stretch vibration and both the hydrogen-bond stretch and bending modes. The ω_2-frequency of the peak is shifted significantly to the red compared to the OH-stretch maximum in the absorption spectrum (Fig. 6.3). Taking into account that the maximum intensity of the IR pulse employed in the 2D TRIV measurements favors a generation of the signal at $\omega_2 \approx 3500\ \mathrm{cm}^{-1}$ (Fig. 6.4), we conclude that peak β reflects the enhanced LFM-HFM coupling for the red wing of the OH-stretch modes with intra- and inter-molecular delocalization as also concluded previously [65] (Fig. 6.3). This peak is isolated from the signal produced by the water libration modes, and therefore it is a convenient probe to study the characteristics of the hydrogen-bond vibrations of neat water and aqueous salt solutions.

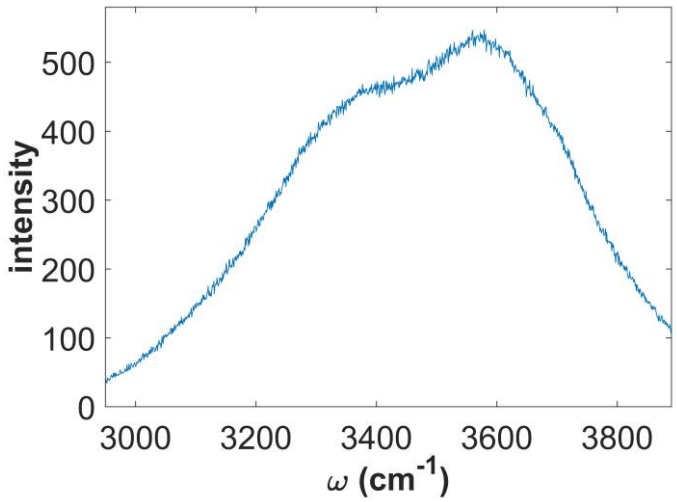

Fig. 6.4 Intensity spectrum of the IR pulse. The spectrum is derived from the measured LO spectrum by subtracting the frequency of the VIS pulse.

Figure 6.5 shows peak β for the aqueous solutions of the three different salts, KCl, KBr and KI, at 1 M, 2 M and 4 M concentrations. One can notice a slight change in the tilt of this peak upon increasing the salt concentration. This change is most apparent for the most intense part of the 4 M KI peak. A well-established method to quantify a peak lineshape, in particular its tilt, is by using the center line slope (CLS). It is often employed in two-dimensional infrared (2D IR) spectroscopy for diagonal peaks to characterize the microscopic inhomogeneity of a system [104]. For a very inhomogeneous system, the diagonal 2D IR peak is elongated along the diagonal and the CLS value is close to 1, indicating a strong correlation of the excitation and probe frequencies of a given vibration. With the decrease of the inhomogeneity the CLS decreases to zero due to the loss of correlation between the excitation and probe frequencies. We apply the CLS concept to the 2D TIRV spectra to quantify the correlations and the inhomogeneity there. However, the implementation and interpretation of this approach in

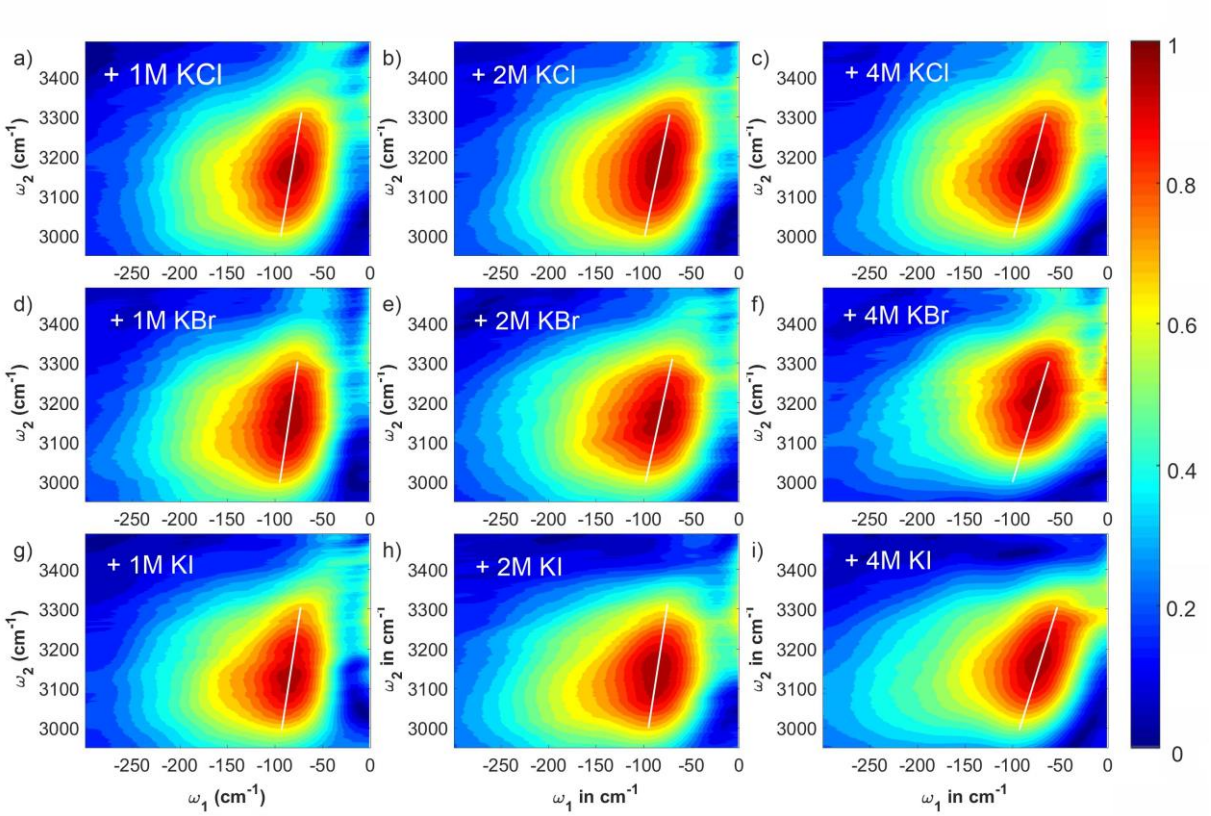

Fig. 6.5 Second quadrant of absolute-value 2D TIRV spectra of the aqueous solutions of KCl, KBr and KI. The solutions contain 1 M, 2 M and 4 M concentrations of the salts. The white line shows the center line of a corresponding peak β.

2D TIRV spectroscopy varies from the one in 2D IR spectroscopy. In 2D TIRV spectroscopy, we measure off-diagonal cross peaks, which result from the coupling of two different modes. Thus, in 2D TIRV spectroscopy, the CLS reveals the correlation between the LFM and HFM. Such a correlation provides an alternative opportunity to investigate the inhomogeneity of a molecular system. We note that the application of the CLS analysis developed in 2D IR spectroscopy is not straightforward in 2D TIRV spectroscopy because of a significantly different excitation scheme of the latter. A detailed consideration requires the development of a rigorous theory of 2D TIRV line shapes, which is a subject for future work. However, in this study we demonstrate that such an approach can indeed provide semi-quantitative insights into the system's inhomogeneity.

We derive the center line of peak γ by taking spectrum profiles at different ω_2-frequencies. We determine the ω_1-frequencies of the maxima in these profiles, and then the (ω_1, ω_2)-pairs determine the center line. The resulting center lines are plotted on top of the 2D TIRV spectra in Fig. 6.2 and Fig. 6.5. We define the CLS as inverse of the slope of the center line, similar to its definition in 2D IR spectroscopy [104]. The obtained values of the CLS of peak β for neat water and the different concentrations of the anions Cl^-, Br^- and I^- are shown in Fig. 6.6 b). We assume that the uncertainty of the values is given by the variations of the CLS for water and the 1M solutions, where no significant spectral changes are observed. Thus, the CLS error bar is about $\pm 15\%$. For all salts, the slope increases from about 0.07 for neat water to about 0.12 for the 4 M samples. Thus, the correlation between the hydrogen-bond and OH-

stretch modes increases with increasing salt concentration. Within the uncertainty of our measurements, we cannot find significant differences for the different ion species. However, the spectral changes that cause the increase of the CLS vary for each anion. Figure 6.6 a) shows the center lines for water and the 4 M solutions plotted together. The change of the CLSs for the Cl^- and Br^- samples is caused by an opposite shift along the ω_1-axis at the low and high ω_2-frequency, respectively. In contrast, the CLS change of the I^--solution is predominantly produced by a shift to the lower ω_1-frequency at the high ω_2-frequency wing of the spectrum.

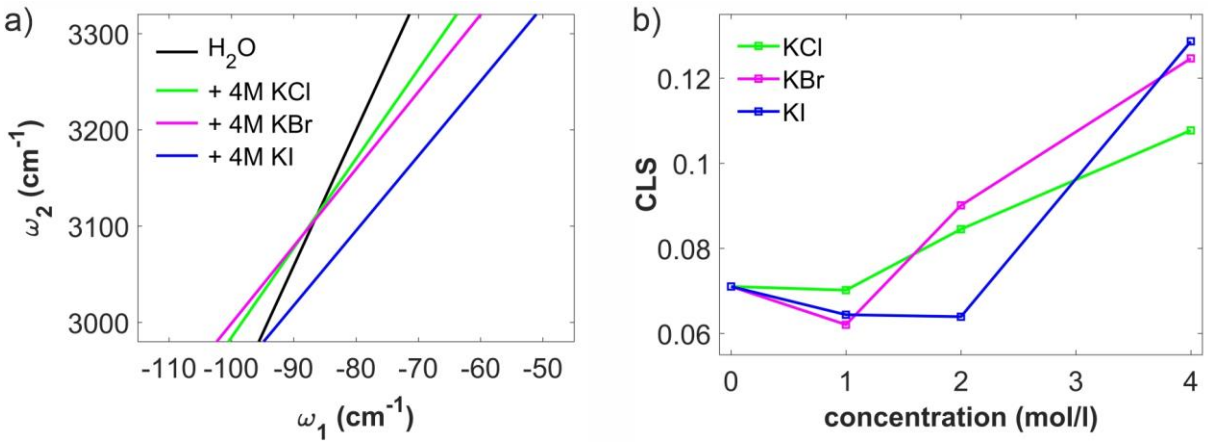

Fig. 6.6 a) Center line of peak β for neat water (black) and 4 M solutions of KCl (green), KBr (purple), KI (blue). b) Center line slope (CLS) for the different concentrations of the aqueous solutions of KCl (green), KBr (purple) and KI (blue).

An increasing CLS indicates an enhanced inhomogeneity of the LFM in the aqueous solutions in the presence of salts. To test if these changes can be associated with the formation of a hydration shell around the anions, we perform classical molecular dynamics (MD) simulations. To this end, we calculate the dynamics of the molecules in neat water and 1.5 M aqueous solutions of KCl, KBr, and KI. The water LFMs in the spectral range of the present study are dominated by hindered translation modes of the whole molecule, which are well represented by the vibrations of the oxygen atom. Thus, to explore the changes of the LFMs of water, we employ the velocity autocorrelation function $\mathrm{VAC_O}$ for the oxygen atom of the water molecule, which, in contrast to the $\mathrm{VAC_H}$ of the hydrogen atoms, does not include librational motions. The spectrum of the $\mathrm{VAC_O}$ is proportional to the spectral density of those vibrations that involve oxygen. Figure 6.7 shows the spectra of the $\mathrm{VAC_O}$ for neat water and the first hydration shell around the Cl^-, Br^- and I^- anions. This comparison demonstrates that the frequency of the maximum of the vibrational density of states (VDOS) in the range of the hydrogen-bond bending mode ($\approx 50\ \mathrm{cm^{-1}}$) is almost invariant. In contrast, the hydrogen-bond stretch modes around $180\ \mathrm{cm^{-1}}$ shift to the red noticeably. The displacement is the largest for the I^- solution and results in the formation of a new VDOS peak at $\approx 140\ \mathrm{cm^{-1}}$. Thus, the MD calculations show a red-shift of the VDOS of hydrogen-bond modes of water in the hydration shell of halide anions, which leads to an increased inhomogeneity of the hydrogen-bond dynamics in the samples. These findings are in agreement with the results obtained from the analysis of the 2D TIRV spectra.

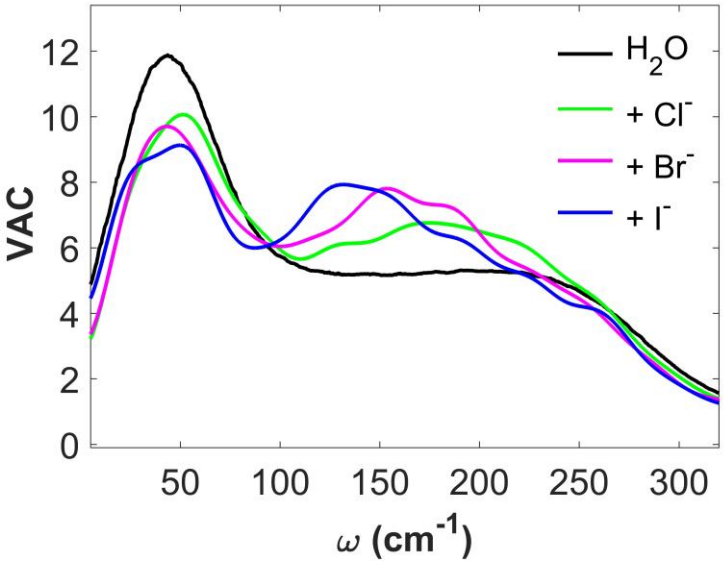

Fig. 6.7 Real part of the spectrum of the velocity autocorrelation function (VAC) for the oxygen atom in bulk water and the oxygen atom in the first hydration shell of the anions Cl^- (green), Br^- (magenta) and I^- (blue).

To summarize, the quadrant separation procedure described in chapter 4 enabled a more detailed analysis of the couplings and correlations between the low-frequency hydrogen-bond modes and the OH-stretch mode in aqueous solutions. By applying the concept of the center line slope to 2D TIRV spectra, we found an increasing inhomogeneity of these hydrogen-bond vibrations with the addition of salts by observing a correlation between the hydrogen-bond modes and the OH-stretch mode. Additional MD simulations showed, that this change can be related to the water molecules in the first hydration shell of the halide anions. Thus, we found that the addition of salts makes the dynamics of the hydrogen-bond network more inhomogeneous.

6.3 Methods

6.3.1 Linear absorption spectroscopy

The linear absorption spectra were obtained in the same way as described in the previous chapter and were measured using a commercial Bruker Vertex 70, extended to measure absorption spectra in the range from 30 to $6000\ \mathrm{cm}^{-1}$.

6.3.2 2D TIRV spectroscopy

Our 2D TIRV spectroscopy setup is described in detail in chapter 3 and 4. In brief, we split the output of an amplified Ti:Sapphire laser ($5\ \mathrm{mJ/pulse}$, $1\ \mathrm{kHz}$ repetition rate, about $60\ \mathrm{nm}$ FWHM) is split into three beams (each $\sim 1\ \mathrm{mJ/pulse}$), from which we generate the broadband mid-IR (centered at $\sim 3400\ \mathrm{cm}^{-1}$, $300\ \mathrm{cm}^{-1}$ FWHM), VIS (centered at $800\ \mathrm{nm}$, $1\ \mathrm{nm}$ FWHM) and THz beam (spectrum in Fig. 3.3), respectively. All beams are polarized horizontally, interact with the sample and thus generate the signal field. The signal field passes first a polarizer, to ensure horizontal polarization, and then a spectrometer. It is detected heterodyned using a CCD camera.

Here, we do not use a displaced Sagnac interferometer as in chapter 4 but generate the local oscillator (LO) by sum-frequency mixing of the IR and VIS pulses at the surface of a gold mirror as described in the previous section. The generated time delay of ≈ 100 fs between the 2D TIRV signal and LO due to the dispersion between the IR and LO beam in nitrogen gas is enough to apply the quadrant separation procedure of chapter 4. The data is processed in the same way as in the previous chapter.

6.3.3 Molecular dynamics calculations

We perform classical molecular dynamics (MD) simulations using the GROMACS 2020.1 software. The compositions of the aqueous salt solutions correspond to a 1.5 M concentration of KCl, KBr and KI, respectively. The calculations are performed in the same way as in the previous chapter.

7 CONCLUSION AND OUTLOOK

In this thesis, we showed how the successful further development of 2D TIRV spectroscopy enabled a more precise analysis of the spectra and thus to learn more about the dynamics of the hydrogen-bond network of liquid water. In particular, we investigated how the coupling between the OH-stretch mode and the low-frequency libration and hydrogen-bond modes changes when the water network is disrupted by salts. These results are of substantial fundamental interest and can also give an insight into the dynamics of (bio-)chemically relevant systems. The results in chapter 5 on the coupling between the libration modes and the OH-stretch mode show that the coupling with lower-frequency librations increases significantly with the addition of halide anions. This finding demonstrates the significance of the ions' impact on the water network. The observed inhomogeneity for the coupling between the hydrogen-bond modes and the OH-stretch mode in chapter 6 provides new insights into the network dynamics and the localization of the modes.

Chapter 4 of this thesis demonstrates how the experimental development can significantly improve the spectral analysis. A time delay induced between the local oscillator and the signal enabled the separation of positive and negative signal frequencies, and thus allowed distinguishing excitation pathways that show up in different quadrants of the 2D TIRV spectrum. This significantly simplified the analysis of the spectra. This procedure was verified using the two model samples, CaF2 and nitrogen gas. For CaF2, the signal is produced at the sum-frequency of the THz and IR beams, while for nitrogen gas, the signal is generated at the difference frequency of the two beams. For the more complex 2D TIRV spectrum of water, this quadrant separation procedure allows to disentangle the spectrum and to eliminate the interference pattern observed in previous measurements (Grechko et al., 2018).

The progress in the spectral analysis enabled advanced investigations of the coupling between the low-frequency vibrations (hydrogen-bond modes as well as libration modes) and the OH-stretch vibration in aqueous systems. To reveal how this coupling varies for a disrupted water network, we added potassium salts with the halide anions Cl-, Br- and I-.

For the coupling between the libration and the OH-stretch mode, we found in chapter 5 an increase of the 2D TIRV signal intensity with the addition of halide anions in chapter 5. This increase is due to a combined increase of the vibrational density of states, the transition dipoles, the polarizability, and the electrical coupling. Interestingly, the observed increase of the intensity depends on both, the concentration and type of the ion. We found the same order for the influence of the Cl-, Br- and I- ions as in the Hofmeister series. This is in line with many other experiments that found the same ordering, even though the exact context varied.

Chapter 6 focuses on the coupling between the hydrogen-bond modes and the OH-stretch mode. Since the coupling of these modes contributes to energy relaxation pathways in the water network, it plays a significant role in chemical and biological reactions in an aqueous environment. We found an increasing correlation between the frequency of the LFM and HFM mode for aqueous salt solutions of KCl, KBr and KI, which we assigned to the water molecules in the first hydration shell of the respective anions. To our knowledge, this is the first

experimental evidence for the inhomogeneity of the hydrogen-bond modes induced by halide anions.

The studies in this thesis considered only monatomic halide anions. The induced changes show a similar trend for the anions Cl-, Br- and I-. Studies with anions that change the water network in a different way might reveal other ways in which the coupling between different modes is affected. In contrast to the structure breaker ions Cl-, Br- and I-, F- is known as a structure maker with a redshifted OH-stretch frequency. An influence of the coupling in the opposite way seems possible, e.g. that the coupling of the libration modes gets weaker. Another interesting type of ions to study are polyatomic ions like perchlorate (ClO4-). Compared to the halide anions studied here, the OH-stretch of the water molecules in the hydration shell of perchlorate shows up as a peak that can be distinguished from the OH-stretch peak of the bulk water molecules. Here, studies on the coupling between the OH-stretch and the hydrogen-bond modes could show if the induced inhomogeneity of the hydrogen bonds varies significantly from the one induced by the halide anions in the present study.

As 2D TIRV is still a novel technique, it needs further advances in the measurements methodology and analysis of the spectra. The line shapes in 2D TIRV spectroscopy are barely understood. A systematic experimental study on the various influences on the line shape, like the spectra of the laser pulses, and the development of the theory of the line shapes could allow deeper insights into the nature of the measured couplings.

Likewise, why certain excitation pathways are preferred is still unclear. For water, we concluded that excitation pathways with the two-quantum transition at the second step are preferred. The reason for this preference for water, and more general, what determines the favorable excitation pathway for other molecules, is not clear. In the future, studying samples with more simple spectra, e. g. with only one narrowband LFM and HFM, respectively, could help to understand why different pathways are favored, and thus maybe also to assign the peaks in more complex spectra to the respective excitation pathway.

This broad range of possibilities for further developments shows the capability of new insights that 2D TIRV spectroscopy can provide. In addition, investigations beyond aqueous salt solutions can be promising, as they can reveal details of the dynamics of chemical and biological systems.

REFERENCES

[1] P. Ball, Chem. Rev. **108**, 74 (2008).

[2] M. Chaplin, Nat. Rev. Mol. Cell Biol. **7**, 861 (2006).

[3] E. Brini, C. J. Fennell, M. Fernandez-Serra, B. Hribar-Lee, M. Lukšič, and K. A. Dill, Chem. Rev. **117**, 12385 (2017).

[4] P. Ball, Nature **452**, 291 (2008).

[5] F. Franks, *Water: A Comprehensive Treatise. Volume 1. The Physics and Physical Chemistry of Water* (1972).

[6] L. G. M. Pettersson, R. H. Henchman, and A. Nilsson, Chem. Rev. **116**, 7459 (2016).

[7] K. Stokely, M. G. Mazza, H. Eugene Stanley, and G. Franzese, Proc. Natl. Acad. Sci. U. S. A. **107**, 1301 (2010).

[8] H. J. Bakker, Chem. Rev. **108**, 1456 (2008).

[9] B. Auer, R. Kumar, J. R. Schmidt, and J. L. Skinner, Proc. Natl. Acad. Sci. **104**, 14215 (2007).

[10] C. Pérez, D. P. Zaleski, N. A. Seifert, B. Temelso, G. C. Shields, Z. Kisiel, and B. H. Pate, Angew. Chemie Int. Ed. **53**, 14368 (2014).

[11] I. Bakó, A. Lábas, K. Hermansson, Á. Bencsura, and J. Oláh, J. Mol. Liq. **245**, 140 (2017).

[12] W. A. P. Luck, J. Mol. Struct. **448**, 131 (1998).

[13] Y. Marcus, Chem. Rev. **109**, 1346 (2009).

[14] F. Hofmeister, Arch. Für Exp. Pathol. Und Pharmakologie **24**, 247 (1888).

[15] H. Ohtaki and T. Radnai, Chem. Rev. **93**, 1157 (1993).

[16] G. Schwaab, F. Sebastiani, and M. Havenith, Angew. Chemie Int. Ed. **58**, 3000 (2019).

[17] M. F. Kropman and H. J. Bakker, Chem. Phys. Lett. **370**, 741 (2003).

[18] D. Laage and J. T. Hynes, Proc. Natl. Acad. Sci. U. S. A. **104**, 11167 (2007).

[19] A. W. Omta, M. F. Kropman, S. Woutersen, and H. J. Bakker, Science **301**, 347 (2003).

[20] M. Smiechowski, H. Forbert, and D. Marx, J. Chem. Phys. **139**, 14506 (2013).

[21] Y. Chen, H. I. Okur, N. Gomopoulos, C. Macias-Romero, P. S. Cremer, P. B. Petersen, G. Tocci, D. M. Wilkins, C. Liang, M. Ceriotti, and S. Roke, Sci. Adv. **2**, e1501891 (2016).

[22] P. Schienbein, G. Schwaab, H. Forbert, M. Havenith, and D. Marx, J. Phys. Chem. Lett. **8**, 2373 (2017).

[23] R. A. X. Persson, V. Pattni, A. Singh, S. M. Kast, and M. Heyden, J. Chem. Theory Comput. **13**, 4467 (2017).

[24] Y. Levy and J. N. Onuchic, Annu. Rev. Biophys. Biomol. Struct. **35**, 389 (2006).

[25] S.-H. Chong and S. Ham, Angew. Chemie Int. Ed. **53**, 3961 (2014).

[26] S. H. Chong and S. Ham, Acc. Chem. Res. **48**, 956 (2015).

[27] P. W. Atkins and J. De Paula, *Physikalische Chemie* (John Wiley & Sons, 2013).

[28] G. E. Walrafen, J. Chem. Phys. **47**, 114 (1967).

[29] D. A. Draegert and D. Williams, J. Chem. Phys. **48**, 401 (1968).

[30] G. Fleming, *Chemical Applications of Ultrafast Spectroscopy* (1986).

[31] P. R. Griggiths and J. A. de Haseth, *Fourier Transform Infrared Spectrometry* (2007).

[32] M. Cho, in *Springer Ser. Opt. Sci.* (Springer Verlag, 2019), pp. 1–34.

[33] R. E. Verrall, in *Aqueous Solut. Simple Electrolytes* (Springer US, 1973), pp. 211–264.

[34] P. Terpstra, D. Combes, and A. Zwick, J. Chem. Phys. **92**, 65 (1990).

[35] D. M. Carey and G. M. Korenowski, J. Chem. Phys. **108**, 2669 (1998).

[36] G. E. Walrafen, J. Phys. Chem. **94**, 2237 (1990).

[37] M. Heyden, J. Sun, S. Funkner, G. Mathias, H. Forbert, M. Havenith, and D. Marx, Proc. Natl. Acad. Sci. U. S. A. **107**, 12068 (2010).

[38] E. Libowitzky, Monatshefte Fur Chemie **130**, 1047 (1999).

[39] B. M. Auer and J. L. Skinner, J. Chem. Phys. **128**, 224511 (2008).

[40] S. A. Corcelli and J. L. Skinner, J. Phys. Chem. A **109**, 6154 (2005).

[41] F. Perakis, L. De Marco, A. Shalit, F. Tang, Z. R. Kann, T. D. Kühne, R. Torre, M. Bonn, and Y. Nagata, Chem. Rev. **116**, 7590 (2016).

[42] Y. Maréchal, J. Mol. Struct. **1004**, 146 (2011).

[43] S. Mukamel, *Principles of Nonlinear Optical Spectroscopy* (Oxford University Press, Oxford, 1995).

[44] M. Cho, *Two-Dimensional Optical Spectroscopy* (2009).

[45] K. Schmidt-Rohr and H. Spiess, *Multidimensional Solid-State NMR and Polymers - 1st Edition* (2012).

[46] Y. Tanimura and S. Mukamel, J. Chem. Phys. **99**, 9496 (1993).

[47] P. Hamm and M. T. Zanni, *Concepts of 2D Spectroscopy* (2011).

[48] T. L. Courtney, Z. W. Fox, K. M. Slenkamp, and M. Khalil, J. Chem. Phys. **143**, 154201 (2015).

[49] K. Ramasesha, L. De Marco, A. Mandal, and A. Tokmakoff, Nat. Chem. **5**, 935 (2013).

[50] T. Elsaesser, Acc. Chem. Res. **42**, 1220 (2009).

[51] D. Kraemer, M. L. Cowan, A. Paarmann, N. Huse, E. T. J. Nibbering, T. Elsaesser, and R.

J. Dwayne Miller, Proc. Natl. Acad. Sci. U. S. A. **105**, 437 (2008).

[52] J. Lu, X. Li, Y. Zhang, H. Y. Hwang, B. K. Ofori-Okai, and K. A. Nelson, Top. Curr. Chem. **376**, 6 (2018).

[53] M. Woerner, W. Kuehn, P. Bowlan, K. Reimann, and T. Elsaesser, New J. Phys. **15**, 025039 (2013).

[54] S. Palese, J. T. Buontempo, L. Schilling, W. T. Lotshaw, Y. Tanimura, S. Mukamel, and R. J. D. Miller, J. Phys. Chem **98**, 12466 (1994).

[55] A. Tokmakoff, M. J. Lang, D. S. Larsen, G. R. Fleming, V. Chernyak, and S. Mukamel, Phys. Rev. Lett. **79**, 2702 (1997).

[56] A. Tokmakoff and G. R. Fleming, J. Chem. Phys. **106**, 2569 (1997).

[57] M. Cho, J. Chem. Phys. **111**, 4140 (1999).

[58] P. Hamm and A. Shalit, J. Chem. Phys. **146**, 130901 (2017).

[59] J. Savolainen, S. Ahmed, and P. Hamm, Proc. Natl. Acad. Sci. U. S. A. **110**, 20402 (2013).

[60] A. Shalit, S. Ahmed, J. Savolainen, and P. Hamm, Nat. Chem. **9**, 273 (2017).

[61] M. A. Allodi, I. A. Finneran, and G. A. Blake, J. Chem. Phys. **143**, 234204 (2015).

[62] I. A. Finneran, R. Welsch, M. A. Allodi, T. F. Miller, and G. A. Blake, Proc. Natl. Acad. Sci. U. S. A. **113**, 6857 (2016).

[63] J. Lindner, P. Vöhringer, M. S. Pshenichnikov, D. Cringus, D. A. Wiersma, and M. Mostovoy, Chem. Phys. Lett. **421**, 329.

[64] S. Ashihara, N. Huse, A. Espagne, E. T. J. Nibbering, and T. Elsaesser, J. Phys. Chem. A **111**, 743 (2007).

[65] M. Grechko, T. Hasegawa, F. D'Angelo, H. Ito, D. Turchinovich, Y. Nagata, and M. Bonn, Nat. Commun. **9**, 885 (2018).

[66] R. Feynman, R. B. B, Leighton, and M. Sands, *The Feynman Lectures on Physics. Volume II.* (Addison–Wesley, 1964).

[67] Robert W. Boyd, *Nonlinear Optics - 3rd Edition* (2008).

[68] G. R. Wilkinson, J. Raman Spectrosc. **17**, 487 (1986).

[69] L. Vietze, M. Bonn, and M. Grechko, in *Springer Ser. Opt. Sci.* (2019), pp. 197–214.

[70] W. W. Parson, *Modern Optical Spectroscopy -2nd Edition* (Springer Berlin Heidelberg, 2015).

[71] A. M. Weiner, J. P. Heritage, and E. M. Kirschner, J. Opt. Soc. Am. B **5**, 1563 (1988).

[72] J. Dai, J. Liu, and X.-C. Zhang, IEEE J. Sel. Top. Quantum Electron. **17**, 183 (2011).

[73] H. G. Roskos, M. D. Thomson, M. Kreß, and T. Löffler, Laser Photonics Rev. **1**, 349 (2007).

[74] F. D'Angelo, Z. Mics, M. Bonn, and D. Turchinovich, Opt. Express **22**, 12475 (2014).

[75] N. Karpowicz, X. Lu, and X.-C. Zhang, J. Mod. Opt. **56**, 1137 (2009).

[76] A. Nahata and T. F. Heinz, Opt. Lett. **23**, 67 (1998).

[77] N. Karpowicz, J. Dai, X. Lu, Y. Chen, M. Yamaguchi, H. Zhao, X. C. Zhang, L. Zhang, C. Zhang, M. Price-Gallagher, C. Fletcher, O. Mamer, A. Lesimple, and K. Johnson, Appl. Phys. Lett. **92**, 011131 (2008).

[78] S. Mukamel, A. Piryatinski, and V. Chernyak, Acc. Chem. Res. **32**, 145 (1999).

[79] M. Khalil, N. Demirdöven, and A. Tokmakoff, J. Phys. Chem. A **107**, 5258 (2003).

[80] T. L. C. Jansen, B. M. Auer, M. Yang, and J. L. Skinner, J. Chem. Phys. **132**, 224503 (2010).

[81] S. T. Roberts, R. A. Nicodemus, A. Mandal, and A. Tokmakoff, J. Chem. Phys. **135**, 054509 (2011).

[82] M. Grechko, S. A. Bretschneider, L. Vietze, H. Kim, and M. Bonn, Angew. Chemie Int. Ed. **57**, 13657 (2018).

[83] M. Khalil, N. Demirdöven, and A. Tokmakoff, Phys. Rev. Lett. **90**, 4 (2003).

[84] P. Hamm and J. Savolainen, J. Chem. Phys. **136**, 094516 (2012).

[85] K. Kwak, S. Cha, M. Cho, and J. C. Wright, J. Chem. Phys. **117**, 5675 (2002).

[86] S. Yamaguchi and T. Tahara, J. Chem. Phys. **129**, 101102 (2008).

[87] S. Nihonyanagi, S. Yamaguchi, and T. Tahara, J. Chem. Phys. **130**, 204704 (2009).

[88] X. Lu, N. Karpowicz, Y. Chen, and X. C. Zhang, Appl. Phys. Lett. **93**, 261106 (2008).

[89] J. Dai, X. Xie, and X. C. Zhang, Phys. Rev. Lett. **97**, 103903 (2006).

[90] Y. Wang, L. A. Zhang, S. Shang, Z.-K. Liu, and L.-Q. Chen, Phys. Rev. B **88**, 024304 (2013).

[91] J. Israelachvili, *Intermolecular and Surface Forces* (Elsevier Inc., 2011).

[92] M. Bennouna, H. Cachet, J. C. Lestrade, and J. R. Birch, Chem. Phys. **62**, 439 (1981).

[93] P. K. Verma, A. Kundu, M. S. Puretz, C. Dhoonmoon, O. S. Chegwidden, C. H. Londergan, and M. Cho, J. Phys. Chem. B **122**, 2587 (2018).

[94] H. R. Zelsmann, J. Mol. Struct. **350**, 95 (1995).

[95] H. Tanaka, J. Henning, H. D. Lutz, and G. Kliche, Spectrochim. Acta Part A Mol. Spectrosc. **43**, 395 (1987).

[96] J. M. Hollas, *Modern Spectroscopy* (John Wiley & Sons, 2004).

[97] J. M. Dickey and A. Paskin, Phys. Rev. **188**, 1407 (1969).

[98] A. Ghalgaoui, L. M. Koll, B. Schütte, B. P. Fingerhut, K. Reimann, M. Woerner, and T. Elsaesser, J. Phys. Chem. Lett. **11**, 7717 (2020).

[99] H. Ito and Y. Tanimura, J. Chem. Phys. **144**, 074201 (2016).

[100] S. A. Burikov, T. A. Dolenko, P. A. Velikotnyĭ, A. V. Sugonyaev, and V. V. Fadeev, Opt. Spectrosc. **98**, 235 (2005).

[101] D.-Y. Wu, S. Duan, X.-M. Liu, Y.-C. Xu, Y.-X. Jiang, B. Ren, X. Xu, S. H. Lin, and Z.-Q. Tian, J. Phys. Chem. A **112**, 1313 (2008).

[102] W. H. Thompson and J. T. Hynes, J. Am. Chem. Soc. **122**, 6278 (2000).

[103] I. S. Joung and T. E. Cheatham, J. Phys. Chem. B **112**, 9020 (2008).

[104] K. Kwak, S. Park, I. J. Finkelstein, and M. D. Fayer, J. Chem. Phys. **127**, 124503 (2007).